Inorganic Chiral Nanomaterials:
Design Strategies and Their Properties

by

Jihyeon Yeom

A dissertation submitted in partial fulfillment
of the requirements for the degree of
Doctor of Philosophy
(Macromolecular Science and Engineering)
in The University of Michigan
2017

Doctoral Committee:

Professor Nicholas A. Kotov, Chair
Professor Sharon C. Glotzer
Professor Jinsang Kim
Professor Joerg Lahann

Jihyeon Yeom

jyeom@umich.edu
ORCID iD: 0000-0002-3032-8301

DEDICATION

To my loves

ACKNOWLEDGMENTS

"Live your life just like all the world is your stage"

I cannot remember the first time she told me the phrase. What I can remember is that I have been raised with an ambitious spirit, keeping the phrase in my mind throughout my life. I have never hesitated to make decisions; no matter how hard they are so long as they are aligned with the pursuit of my dream. I would like to express my deep gratitude to my mom, Sook Kim, who has been protecting and supporting me with all her love; and my sister, Jisoo Yeom, who will be my life-long best friend. Thanks to family for giving me such a wonderful life.

I also would like to express my sincere appreciations to my advisor, Professor Nicholas Kotov. When I made the decision on a Ph.D advisor, I considered two factors: scientific knowledge, and good mentorship. After working with him for six years, I can say that he has been a great advisor, full of insightful comments on research and kind advice on life. He has been always supportive and respectful. I thank Professors Jinsang Kim, Joerg Lahann, and Sharon Glotzer for being on my dissertation committee. Their guidance and comments helped me to improve my thesis.

There are many colleagues and friends who have enriched my Ph.D life. Especially, I would like to thank Naomi Ramesar, Mahshid Chekini, Gleiciani Silveira, Luiz Gorup, Doug Montjoy, and Drew Vecchio for making me realize that colleagues can be great friends. I cannot

imagine better people with which to share my days and nights. It is unusual that I could enjoy and have lots of fun while working so hard in the lab.

I also thank Macromolecular Science and Engineering department for all the support. When I started my Ph.D life, Nonna was more than an administrator. She has taken good care of me with loves just like an adoptive mom. I also appreciate University of Michigan's Rackham Predoctoral Fellowship and Barbour Scholarship programs.

TABLE OF CONTENTS

LIST OF FIGURES

x

LIST OF TABLES

ABSTRACT

Interest in the synthesis of chiral nanostructures has been fueled by their prime fundamental and potential application of chiral nanostructures in biosensing, telecommunication, display technologies, diffraction-free patterning, and chiral catalysis.[1,2] Although chirality is often associated with biochemistry due to numerous chiral biomolecules, today chiral inorganic nanostructures have attracted much attention, but their optical properties remain largely unexplored. Nanoscale inorganic chiral materials strongly rotate linear and circularly polarized light passing through them. Such optical effects are relatively easy to observe and are being actively investigated as a part of the study of chiral photonics and plasmonics. However, the opposite effects, the transfer of spin angular momenta of circularly polarized photons to materials and their subsequent nanoscale restructuring, are much less understood.

Chiroptical effects associated with the magnetic component of light are essential for studies of spintronics, skyrmions, magnetochemistry, and Earth's homochirality.[3–5] However, it has been well known since the times of M. Faraday[6] that the magnetic field of photons are generally much weaker than those forces based on the electrical component of electromagnetic waves. Despite the technological appeal of chiromagnetic phenomena as a platform for memory elements, optoelectronic devices, high-speed information processing, and chiral catalysts,[7,8] the

requirements of low temperatures of T = 5–7 K and high magnetic fields of B = 1.2–7.5 T complicates their implementation.[9–11] The problems that hamper the molecular design of materials possessing chiral centers with large magnetic moments, or those exhibiting long-distance spin-coupling that should also be thermally stable and oxidation resilient, are also well known.[12–14]

In chapters II and III of this dissertation, I describe an experiment that demonstrates how circularly polarized light (CPL) affects dispersions of racemic nanoparticles (NPs). The intrinsic, non-covalent electrostatic, dipole-dipole, and van der Walls interactions, as well as hydrogen bonds between NPs combined to produce different types of NP superstructures. The transition from individual NPs to their superstructure assemblies can be easily controlled, visualized, and studied by different means. This strategy was applicable to various materials such as gold. By illuminating a seed-free gold ion dispersion with CPL, I could obtain optically active gold nanostructures.

In chapter IV, I describe how I synthesized chiral cobalt oxide NPs using chiral molecules, namely, *L*- and *D*-cysteine as surface ligands. The chiral paramagnetic NPs showed ~ 10 times greater optical activity than other metal or semiconducting NPs of similar size.[15–17] Moreover, the optical activities of the latter were mainly in the UV region while our NPs show practical activity in both the UV and visible ranges.[15,18] The results of this study provide new opportunities for the design and synthesis of novel materials and contributes to a better understanding of materials at the nexus of magnetism and chirality.

CHAPTER I

Introduction

1.1 Chirality

The term chirality is derived from the Greek word χειρ (kheir) which means hand. Hands are an easy to understand example of chirality: no matter how the two hands of a person are oriented, the left hand can never be superimposed upon the right; they are mirror images of each other. A molecule is considered to be chiral if it lacks an internal plane of symmetry and has a non-superposable mirror image. In organic chemistry, the presence of an asymmetric carbon atom in a molecule is often the source of chirality. Symmetric molecules are achiral in that their mirror images are indistinguishable, or identical.

Chiral phenomena is a unifying chemical, optical, physical, and biological property with manifestations from the atomic to macroscopic scales; we confront them in everyday life: watching 3D movies, putting on gloves, taking single-enantiomer medicines, and the predominance of right-handed helical growth in climbing plants as well as right-handed shells. Elementary particles such as electrons and neutrinos also spin in certain directions: electrons of an atom orbit the nucleus generating right-handed chiral current, and a neutrino is a left-handed

object where its spin and movement directions are opposed to each other.[19] To date, the relationships between atomic chirality and macroscopic chirality have not been well understood.

Quartz crystals

Left-handed   Right-handed

(1) Macroscopic enantiomorphous crystals

Left-handed
L(+) alanine

Right-handed
D(-) alanine

(2) Molecular enantiomeric structures

Left-handed state   Right-handed state

spin vector   spin vector

Direction of motion   direction of motion

(3) Fundamental particles with spin and translatory momentum
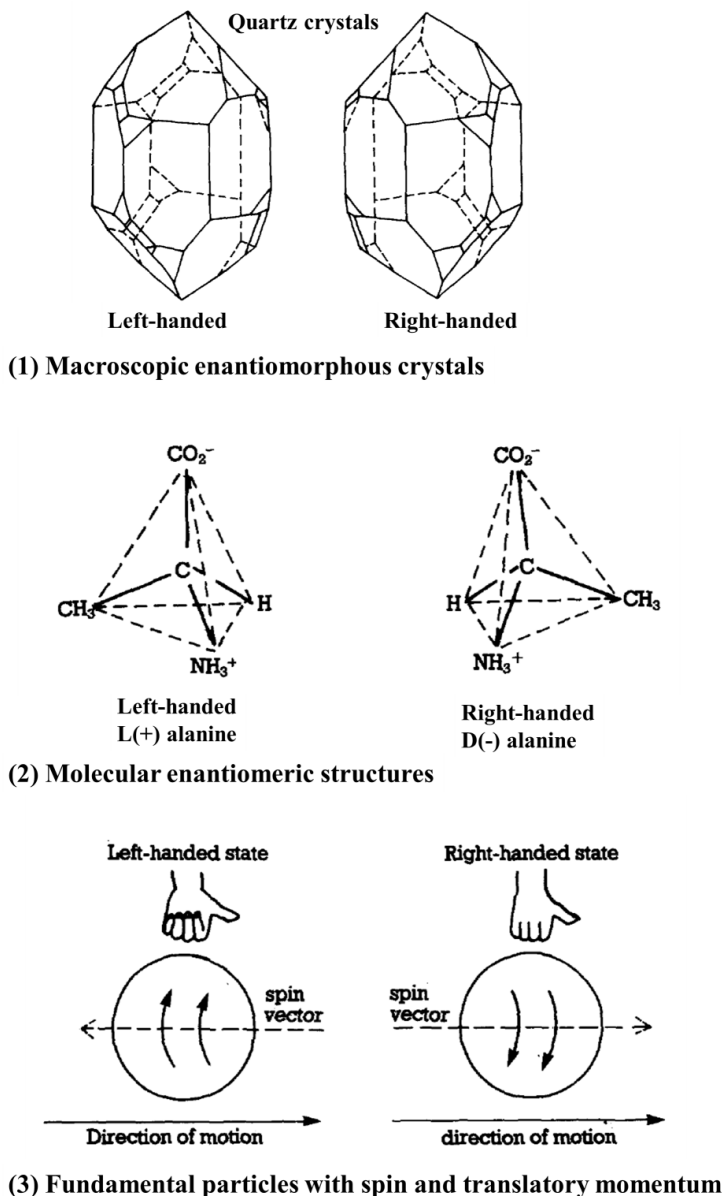
Figure 1.1. Three domains of chirality. (1) The minor crystal facets follow a left- or right-handed sequence, viewed along the threefold crystal axis. (2) The NH_3^+, CO_2^- and CH_3 groups of alanine follow a left-handed or right-handed sequence, viewed with the bonded hydrogen atom remote from the observer. (3) The left- or right-handed chirality of an electron, or any particle, derives from the respective antiparallel or parallel relation between the linear momentum vector and the axial vector of the spin angular momentum. [19]

1.1.1 Chirality in Nature

In old wine barrels, tartaric acid crystals build up on the vat walls. Since grapes contain (+) enantiomers of tartaric acid, one can obtain enantiomerically pure chiral tartaric acid crystals, which intrigued scientists like Jean-Bapstiste Biot and Louis Pasteur. In 1832, Biot discovered that tartaric acid organic crystals rotate plane polarized light (PPL), a phenomenon which we now call optical rotation or optical activity. In 1848, Pasteur found that tartaric acid can form two different types of crystals; ones like those from wine barrels and others that were mirror images of wine barrel crystals. Pasteur later reported the 'chirality' of tartaric acid crystals.

The importance of chirality was discovered after World War II. In the post-war era insomnia was prevalent, and the drug thalidomide was introduced to the market as a sleep inducing agent, which became popular with sales nearly matching those of aspirin. This was mostly in Europe, as thalidomide was never approved by the U.S. FDA for medical use. Thalidomide was also popular among pregnant women at that time because it was supposed to alleviate morning sickness. In 1961, a German newspaper reported that the drug caused critical birth defects as thousands of children were born with missing or deformed limbs. After the tragedy, studies revealed that the terotogenicity was due to the usage of the prescribed drug as a racemic mixture. It became clear that the enantiomers had very different properties once inside the human body; (+) thalidomide is a sleep inducing agent but it's (-) enantiomer is terotogenic. This changed the very nature of synthetic organic chemistry in general, and drug discovery and development in particular. The only method to distinguish one enantiomer from another is by examining how they interact with plane polarized light. One enantiomer will rotate PPL to some specific angle (clockwise or counter clockwise), and the mirror image molecule will rotate PPL

to the same degree, but in the opposite direction. All of the physical properties of enantiomers are the same; melting point, boiling point, density, etc.

This chiral selectivity occurs in the case of thalidomide, and many other substances, because the human body is formed with chiral materials such as left-handed amino acids and proteins, and right-handed DNA and RNA. Drug receptor sites are enantiospecific; one enantiomer may have a mode of action that is drastically different from its mirror image. The volatile organic molecule limonene reaches our nose and will smell either like pine or orange, depending on the chirality of the molecule. For the same reason, a chiral molecule may make a food taste sweet or bitter, depending on which enantiomer is present in the greater amount. In general, these phenomena occur because receptors in our nose, tongue, and cells are chiral.

Despite the fact that 150 years have passed since Pasteur discovered molecular chiral crystallinity, the origin of homochirality in nature's biomolecules is still uncertain. Several chemical routes are being debated, including the influence of circularly polarized light (CPL) from the cosmos.[20,21] The circular polarization of cosmic light has been predominantly observed in the infrared spectrum where simple organic molecules do not absorb these wavelengths, but inorganic NPs do absorb IR light. Magnetic field is another proposed route being debated regarding the origin of chiral biomolecules, since Earth itself is a magnet. Following Faraday's discovery of magnetically induced optical activity, Pasteur tried to grow chiral crystals in a magnetic field, but failed to produce positive results.

1.1.2 Optical Activity

Optical activity describes the phenomenon of rotating plane polarized light in either a clockwise or counterclockwise direction as the light travels through certain materials. The rotation of polarized light occurs in gases of spin-polarized atoms or molecules, solutions of chiral molecules, and solids with rotated crystal planes such as quartz. This rotation is a result of circular birefringence arising from a difference between the indices of refraction for right- (RCP) and left circularly polarized light (LCP), n_{LCP} and n_{RCP}, which implies that the extinction coefficients for RCP and LCP are different: ε_{LCP} and ε_{RCP}.

Both achiral materials and an equal mixture of a chiral molecule's enantiomers, known as racemic mixtures, do not rotate polarized light; but when a sample has an excess of one enantiomer, the plane can be rotated in either direction. This phenomenon is used in the sugar industry to measure syrup concentration, in optics to manipulate polarization such as polarized camera lenses, in chemistry to characterize substances in solutions, and in biology to measure bioactivities.

1.1.3 Circular Dichroism and Chiral Anisotropic Factor

Circular dichroism (CD) refers to the differential absorption of left and right circularly polarized light by optically active materials due to the difference between the extinction coefficients for right and left circularly polarized components. It is measured with a CD spectrometer, and the CD spectrum is the wavelength dependency of the difference in absorption between the right and left-handed components. By convention, a circular dichroism signal can be

positive or negative, depending on whether LCP is absorbed to a greater extent than RCP (CD signal positive) or to a lesser extent (CD signal negative).

$$\Delta\varepsilon = \varepsilon_{\text{LCP}} - \varepsilon_{\text{RCP}} \qquad \text{(Eq. 1.1)}$$

Another way to characterize chirality of materials is the chiral anisotropic factor, also known as the g-factor, which is defined as $\Delta\varepsilon/\varepsilon$, where $\Delta\varepsilon$ and ε are the molar CD and molar extinction coefficient, respectively.

$$g - factor = \frac{\Delta\varepsilon}{\varepsilon} \qquad \text{(Eq. 1.2)}$$

1.1.4 Rotational Strength

Rotational strength is a quantity describing CD that can be calculated using quantum chemistry with the imaginary part of the scalar product of the electric and the magnetic transition moments between the ground state 0 and excited state a:[22–24]

$$R_{oa} = \text{Im}[< \Psi_0|\hat{\mu}|\Psi_a >\cdot< \Psi_a|\hat{m}|\Psi_0 >]$$
$$= \text{Im}[\boldsymbol{\mu}_{0a} \cdot \boldsymbol{m}_{a0}] \qquad \text{(Eq. 1.3)}$$

where Ψ_0, and Ψ_a are the corresponding wavefunctions, $\hat{\mu}$ and $\hat{m}$ are the electric and magnetic moment operators, and $\boldsymbol{\mu}_{0a}$ and $\boldsymbol{m}_{a0}$ are the electric and magnetic transition dipole moments, respectively. In most systems, the absorption term related to the magnetic dipole component of the incident electromagnetic field is negligible in comparison to that of the electric dipole

component. [22,25,26] This term is considered imperceptible in small NPs as in most metallic and semiconducting NPs, and do not remarkably perturb the magnetic field of the incoming wave. [22,25,26] However, some exceptions have been observed when the molecules exhibit strong optical activities as a result of their strong magnetic transition dipole moment. [25,27,28]

1.2 Chiral Inorganic NPs

The first observation of optical activity from inorganic materials was achieved using a quartz crystal by F. J. D Arago in 1811. Nearly two centuries after this discovery, most studies in the field of inorganic chirality have been limited to biomological metal-organic complexes and inorganic salts. Recently, optical activity from a new class of metallic or semiconducting nanostructures has been observed. The introduction of chirality into the field of nanoscience may open a door for new applications beyond the conventional approaches such as biosensing, telecommunication, display technologies, diffraction-free patterning, and chiral catalysis[2].

1.2.1 Synthesis Strategies

There is a wide variety of methods for synthesizing chiral inorganic NPs using liquid-, solid-, and gas-phase precursors with top-down or bottom-up approaches. The most commonly used method is a liquid-based chemical bottom-up technique because of its economic benefits. This approach is based on the typical nucleation and growth of metal or semiconducting atoms, but in the presence of chiral stabilizers. In 2000, researchers reported that ~ 1 nm Au clusters, synthesized with glutathione, showed CD signals at the Au cluster electronic transition region.[29] After further discovery of chirality transformation using stabilizers on the surface of NPs

absorbance bands, [30,31] this method has been widely used to synthesize chiral metal NPs or semiconducting quantum dots (QDs) because of its versatility and simplicity. [32,16,17]
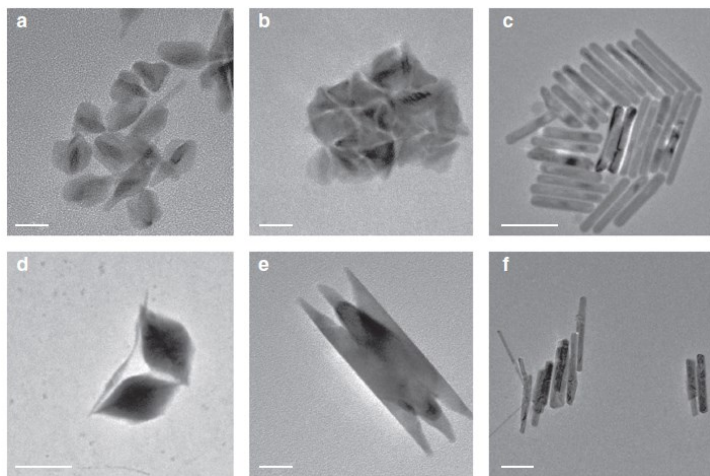
Figure 1.2. TEM images of tellurium and selenium nanocrystals produced by different procedures. (a,b) Tellurium nanocrystals, obtained with glutathione without hydrazine. Scale bar, 20 nm. In b, the nanocrystals are packed closely, and aligned with their long axis perpendicular to the surface, exhibiting the trigonally symmetric cross section. (c) Long tellurium nanorods, obtained with glutathione and hydrazine. Scale bar, 100 nm. (d) Tellurium nanocrystals obtained with L- or D-penicillamine and hydrazine. Scale bar, 200 nm. (e) Tellurium nanocrystal, obtained with hydrazine and glutathione added in a reversed order of sample 2. Scale bar, 20 nm. (f) Selenium nanocrystals obtained with cysteine. Scale bar, 200 nm.[17]
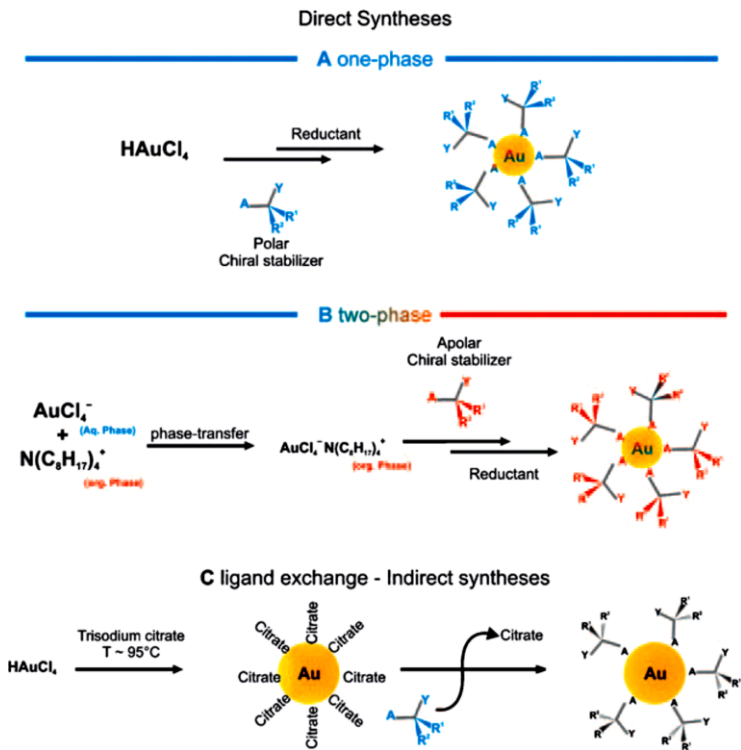
Figure 1.3. Different methods exploited for the syntheses of optically active AuNPs with chiral ligands. [32]
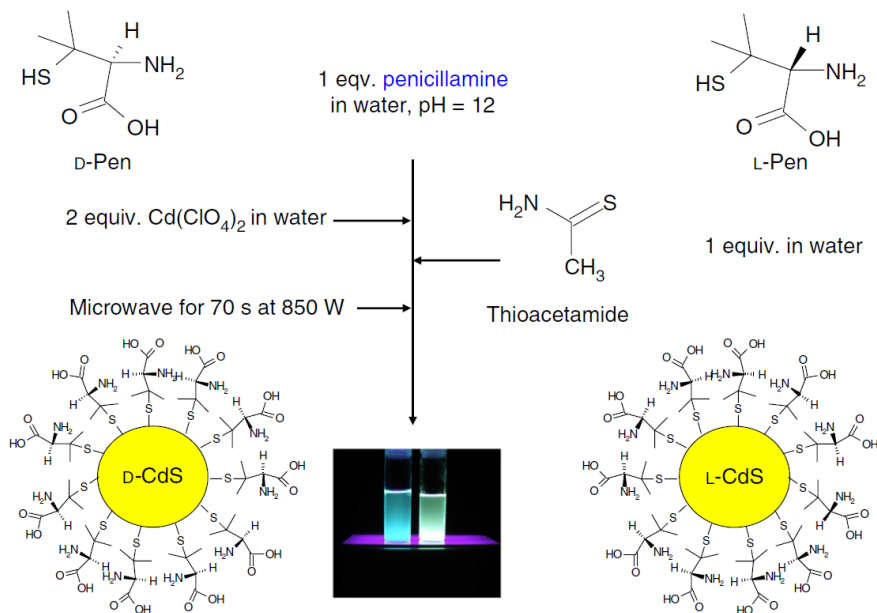
Figure 1.4. Schematic presentation of the synthesis of chiral CdS QDs. [16]
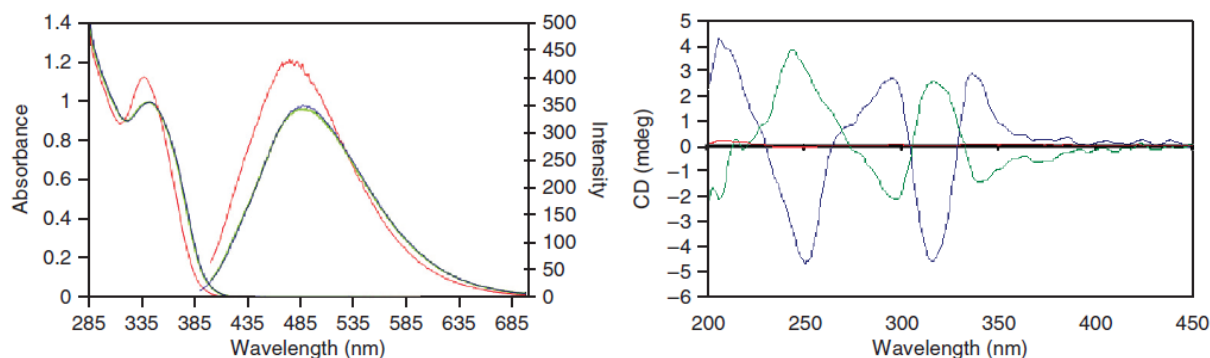
Figure 1.5. Left: UV-visible and emission (Ems) spectra of d-penicillamine CdS, (blue), absorbance (Abs) 345 nm, Ems 492 nm, l-penicillamine CdS, (green), Abs 345 nm, Ems 492 nm and Rac-penicillamine CdS (red). All PL spectra were excited at 360 nm. The higher quantum yield of the Rac-dots is clearly visible in the picture. Right, CD spectra of d-penicillamine (red), l-penicillamine (green), and Rac-penicillamine (blue)-modified CdS particles. [16]

In most cases, the CD signals change with the size of the NPs, and the anisotropic g-factors increase with decreasing NP size. The g-factor of these NPs is about $10^{-5} \sim 10^{-3}$.

1.2.2 Origin of Optical Activity of Chiral NPs

Several models have been proposed to explain the optical activity of inorganic NPs protected with chiral stabilizers [29,32]: (1) the inorganic core is inherently chiral; (2) a chiral organic shell on the surface induces optical activity with an intrinsically achiral core; (3) optical activity can be observed due to electronic interactions between a chiral molecule on the surface and the core electrons even though neither the surface nor the core of NP is chiral.

Models (1) and (2) have been supported by experimental and theoretical calculations. Nishida and co-workers observed the emergence of optical activity of ~ 1.5 nm Ag clusters by replacing racemic stabilizers with enantio-pure stabilizers.[15] Considering the higher chemical

reactivity and anisotropic factors of these Ag clusters compared to those of similar sized Au clusters with the same stabilizers, the author speculated that a chiral deformation of the core structure might be the origin of the optical activity.[33]

On the other hand, it has been demonstrated that Au_{15} and Au_{18} clusters reversed their optical activity when the chiral stabilizer was changed to its opposite enantiomer (model 2, Figure 1.4). [34] In the case of CdTe or CdS nanocrystals, the chiroptical properties were passivated even after the stabilizers exchange with opposite enantiomers. It has been proposed that the optical activity originated from distorted surface structures, and that chiral molecule-capped CdTe and CdS nanocrystals have a robust chiral memory on their surfaces (Figure 1.5).[35] Thus, different models should be used to explain the origin of optical activity of each chiral systems made with different materials.
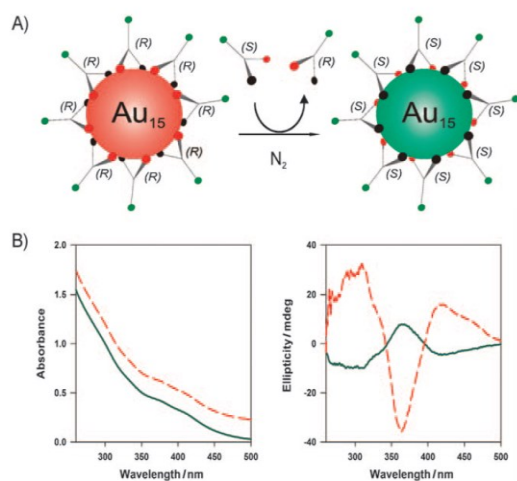
Figure 1.6. A) Schematic illustration of "chiral inversion" under inert atmosphere. The chiral adsorbed ligand is exchanged for its opposite enantiomer. B) UV/Vis (left) and CD spectra (right) of Au_{15}(N-isobutyryl-*L*-cysteine)$_{13}$ before (red dashed line) and after exchange with N-isobutyryl-*D*-cysteine (green solid line).[32,34]
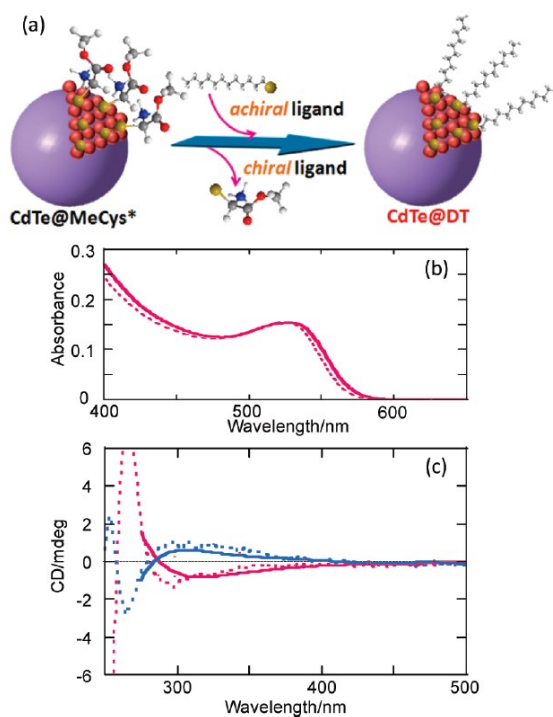
Figure 1.7. (a) Schematic illustration of ligand-exchange reaction. (b) UV-vis absorption spectra of D-MeCys-capped CdTe NCs (dotted line) and DT-capped CdTe NCs (solid line) after ligand-exchanged from D-MeCys. (c) CD spectra of D-MeCys (red) and L-MeCys (blue)-capped CdTe NCs (dotted lines) in water and DT-capped CdTe NCs (solid lines) in chloroform ligand-exchanged from D-MeCys (red) and L-MeCys (blue) -capped CdTe NCs. [35]

CHAPTER II

Chiral Templating of Self-assembly Nanostructures by Circularly Polarized Light

from *Nature Materials*, **14**, 66-72 (2015)

2.1 Abstract

The high optical and chemical activity of nanoparticles (NPs) signifies the possibility of converting the spin angular momenta of photons into structural changes in matter. Here, we demonstrate that illumination of dispersions of racemic CdTe NPs with right- (left-) handed CPL induces the formation of right- (left-) handed twisted nanoribbons with an enantiomeric excess exceeding 30%, which is ~10 times higher than that of typical CPL-induced reactions. Linearly polarized light or dark conditions led instead to straight nanoribbons. CPL "templating" of NP assemblies is based on the enantioselective photoactivation of chiral NPs and clusters, followed by their photooxidation and self-assembly into nanoribbons with specific helicity driven by chirality-sensitive interactions between NPs with tetrahedral cores. The ability of NPs to retain the polarization information of incident photons should open pathways for the synthesis of chiral photonic materials and allow for better understanding of the origins of biomolecular homochirality.

2.2 Introduction

Materials with nanoscale chirality are known to strongly rotate the polarization of linearly polarized (LinP) and circularly polarized light (CPL). Such optical effects in nanomaterials with different chiral geometries are being actively investigated as a part of chiral photonics and plasmonics.[36–43] The opposite effects, i.e. the transfer of spin angular momenta of circularly polarized photons to matter and its subsequent nanoscale or atomic restructuring, retaining the "memory" of circular polarization, are much less known. The possibility of such effects at the atomic and nanometer scale is indicated by, for instance, the formation of spiral nano-needles with controlled helicity during laser ablation of bulk metallic tantalum with CPL,[44] although the mechanism of this effect is not well understood. The transfer of spin angular momenta in high intensity laser beams was also observed for Bose–Einstein condensates,[45] ensembles of cold atoms,[46] and microscale colloids.[47] These special chromophores/scatterers acquired circular or spiral motion while being illuminated by high intensity CPL. However, it is difficult to convert the photon spin into permanent structural changes of atomic and particulate systems, due to their achiral symmetry, structural barriers for channeling the rotational energy into chemical bonds, and fast quenching of rotational motion by the media.

The transfer of spin angular momentum into particle rotation was observed for a wide range of sizes and molar masses (M) of particles – from $M \approx 10^2$ for ensembles of cold atoms [46] to $M \approx 5 \times 10^{12}$ for microscale colloids.[47] CPL effects could be possible to observe for nanoparticles (NPs) that are intermediate in mass and size between atom clusters and microparticles, and are similar in masses to Bose-Einstein condensates ($M \approx 10^7$).[45] NP dispersions stable at ambient conditions are more convenient to use than some of these chromophores/scatterers and can be more reactive than polymeric colloids[47] or bulk tantalum.[44]

The larger physical size of the NPs should enhance the photochemical effects of light with different handedness compared to those observed for chiral organic molecules.[48,49]

CPL-induced restructuring of NP systems can provide a new, powerful, and versatile tool for (nano)chemistry of chiral materials. The interest in the synthesis of chiral nanostructures has been fueled by the potential application of chiral nanostructures in biosensing, telecommunication, display technologies, diffraction-free patterning, and chiral catalysis.[37–43] Further motivation to study long-term structural changes caused by CPL in matter is evidenced by the ongoing discussion about the origin of homochirality in natural compounds. Natural amino acids and sugars exist predominantly as left-handed (LH) and right-handed (RH) enantiomers, respectively. Illumination with CPL[20,50,51] was recently suggested as one of the plausible causes of homochirality. [20,21] However, the mechanism of how CPL can lead to homochirality of organic molecules is not known. Several chemical routes are being debated,[50,51] including chiral amplification.[52]

Self-assembly of NPs is one of the mechanisms that could potentially be influenced by CPL. Such expectations are based on (a) atomic and nanoscale chirality of individual NPs,[53,54] (b) amplification of circular polarization effects in NP assemblies,[22,55] and (c) sensitivity of self-assembly processes to small changes in interparticle interactions.[56] Also, inorganic NPs represent a convenient building block for nanoscale synthesis, affording a variety of pathways to geometrically complex nanostructures. Based on this hypothesis, we investigated the effects of CPL on the assembly of water-soluble NPs under ambient conditions.

2.3 CPL Induced Chiral Self-Assembly

A dispersion of CdTe NPs, stabilized by achiral capping agent thioglycolic acid (TGA), was illuminated either by left- (LCP) or right-handed circularly polarized light (RCP) with a wavelength of 543 nm. Note that this CdTe dispersion revealed no circular dichroism (CD) peaks in the visible range (Fig. 2.5) and therefore has equal cumulative absorbance for LCP and RCP photons at 543 nm. From a previous study[57] we expected the formation of twisted nanoribbons but it was unclear whether polarization of light would have an effect on their assembly pattern and geometry. CPL-induced transformations of NPs were examined after 1, 12, 28, 35 and 50 h of illumination (Fig. 2.1A and 2.1B). The temporal progression of the products included short 50-200 nm rods (1 h) that evolved into 1-2 μm twisted nanoribbons (12 h) and subsequently into 2-3 μm longer nanoribbons (28 h). After 50 h of illumination, twisted nanoribbons with total lengths, pitch lengths, and diameters of 3 ± 0.5 μm, 800 ± 20 nm, and 50 ± 5 nm, respectively, were the predominant products of the photo-induced reaction (Fig. 2.1C and 2.1D). When nanoribbons were exposed to CPL for more than 96 h, they started to be thinner, but retained their twisted shape (Fig. 2.6). After 50 h of photoinduced assembly and in the absence of further illumination, the nanoribbons retained their geometry for the entire project time (3.5 years).

Circular polarization of light exhibited an enantio-selective photochemical influence on NP dispersions and the geometry of self-assembled nanoribbons. Under LCP illumination, predominantly left-handed (LH) nanoribbons were formed, as established by SEM (Fig. 2.1A and 2.7). When the NP dispersion was illuminated with RCP, right-handed (RH) nanoribbons of otherwise similar dimensions prevailed (Fig. 2.1B and 2.8). In both cases, the differences between LH and RH nanoribbon fractions obtained after analysis of 100 scanning electron

microscopy (SEM) images of ~ 1000 nanoribbons were more than 30% (Fig. 2.1E), which was well in excess of the experimental error of ~5 %. Note that this is also much higher than a typical enantiomeric excess in CPL-stimulated organic reactions (0.5-2%).[14] The chiral preference in nanoribbon geometry was also confirmed by circular dichroism (CD) spectroscopy. CD spectra of purified nanoribbons were measured in aqueous dispersions and revealed distinct chiroptical bands at 490, 590, and 700 nm (Fig. 2.1F). Comparison of CD and absorption spectra after 50 h illumination (Fig. 2.10) indicates that the first two bands in CD spectra are associated with the absorption in the band-gap transition. Importantly, nanoribbon dispersions illuminated by LCP and RCP showed positive and negative CD signals, respectively. Transmission electron microscopy (TEM) tomography (Fig. 2.2A, and B), capable of visualizing 3D structures of the nanoribbons, corroborated the conclusions regarding their chiral shape.

A control experiment involving illumination with un-polarized light (UnP) showed equal distribution between right- and left-handed nanoribbons in agreement with the previous study.[57] Illumination with LinP as well as incubation in the dark yielded straight nanowires that were the overwhelmingly dominant products in these two cases. Nanowires produced by exposure to UnP and LinP revealed no CD activity (Fig. 2.11), which is consistent with the SEM data (Fig. 2.13).

Another experimental series contributing to understanding of templating effect of photons on the mesoscale geometry of nanoribbons and nanowires was the illumination of CdTe dispersions with a different light source at 607 nm for 50 h. The efficiency of chiral induction by LCP is reduced as the difference between the yield of LH and RH nanoribbons drops to ~20% (Fig. 2.14) compared to illumination at 543 nm. This observation is consistent with the reduced intensity of NP absorbance at the fringes of the band gap transition (Fig. 2.5B).

In order to avoid the effects of chirality arising from potential artifacts of small molecular weight compounds present in solution, we compared CD spectroscopy of ensembles of chiral structures in dispersion with CD measurements taken for single nanoribbons (Fig. 2.2E and 2.2F) for the 600-800 nm spectral window. The single LH and RH nanoribbons revealed correspondingly positive and negative mirror-image CD signals. A band located at ~660-700 nm is spectrally similar to the band observed for dispersions (Fig. 2.1F; the effective spectral window of the quarter wave plate used prevents single particle CD measurements in the 400 - 600 nm region). Figs. 2.15 and 2.16 demonstrate that the CD spectra of the single twisted nanoribbons measured using dark field microscopy are dominated by light scattering. Therefore, the 'red' CD bands in Fig. 2.1F should be predominantly attributed to scattering of LCP and RCP photons on twisted nanoribbons with specific handedness and, in fact, are may be considered in the framework of circular intensity differential scattering.[58] As a control experiment against potential artifacts we measured CD spectra from single nanoribbons at various rotational angles in respect to the long axis. The shape of CD spectra remained unchanged regardless of the nanoribbon orientation (Fig. 2.17). As another control experiment, confirming attribution of the origin of the CD bands, non-twisted nanoribbons did not show any CD signals (Fig. 2.18).

The chiroptical properties of the twisted nanoribbons can be compared to those of microscale gold helixes made by 3D lithography[43] which also exhibit broadband polarization rotation. Anisotropy factors of g = 0.02–0.04 were obtained from numerical FEM solutions of the Maxwell equations for CdTe twisted ribbons models (Fig. 2.2C, and 2.2D), which is comparable to the values obtained for Ag-enhanced Au nanohelices and Au nanorods/fiber composites, g ~ 0.025.[37,38]

2.4 Mechanisms

To understand how circular polarization of photons causes distinct permanent differences in shapes of nanoribbons, we first addressed the mechanism of light-induced self-assembly of CdTe NPs. From the optical properties (Fig. 2.11) and the relative content of NPs in the supernatant of nanoribbons dispersions assembled with and without light (Fig. 2.19), it becomes apparent that, along with the spontaneous self-assembly of NPs,[57,59] there is a parallel light-stimulated process of the formation of twisted ribbons. We found that FTIR peaks for v(O-H), δ(O-H), v_s(COOH), characteristic of TGA ligand located at 3500 cm^{-1}, 1567 cm^{-1}, and 1421 cm^{-1}, respectively, were drastically decreased in nanoribbons compared to the original CdTe NPs (Fig. 2.3A). A strong peak at 1722 cm^{-1} corresponding to v_{as}(COO$^-$) of carboxyl moieties was observed in the supernatant obtained after separation of twisted nanoribbons and NPs by centrifugation. Concomitantly, the characteristic UV-Vis absorption peak of TGA at 276 nm decreased as illumination time increased (Fig. 2.20), indicating its decomposition. The presence of an S 2p signal from CdS in X-ray photoelectron spectra (XPS) of nanoribbons (Fig. 2.21) and the weakness of peaks for Te from CdTe (Fig. 2.22) indicate that illumination also results in the replacement of Te in the NPs with S; the elemental atomic composition of nanoribbons were 51.5 % Cd, 47.3 % S, 1.2% Te (Table 2.1). The mechanism of photoinduced replacement of Te by S in NPs is likely to involve ionic diffusion of S^{2-} ions formed by photoinduced oxidation of TGA into the NPs. TEM of the twisted region (Fig. 2.23, and 2.24), atomic mapping images (Fig. 2.26), and energy dispersive spectroscopy (EDS) spectra (Figs. 2.27 and 2.28) confirmed the transformation of CdTe NPs into CdS NPs (Fig. 2.3B). These results are consistent with previous

findings regarding formation of a thin CdS shell around CdTe NPs due to chemical decomposition of TGA (Supplementary Information) and photoinduced oxidation of CdTe.[60]

X-ray photoelectron spectroscopy spectra (Fig. 2.30) indicated that there was no significant difference in chemical composition of left and right-handed nanoribbons. Therefore, the assembly mechanism should be the same for RCP and LCP illumination. Spectroscopy and microscopy data in Fig. 2.3 and Figs. 2.20-2.31 suggest that the light-induced mechanism of nanoribbon self-assembly starts with the photoinduced decomposition of TGA to form S^{2-} that subsequently replaces Te^{2-} ions in NPs. The loss of the already sparse TGA shell is likely to be the trigger of the light-induced NP assembly into twisted structures. Such attribution of the self-assembly mechanism encounters, however, an unexpected complication. The electrokinetic zeta-potential, ζ, decreased from $\sim$ -6 mV to $\sim$ -15 mV upon illumination (Fig. 2.33); the increase in electrostatic repulsion must hinder the assembly process contrary to the results observed. Calculations of the pair-potentials between the NPs using extended Derjaguin-Landau-Verwey-Overbeek theory (E-DLVO) help to explain this discrepancy and confirm the light-induced assembly mechanism. Even though the zeta-potential of "bare" CdS NPs are more negative, the loss of the TGA shell and increased ionic strength associated with the surface ligand photooxidation makes the overall pair potential more attractive (Fig. 2.34).

Based on the above results, the effect of circular polarization of incident light on NP self-assembly originates in the optically selective activation of nanostructures with different handedness. Both individual CdTe NPs and their clusters can be chiral. As such, aberration corrected TEM tomography indicates the existence of chiral dislocations of atoms in Pt NPs.[54] Chirality of individual Au NPs in racemic mixtures capped with achiral ligands was previously

shown with liquid chiral chromatography.[61]   With the help of a high-angle annular dark field (HAADF) scanning transmission electron microscope (STEM) (Figs. 2.3G and 2.3H), we found that the TGA-stabilized NPs have the shape of a truncated tetrahedrons. The distinct truncated tetrahedron shape of CdTe-TGA NPs was also seen in high resolution TEM images (Fig. 2.3I). Four uneven truncations result in a chiral tetrahedron similar to a sp^3 hybridized carbon atom with three different substituents (Fig. 2.3S). To confirm the chirality of individual NPs, we incubated the dispersion of TGA-stabilized CdTe NPs with bovine serum albumin (BSA, 66.5 kDa) serving here as an enantio-selective absorber. After 5 hour of incubation, we separated BSA and unbound NPs using centrifugal membrane (50 kDa), and measured CD spectra of obtained dispersions. In contrast to the original CdTe NPs that has no CD signals (Fig. 2.5) and BSA that has a negative CD peak at around 215 nm (Fig. 2.37), the separated NPs showed positive CD band at 400-550 nm (Fig. 2.38) coinciding with the excitonic transition of NPs. This observation indicates that the starting NP dispersion is a racemic mixture of NP enantiomers with different chirality that can be enantio-selectively separated.

Simulation of light absorption showed that enantiomers of truncated NPs (Fig. 2.3C, 2.3S) should display optical activity, as reflected in the mirror-imaged simulated CD and g-factor spectra (Fig. 2.3D). Spontaneously formed small clusters of NPs similar to those in Fig. 3G can also be chiral. According to our simulations, the differences in absorption of LCP and RCP in such clusters (Fig. 2.3F) are even greater than in NPs (Fig. 2.3D). In both cases, there is a large difference in absorption of LCP and RCP at 543 nm for nanostructures of different handedness used for this study.

Then, the mechanism of the chirality transfer from CPL to NP assemblies can be understood as follows. The original CdTe NP solution is racemic and contains equal amounts of

left- and right-handed particles and small clusters. When a racemic mixture of CdTe NPs (Fig. 2.5A) is illuminated by LCP at 543 nm, a subpopulation of LH NPs and clusters absorb light more effectively (Fig. 2.40 step **2**) than RH NPs and clusters. The same is true for RH NPs/clusters (Fig. 2.40, step **2'**) when the dispersion is illuminated with RCP. The light-activated CdTe NPs undergo photooxidation of TGA stabilizers that transforms them into "bare" CdS NPs. Photooxidation of multiple TGA ligands on the surface of NPs requires multiple photons and, therefore, the difference in the probability of absorption of *L-* and *R-*photons multiplies over time. This process "locks in" and amplifies the differences between the NPs of opposite chirality in the initially racemic mixture.

The ligand-free CdS NPs display a much stronger propensity to self-assemble than ligand-protected, non-light-activated CdTe NPs of opposite handedness (Fig. 2.34). Because the self-assembly of NPs is very sensitive to the anisotropy of NP interactions,[59] the chirality of the constituent building blocks is reflected in the helicity of the resulting assemblies similar to the self-assembly of organic and biological macromolecules.

2.5 Atomistic Molecular Dynamic Simulations

Atomistic molecular dynamics (MD) simulations were performed to further clarify the origin of the observed ribbon helicity. Individual NPs were modeled as slightly smaller 3.6 nm tetrahedrons with a cubic CdS crystal lattice and a lattice constant of a = 0.582 nm (Fig. 2.4A). The tetrahedrons were asymmetrically truncated by the removal of 2, 3, and 4 atom layers from three of the NP vertices to acquire a left or right chirality. The NPs surfaces were not coated with stabilizers, in accordance with the experimental results presented in Fig. 2.3 and Figs. 2.20 -31, indicating ligands removal in the process of photoactivation. However, the large CdS lattice

polarity was reduced at the NP surfaces to one half of the vacuum value to account for the potential presence of residual ligands. NPs at different (homogeneous) charging states were simulated in accordance with experimental observations. The MD simulations were carried out with explicit water molecules and Cl^- counterions of the charged NPs (Fig 2.4A) to precisely describe the solvent environment of the NP self-assembly process.

Initially, NPs of the same (*L* or *R*) handedness (Fig. 2.4B) were preassembled into a planar piece of nanoribbon (Fig. 2.4C) with packing similar to that observed before,[57] assuming that NPs of predominantly one handedness were prepared by photoexcitation with a circularly polarized light and self-assembled. Upon equilibration of the NP assemblies in an isothermal–isobaric ensemble at T = 300 K for ~ 5-10 ns, the planar nanoribbons acquired distinct twists. Importantly, the twist was opposite for NPs with opposite handedness. The average twist angle observed in the simulation of the nanoribbons made from CdS NPs was - 3.1º and +4.3º for LH and RH NPs (Fig. 2.4D and 2.4E), respectively, which corresponds to a pitch length of ~1,400-1,900 nm similar to the experimental pitch length of nanoribbons observed after 28 h illumination in Figs. 2.1 and 2.2.

These observations confirm the significance of NP chirality in guiding the ribbon assembly and the realism of the photon-matter chirality transfer via geometry-specific photoactivation of NPs. The nanoribbon twists observed in the MD simulations clearly originate in the chirality (truncations) of the NPs, promoted via molecular-field-assisted NP-NP interactions into a cooperative phenomenon. As the light-transformed NPs are still largely solvated in water, their self-assembly into ribbons proceeds mostly via their bulk van der Waals coupling and partial hydrophobicity. However, water molecules form a soft "cushion" layer between the NPs within the ribbons, which allows the NPs to partially translate and reorient with

respect to each other in accordance with the needs imposed by their chirality. The experimental structures are partially disordered (Fig. 2.24) due to fluctuations of the NP size that translates into some variability of the pitch and non-close packing of NP lattice in the ribbon.

Vivid experimental demonstration of subtle differences in interparticle interactions between a priori chiral NPs leading to nanostructures with different chirality can be obtained for NPs with a stabilizing ligand made from *D*- and *L*-cysteine (Fig. 2.4F, and 2.4G.) These originally chiral NPs were self-assembled in the dark and produced submicron helices with distinctly different twist directions depending on the chirality of the building blocks.

2.6 Conclusion

In conclusion, we have demonstrated that circular polarization of light can be "imprinted" on nanoscale structures by altering the chirality of NPs participating in the self-assembly process. Because light-sensitivity is common for NPs (see SI for details), this study offers new synthetic methods for chiral nanostructures using light as the primary parameter determining the asymmetry in the enantiomeric mixture of the products. Furthermore, geological records suggest that inorganic NPs were a part of the primordial Earth conditions,[62] and therefore, selective photonic activation of seemingly achiral NPs might represent the missing link between cosmic CPL[20,50,51] and inorganic/organic materials with preferential chirality.
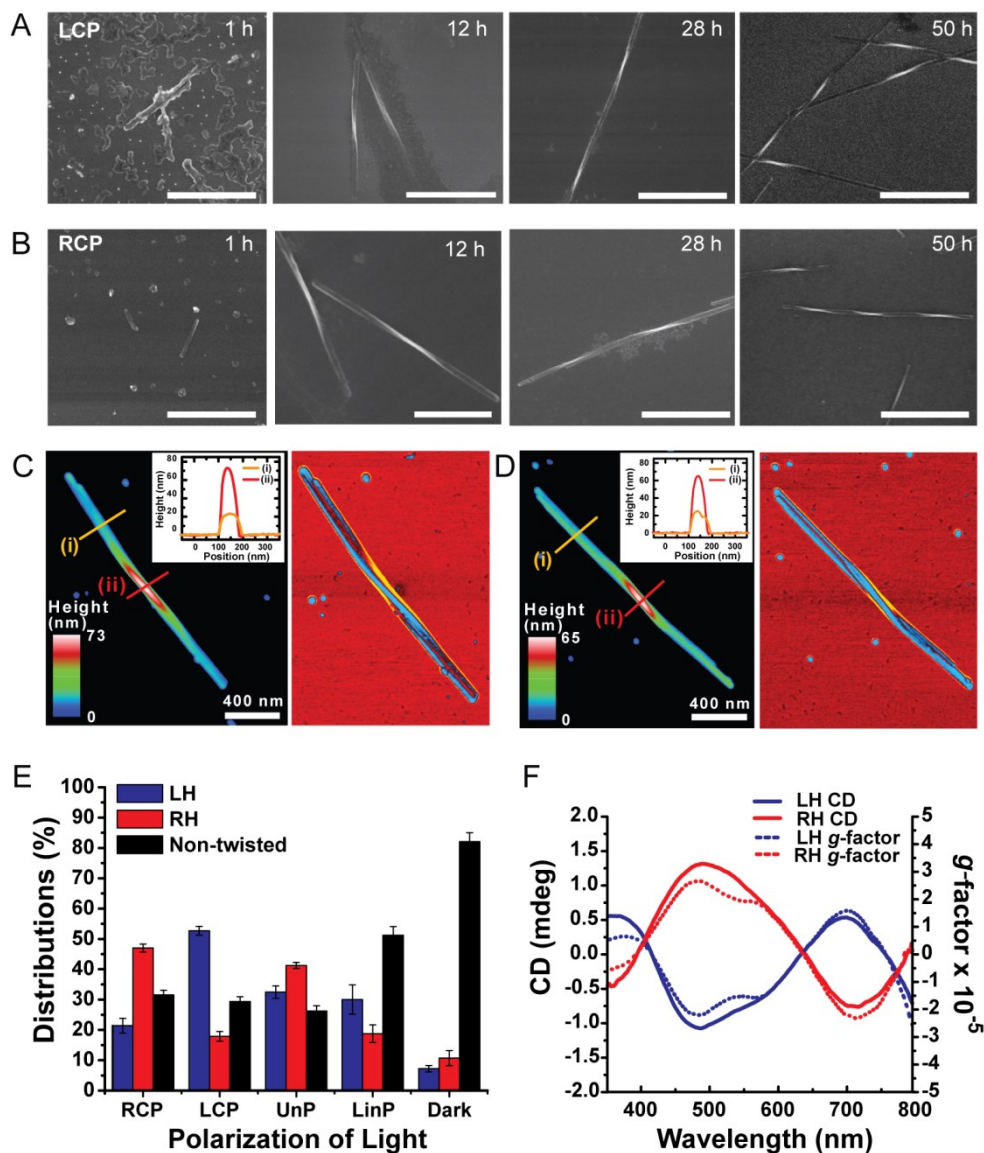
Figure 2.1. Self-assembly of CdTe NPs into twisted nanoribbons induced by illumination with CPL. **A** and **B,** SEM images of the ribbons assembled with LCP (A) and RCP (B) as a function of time exposure for 1 h, 12 h, 28 h and 50 h. All scale bars are 1 μm. **C** and **D,** tapping mode atomic force microscopy (AFM) topographic (left) and phase (right) images of LH nanoribbon (C) and RH nanoribbon (D). **E,** Distributions of LH, RH, and non-twisted nanoribbons obtained after 50 h illumination with RCP, LCP, UnP, LinP light, and in the dark. **F,** ensemble CD spectra (solid line) and *g* factor (dotted line) of dispersions of left-handed (LH) nanoribbons and right-handed (RH) nanoribbons obtained after 50 h of CPL illumination. Linear dichroism effects that could be associated with adsorption on the walls of the cuvette and other spontaneous alignment of linear nanostructures have negligible contribution to the chiroptical properties as indicated by the identity of the CD spectra obtained with and without stirring of the dispersion.
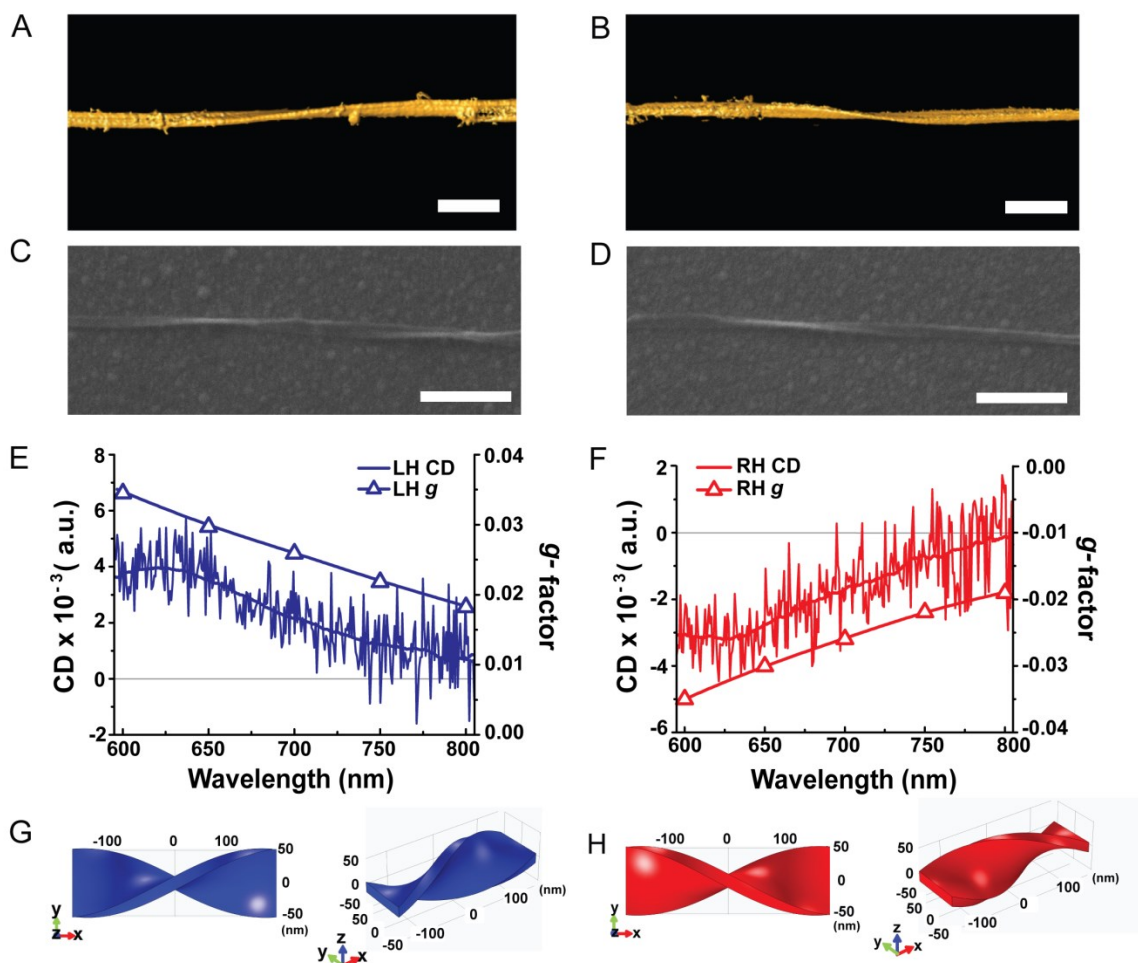
Figure 2.2. Chirality of single nanoribbons. A and **B,** Surface rendering of 3D TEM tomographic reconstruction of LH nanoribbon (A) and RH nanoribbon (B). Scale bars are 100 nm. See also a supplementary video file with 3D rendering of the LH nanoribbon. **C** and **D,** SEM images of single LH (C) and RH nanoribbons (D). Scale bars are 500 nm. **E** and **F,** CD spectra and calculated *g*-factor spectra for single LH (E) and RH (F) nanoribbons in C and D, respectively. **G** and **H,** Computational models of the LH (G) and RH (H) nanoribbons used in the FEM calculations of chiroptical properties based on numerical solutions of Maxwell equations. All scales are nm.
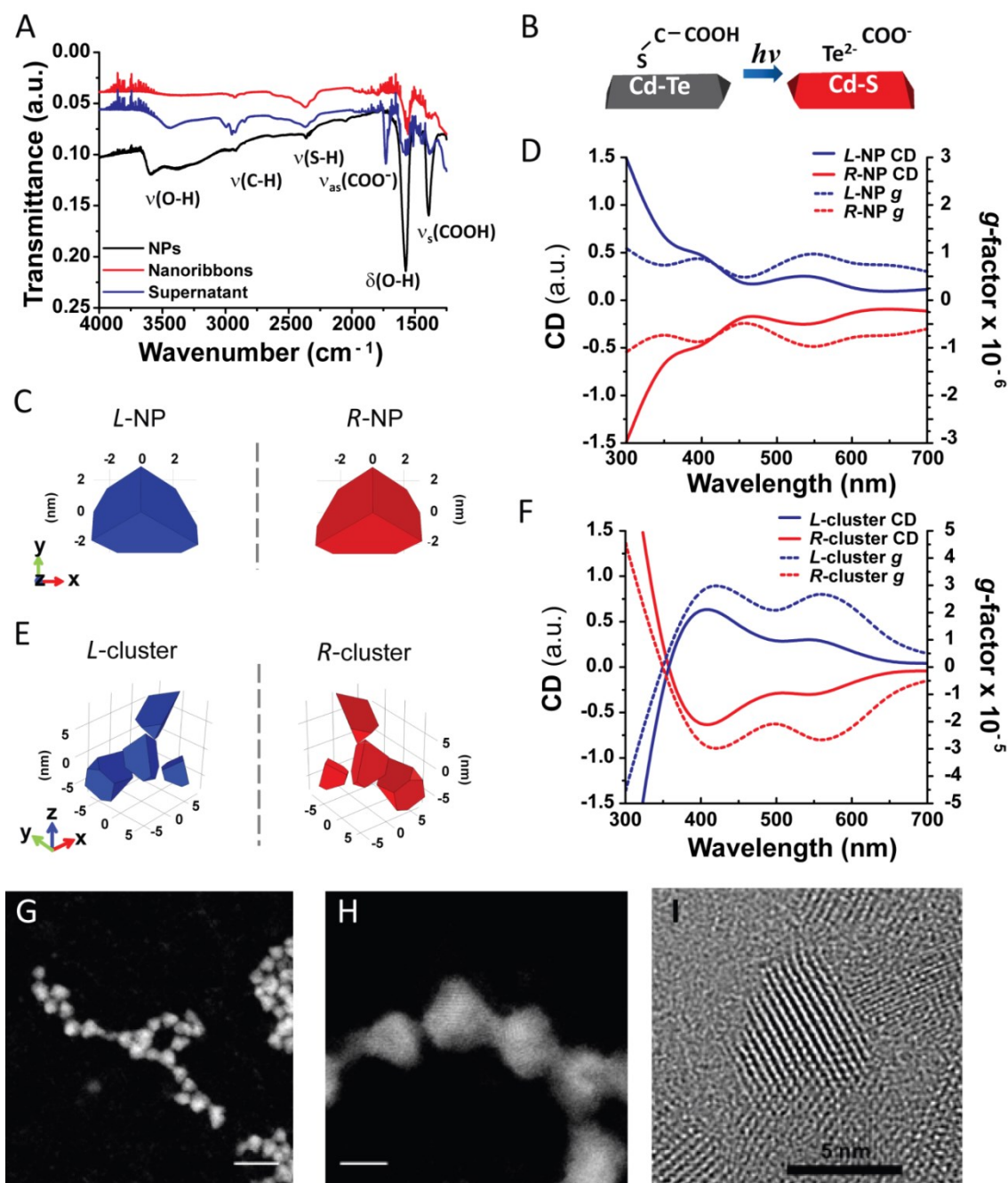
Figure 2.3. Mechanism of enantioselective assembly of NPs. A, FTIR spectra of original CdTe NPs, purified nanoribbons, and supernatant obtained after 50 h of illumination time. **B,** Schematic illustration of CdTe phase transition to CdS. **C,** and **E**, Models of chiral NPs (C) and chiral NP clusters (C) used in calculations of chiroptical properties. **D,** and **F,** Simulated spectra and *g*-factors for (D) *L/R*-NPs and (F) *L/R*-clusters of NPs. Nomenclature for NPs and their clusters is based on the positive (*L*) and negative (*C*) optical activity. **G,** and **H,** HAADF STEM images of TGA-stabilized truncated tetrahedral CdTe NPs. Scale bars are 15 nm (G) and 5 nm (H). **I,** High resolution TEM image of TGA-stabilized truncated tetrahedral CdTe NPs.
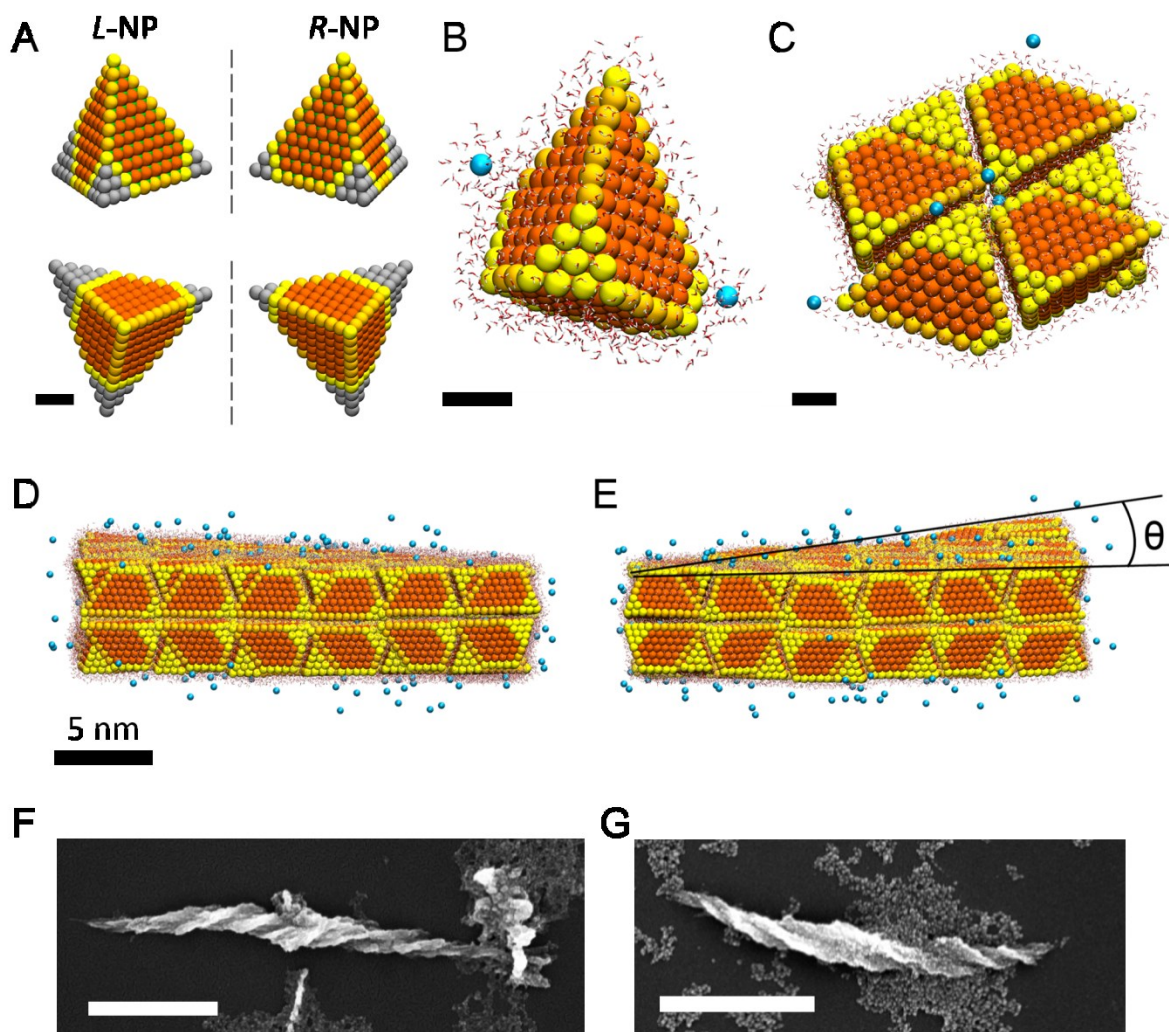
Figure 2.4. Molecular dynamic and experimental studies of self-assembly of chiral NPs. A, Atomistic models of NPs with LH and RH truncations used in MD simulations. **B,** Detailed view of a single NP in aqueous environment with counter ions used in MD simulations. **C,** A fragment of the simulated self-assembled ribbon from (top view) displaying packing of NPs. Scale bars in A, B, and C are 1 nm. **D,** and **E,** The side views of simulated NP ribbon with LH (D) and RH (C) truncated NPs. Dihedral angle θ determines the pitch of the nanoribbons. **F,** and **G,** SEM images of experimental assemblies spontaneously formed in dark from chiral CdTe NPs stabilized by L-cysteine (F) and D-cysteine (G). Scale bars are 1 μm.

2.7 Supplementary Information

2.7.1 Experimental Methods

Synthesis and analysis of twisted nanoribbons: CdTe NPs were synthesized with the reduced amount of thioglycolic acid (TGA) stabilizer. We used the literature procedure [57] with the TGA to Cd^{2+} ratio of ~1.1. To induce the self-assembly of CdTe NPs, templating chirality of CPL, the amount of TGA in the dispersion was significantly reduced by precipitation and redispersion of CdTe NPs in purified water at pH = 9. The pH was adjusted by the addition of 0.1 M NaOH, and the precipitation was done by addition of methanol followed by centrifugation for 20 min. The dispersion was placed in a dark room, and then exposed to circularly polarized light. As the NPs were assembled into nanoribbons by illuminated CPL, the orange color was turned to dark green.

The morphology of assembled nanoribbons were analyzed by tapping mode atomic force microscopy (AFM) with NTEGRA Spectra tips (NTEGRA Spectra at Korea Basic Science Institute, NT-MDT), scanning electron microscopy (SEM, FEI Nova), and transmission electron microscopy (TEM, JEOL 3011) To measure optical activity, the nanoribbons were separated from the solution by gentle centrifugation (bench-top centrifuge, 3000 rpm, 3 min) and redispersion in distilled and deionized water. The CD spectra were obtained by a JASCO J-815 instrument. The Fourier transform infrared spectroscopy (FTIR), energy dispersive spectrometry (EDS, JEM-2200FS, JEOL) and X-ray photoelectron spectra (XPS, Kratos Analytical AXIS Ultra) were used to exam the composition of nanoribbons.

Optical set-up for the CPL induced assembly: The green (543 nm) helium-neon laser with random polarization of emitted photons (Research Electro-Optics, Inc. Boulder, Colorado) was used as a light source. The laser emission was transformed to CPL by directing it through a linear polarizer and a quarter-wave plate. Since the quarter-wave plate is made with a birefringent material, the linearly polarized light turned to CPL by passing through the quarter-wave plate with the 45° transmission angle. By rotating the quarter-wave plate 90° relative to the previous angle, the handedness of CPL is changed.
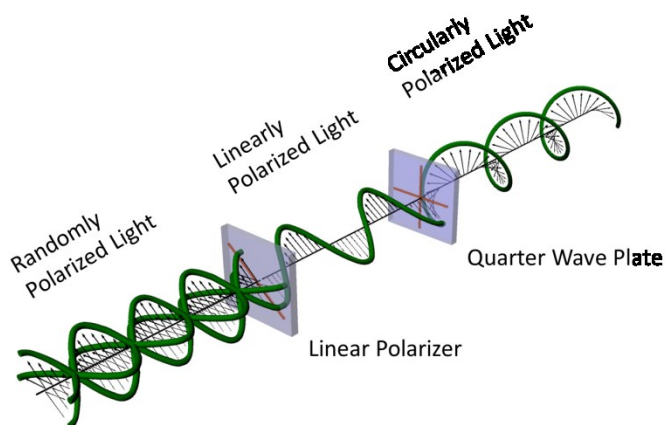
Scheme 2.1. Schematic illustration of the optical set up for the CPL-templated assembly of NPs.

Chiral separation of racemic CdTe-TGA dispersion with bovine serum albumin (BSA): We chose BSA as a chiral separator because its enantiomeric recognition ability has been studied to separate racemic mixture of amino acids. [63] To prevent the interference of residual capping agents in the CdTe NPs dispersion, we centrifuged NPs dispersion, removed supernatant, and then re-dispersed NPs in 50 µM BSA (66.5 kDa) solution. After incubation for 5 h at room temperature in the dark with magnetic stirring, CdTe NPs were separated from BSA by 50 kDa

centrifugal filter (Millipore). The optical activities of obtained CdTe NPs were measured using CD spectrometer (JASCO J-815).

3D TEM tomography: The electron tomography studies at room temperature were carried out on a Tecnai F20 electron microscope (FEI Corporation, Hillsboro, OR.) equipped a Gatan 4K × 4K CCD camera and a field emission gun (FEG) operating at 200 kV. A series of 2D projection images were recorded at a nominal magnification of × 11,500 by tilting the specimen from -75º to 60º for LH nanoribbons and -66º to 75º for RH nanoribbons in increments of 1.5º. Images were recorded at an underfocus value around 7 μm. Colloidal nanogold particles of 15 nm in diameter were used as fiducial markers to aid tracking during data collection and image alignment during reconstruction. A tomography reconstruction software package IMOD [64], was used to align the tilt series and calculate three-dimensional tomograms using a weighted back projection algorithm. The surface rendering was generated using the UCSF Chimera software [65].

Single nanoribbon scattering, extinction, and CD spectroscopy: Measurements of scattering spectra on single twisted nanoribbons were performed with a homebuilt dark-field microscope. In brief, the unpolarized light from a halogen lamp used as a light source was focused by an oil-immersion dark-field condenser (Zeiss, N.A. = 1.40) and transmitted scattered light was collected by a 50X air-spaced objective (Zeiss, NA = 0.8) and guided to either an avalanche photodiode detector (Micro Photon Device) or a spectrometer equipped with a liquid nitrogen cooled CCD camera (Horiba Jobin Yvon). Nanoribbons were deposited on an indexed microscope coverslip, which was mounted on a XY piezo scanning stage (Physik Instrumente). The scattering images were taken by scanning the sample with the piezo stage across a 50 μm

pinhole located at the first image plane of the microscope and the scattering signal was detected by the avalanche photodiode detector. A LabView interface was designed to synchronize the stage movement and the data acquisition. A typical image was composed of 128 x 128 pixels with an integration time of 5 ms/pixel. Single-nanoribbon spectra were collected by positioning the particle of interested over the pinhole and then guiding the light toward the CCD camera. All measured single-nanoribbon spectra were corrected for the background scattering and normalized by the intensity of the excitation light.

Single-nanoribbon CD measurements were performed when a polarizer followed by a quarter-waveplate were placed before the dark-field condenser. Left-handed and right-handed circular polarization was controlled with the fast axis of the quarter-waveplate set to -45deg and 45deg with respect to the axis of the polarizer, respectively. The CD spectrum was calculated by subtracting the scattering spectrum for right-handed circular polarization from that taken with left-handed circular polarization. Note that scattering CD spectra have been reported to have different lineshapes compared to absorption for macromolecules. [66]

In our previous work, a correction procedure was developed for single particle CD measurements and applied here for any slight deviations from perfectly circular polarization of the incident radiation at the sample based on CD measurements of randomly orientated single gold nanorods. [67] In the context of this study they can be considered to be achiral and thus should have no CD signal We find that ellipticity in the polarization of the excitation light gives rise to artifact CD signals of the gold nanorods as a function of their relative orientation with respect to the major/minor axes of elliptically polarized light. Measurement of numerous gold nanorods at different orientations, determined first by taking linearly polarized spectra, allowed us to

construct a correction factor for our single particle scattering CD measurements. We applied this orientation-dependent correction factor to the nanoribbons. To further test the validity of this procedure for the system studied here we collected single particle CD spectra of the same nanoribbon as a function of its orientation by rotating the sample. The results are shown in Fig. 2.17 and the independence of the CD spectra on nanoribbon orientation illustrate that our correction procedure eliminates artifacts in the CD spectra originating from non-perfect circular polarization. It should further be noted that this correction procedure specifically addresses deviations from circular polarized excitation light, while using a condenser to excite the sample ensured that light was incident from all angles, effectively averaging the CD response over all orientation and establishing an important correspondence to ensemble measurements in solution. Minor fluctuations in the CD peak intensity as a function of nanoribbon orientation were likely due to focus drift over the course of the experiment, though contributions from linear anisotropies in the media may also be a factor. In future experiments, a piezoelectric stabilized objective will be used to minimize this possible error.

Single nanoribbon extinction measurements were performed using a microscope setup, in which light from a lamp at normal incidence was focused on the sample using an objective. Comparison between the light intensity collected with and without the nanostructure of interest present in the observation area yielded the extinction. All data analysis was carried out using MatLab software.

2.7.2 E-DLVO Calculations and Computational Simulations

Simulation of chiroptical properties: Optical activities of chiral structures were computationally simulated using a COMSOL Multiphysics software package with wave-optics module. Computational models for twisted ribbons used in the simulations were based on the experimental data obtained from SEM, TEM and AFM (Figs. 2.1 and 2.2). The model twisted ribbons had a width, thickness, and pitch length of 100 nm, 10 nm, and 300 nm, respectively. Optical constants of CdS were adapted from Ref [68].

The *g*-factors obtained for single nanoribbons can be compared to those reported for small organic molecules after plasmon enhancement $g = 0.005$ [69–71], assembled gold NPs on DNA $g = 0.02$ [37], polyaromatic compounds $g = 0.05$ [72], and protein complexes $g = 0.06$ [73].

For simulation of chiroptical properties, the COMSOL models of NPs were created. To simulate random orientation, CD values are calculated from average of directional CDs with light propagating directions of two spherical angles, θ (0 to π) and φ (0 to 2π) with a step of $\pi/6$. The environment was water (n=1.33). Characteristic optical constants of CdTe NPs were obtained from Ref [74].

CdTe NPs were truncated along three apexes but in different positions to create chiral geometry (Figs. 2.3G-I). For an *L*-type nanoscale cluster, four truncated NPs were arranged in space accordingly. The sizes of each NP were scaled as 0.75, 1, 1.1, and 1.2 to reflect the polydispersity of NPs. The L-cluster was mirrored to the plane of x = 0 to obtain an *R*-cluster.

E-DLVO calculations:

Interaction potential (E-DLVO) between nanoparticles

The extended DLVO interaction energies between nanoparticles were approximated by the following expression:

$$V_{EDLVO} = V_{VdW} + V_{DL} + V_{DP} \, , \qquad \text{(Eq. 2.1)}$$

where V_{VdW}, V_{DL}, V_{DP} are van der Waals (VdW), double electric layer (DL) , and dipole-dipole (DP) interaction potentials, respectively.

Van der Waals interaction potential

Van der Waals potential approximated as additive contributions of London dispersion forces between CdTe NPs capped with a shell of TGA can be evaluated as follows [75,76]:

$$V_{VdW} = V_{VdW,shell} + V_{VdW,core} + V_{VdW,core-shell} + V_{VdW,shell-core} \, , \qquad \text{(Eq. 2.2)}$$

where

$$V_{VdW,shelll} = \frac{-A_{232}H_{shell}(m,n)}{12} \quad : m = \frac{x}{2(R_{CdTe}+d)} \, , n = 1 \qquad \text{(Eq. 2.3)}$$

$$V_{VdW,core} = \frac{-A_{131}H_{core}(m,n)}{12} \quad : m = \frac{x+2d}{2R_{CdTe}} \, , \ n = 1 \qquad \text{(Eq 2.4)}$$

$$V_{VdW,core-shell} = \frac{-A_{132}H_{core-shell}(m,n)}{12} \quad : m = \frac{x+d}{2R_{CdTe}} \, , \ n = \frac{R_{CdTe}+d}{R_{CdTe}} \qquad \text{(Eq. 2.5)}$$

$$V_{VdW,shell-core} = \frac{-A_{132}H_{shell-core}(m,n)}{12} \quad : m = \frac{x+d}{2(R_{CdTe}+d)} \, , \ n = \frac{R_{CdTe}}{R_{CdTe}+d} \qquad \text{(Eq. 2.6)}$$

The Hamaker function, *H(m,n)*, is given by:

$$H(m,n) = \frac{n}{m^2+mn+n} + \frac{n}{m^2+mn+m+n} + 2\ln\left[\frac{m^2+mn+m}{m^2+mn+m+n}\right],$$ (Eq. 2.7)

where x is the shortest distance between the TGA-capped CdTe NPs, A_{131} is the Hamaker constant of CdTe interactions in water (4.85 x 10^{-20} J, value of closely CdS NPs [77,78] was used), A_{232} is the Hamaker constant of TGA interactions in water (5 x 10^{-21} J, which approximates interactions between hydrocarbon chains in water [79–81]), A_{132} relates CdTe and TGA in water. And was approximated from the following relation [79] :

$$A_{132} = (\sqrt{A_{11}} - \sqrt{A_{33}})(\sqrt{A_{22}} - \sqrt{A_{33}}) ,$$ (Eq. 2.8)

where $A_{11} = 11.4 \times 10^{-20}J$, value of CdS in air [82], $A_{22} = 7 \times 10^{-20}J$ [81], $A_{33} = 3.72 \times 10^{-20}J$ [79]. R_{CdTe} =5 nm is the radius of CdTe NPs, d= 0.76nm, is the thickness of the TGA layer around the NPs.[83]

Electrostatic potential associated with double electrical layer

The electrostatic interactions between the NPs can be evaluated using the Poisson-Boltzmann formalism as follows [84–87] :

$$V_{DL} = 4\pi\varepsilon_o\varepsilon_r(R_{CdTe} + d)^2\Gamma^2\left(\frac{k_BT}{e}\right)^2\frac{\exp(-\kappa x)}{x+2(R_{CdTe}+d)}, \text{ where}$$ (Eq. 2.9)

$$\Gamma = \frac{8*\tanh(\frac{e\psi_{CdTe-TGA}}{4k_BT})}{1+\sqrt{1-\frac{2\kappa(R_{CdTe}+d)+1}{(\kappa(R_{CdTe}+d)+1)^2}\tanh^2(\frac{e\psi_{CdTe-TGA}}{4k_BT})}} ,$$ (Eq. 2.10)

where ε_0 is the permittivity of vacuum, ε_r is the dielectric constant of water and ψ_{CdTe} is the zeta potential of CdTe-TGA(-6mV) NPs . κ, the reciprocal double layer thickness (Debye length), is given by

$$\kappa = \sqrt{\frac{1000 N_A e^2}{\varepsilon_r \varepsilon_0 k_B T}} \sum_i M_i \times Z_i^2, \qquad \text{(Eq. 2.11)}$$

where e is electric charge (in Coloumbs), N_A is Avogadro's number, M_i and Z_i are the molar concentration and valency of ions, respectively. The practical Debye length of water is taken to be $\kappa^{-1} \approx 100$ nm [88–90].

Dipole-Dipole Interactions

Dipole-dipole interaction potential is approximated by the following [85,86]:

$$V_{DP} = \frac{-\mu_{CdTe}^2}{2\pi\varepsilon_o\varepsilon_r} * \frac{1}{r(r^2 - 4R_{CdTe}^2)}, \text{ where} \qquad \text{(Eq. 2.12)}$$

$$r = x + 2d + 2R_{CdTe} \qquad \text{(Eq. 2.13)}$$

Here, μ_{CdTe} , the dipole moment of CdTe NPs, is taken to be 100 D based on the data reported in [91,92].

Interaction between "naked" CdS NPs:

E-DLVO between CdS NPs

Only the interactions between the CdS NP cores are present in this case because the TGA shell was destroyed during the illumination (see Fig. 2.3 and Figs. 2.20-31). Therefore, distance consideration related to the thickness of the stabilizer layer as opposed to the case of CdTe-TGA NPs, is not required.

$V_{VdW}(CdS, CdS)$

$$= -\frac{A_{131}}{6}\left(\frac{2R_{CdS}^2}{2R_{CdS}x + x^2} + \frac{2R_{CdS}^2}{4R_{CdS}^2 + 4R_{CdS}x + x^2} + ln\left[\frac{4R_{CdS}x + x^2}{4R_{CdS}^2 + 4R_{CdS}x + x^2}\right]\right)$$

(Eq. 2.14)

$$V_{DL} = 4\pi\varepsilon_o\varepsilon_r R_{CdS}{}^2\Gamma^2\left(\frac{k_BT}{e}\right)^2\frac{\exp(-\kappa x)}{x+2R_{CdS}} \; ,$$

(Eq. 2.15)

where

$$\Gamma = \frac{8*\tanh(\frac{e\psi_{CdS}}{4k_BT})}{1+\sqrt{1-\frac{2\kappa R_{CdS}+1}{(\kappa R_{CdS}+1)^2}\tanh^2(\frac{e\psi_{CdS}}{4k_BT})}}, \qquad \psi_{CdS} = -15\text{mV}$$

(Eq. 2.16)

$$V_{DP} = \frac{-\mu_{CdS}^2}{2\pi\varepsilon_o\varepsilon_r} * \frac{1}{r(r^2-4R_{CdS}^2)} \; ,$$

(Eq. 2.17)

where

$$r = x + 2R_{CdS} \; , \mu_{CdTe} = \mu_{CdS}.$$

(Eq. 2.18)

Atomistic computer simulations of the assembly of chiral NPs

The modeled NPs have side length of 3.6 nm (10 Cd layers), and they are made of cadmium and sulfur atoms in F43m space group arrangement with a lattice constant of a = 0.582 nm (layer-to-layer distance = 3.16 A). 2, 3, and 4 layers are cut from three of the four vertices to give the NP chirality. Fig. 2.4A shows a model NP with left and right handedness, respectively. The sulfur atoms are colored based on the number of bonding neighbors and their partial charges are assigned based on that. The partial charges was assigned as 0.4e to cadmium atoms, 0.0655e to sulfur with 1 bonding neighbor (S1), -0.185e to S2, -0.35e to S3, and -0.4e to S4.

The NPs were assembled into a flat layer and the structure was solvated in water. The NPs were subsequently charged by homogeneously distributing the charges to all atoms of the NP. Chloride ions were added to the water to neutralize the NP net charges. We simulated the systems in the NAMD software with CHARMM force field under the condition of periodic boundary, isothermal–isobaric (Gibbs) ensemble at T = 300 K maintained by Langevin dynamics with a damping coefficient of γ_{Lang} = 0.01 ps^{-1}, and long range electrostatic computed using particle mesh Ewald (PME) summation. Furthermore, we added bulk VdW coupling to the NPs (beyond the normal VdW cutoff distance) by adding forces to the center of all NPs. Averaged twist angle of the nanoribbons was calculated from the last ~ 5-10 ns of the simulation trajectory.

2.7.3 Additional Figures and Comments

Comment 1: **Self-assembly intermediate stages**. The CdTe NPs aqueous dispersion with a concentration of 0.35 μM was irradiated with RCP or LCP with the intensity of 30 μW, which were lower than the parameters of the previous work,[57] 5 μM and 61 μW respectively. Contrast to the dog-bone shaped NPs intermediate stages in the Ref. [57], with our experiment conditions demonstrated in this paper, NPs were assembled into twisted nanoribbons individually, not the bundled structures (Figs. 2.1A and B).

Comment 2: After illumination with light for 96 h, some nanoribbons became thinner but the twisted geometry was preserved (Fig. 2.6). NPs that did not successfully assemble into nanoribbons, agglomerated into randomized aggregation. Thus, the supernatant from nanoribbons dispersion rarely had absorbance signal (Fig. 2.19). Contrast to the light activated procedure, the NPs dispersion retained its absorbance signal in the dark.

Comment 3: Compared to exposure of 543 nm light, when we used 607 nm wavelength as a light source, the efficiency of chiral selective activation was significantly reduced. The non-activated NPs were dominant around the nanoribbons (Fig. 2.14). These results indicate that effective absorption of light is important for the efficiency of chiral self-assembly of NPs.

Comment 4: **Phase transition from CdTe to CdS.** The characteristic UV-Vis absorption peak of TGA at 276 nm decreased continuously as we increased the illumination time (Fig. 2.20). With the analysis of FTIR spectra from original NPs, purified nanoribbons, and supernatant, we found that typical TGA peaks at 3500 cm^{-1}, 1567 cm^{-1}, and 1421 cm^{-1}, respectively, were significantly decreased in nanoribbons compared to the original CdTe NPs (Fig. 2.3A). A peak from v_{as}(COO-) of carboxyl moieties was observed in the supernatant,

indicating TGA decomposition. XPS spectra of original CdTe NPs and nanoribbons obtained in the S 2p region had peaks at 164.8 eV from thiol groups and 161.6 eV from S in CdS respectively (Fig. 2.21). In Te 3d region, CdTe NPs show peaks at 572.7 eV and 583.5 eV, corresponding to 3d levels of Te in CdTe (Fig. 2.22). The nanoribbons revealed XPS peaks at 576.2 eV and 586.5 eV corresponding to TeO_2. They indicated that illumination resulted in (expected) oxidation of Te^{2-} to Te^{4+}.[57] Besides XPS, the atomic composition of the nanoribbons was also investigated by energy dispersive spectroscopy (EDS) in TEM. The nanoribbons selected by the dark-field TEM (Fig. 2.26) were imaged for the presence of Cd, S, and Te. The EDS element maps in Fig. 2.30 show that the intensity from Cd (green) and S (blue) was significantly higher than that from Te (red). The same conclusion can be reached for line-scanned EDS spectra (Fig. 2.27). In addition, the absorption peaks of CdTe NPs showed a gradual *blue* shift from 532 nm to 510 nm instead of the typical *red* shift of optical features found in many other NPs assemblies (Fig. 2.31). The blue shift in our case is associated with the transition of CdTe to CdS that has wider band gap (2.42 eV) than that of CdTe (1.45 eV).

Comment 5: **CD spectra at various illumination time points.** CD spectra of purified nanoribbons were measured in aqueous dispersions at various illumination time points (Fig. 2.9). After 12 h of illumination, CD signal appeared at 550 nm. As we increased the illumination time to 28 h, a new peak appeared at 700 nm when the peak at 550 nm was decreased. With more than 36h illumination, the samples revealed distinct chiroptical bands at 490, 590, and 700 nm (Fig. 2.1F). More importantly, supernatant showed opposite signs to that from nanoribbons.
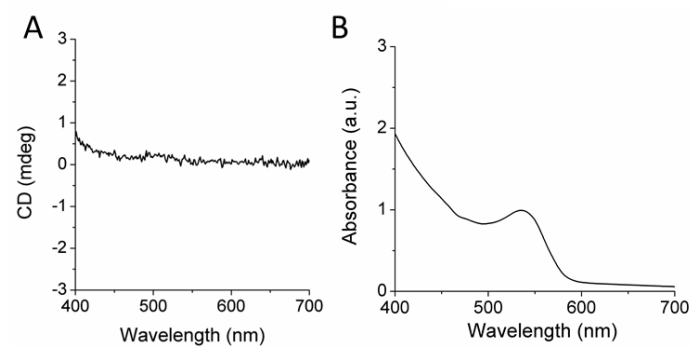
Figure 2.5. CD (A), and UV-Vis absorption (B) spectra of TGA-stabilized CdTe NPs.
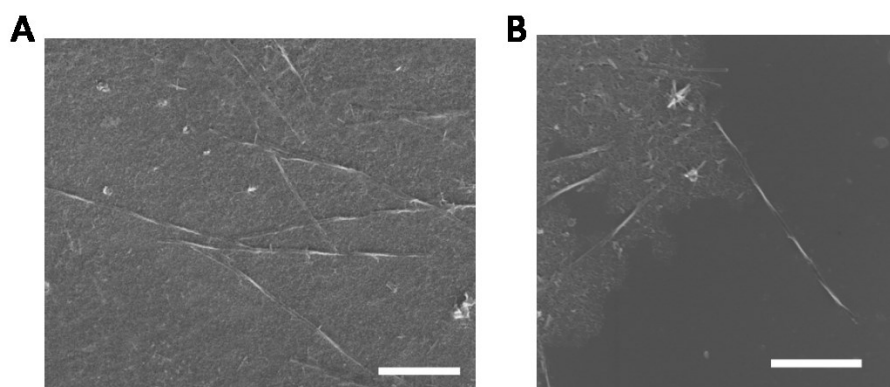
Figure 2.6. SEM images of nanoribbons after exposure to RCP (A) and LCP (B) light for 96 h (scale bars are 1 um).
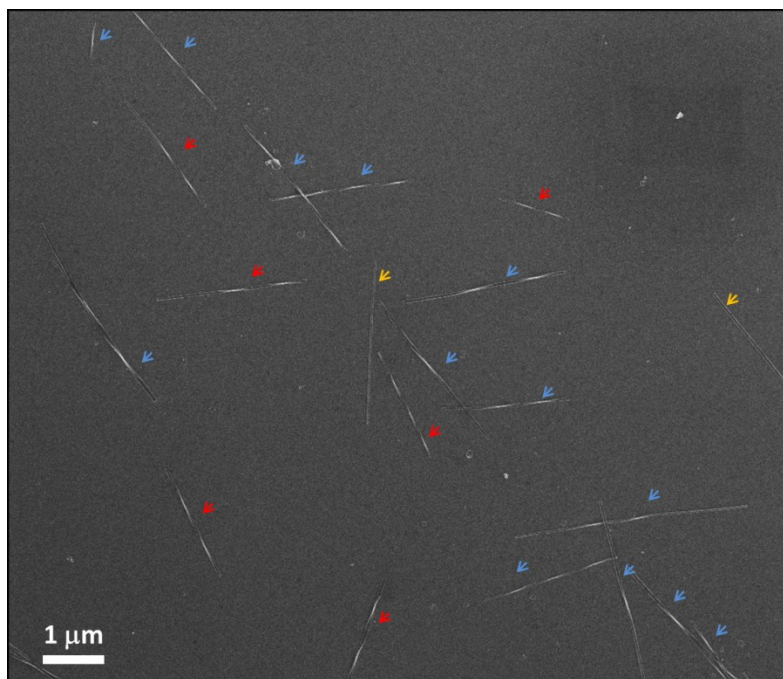
Figure 2.7. SEM image of nanoribbons after exposure to LCP light for 50 h. Blue, red and yellow arrows indicate LH, RH and non-twisted nanoribbons respectively. With total 21 wires in the image, 61.9 % LH, 28.6 % RH, and 9.5 % non-twisted nanoribbons are observed.
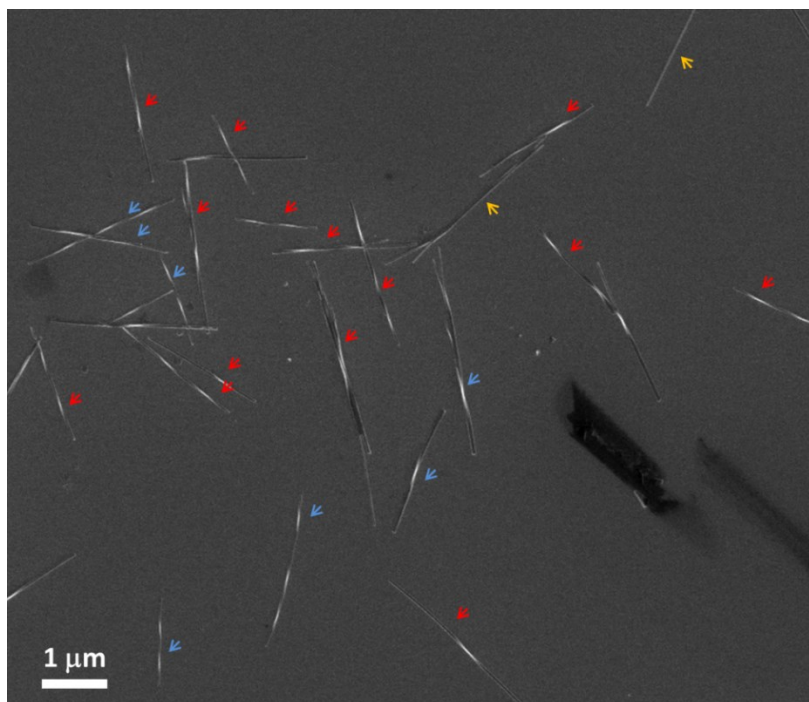
Figure 2.8. SEM image of nanoribbons after exposure to RCP light for 50 h. Blue, red and yellow arrows indicate LH, RH and non-twisted nanoribbons respectively. With total 23 wires in the image, 30.4 % LH, 60.9 % RH, and 8.7 % non-twisted nanoribbons are observed.
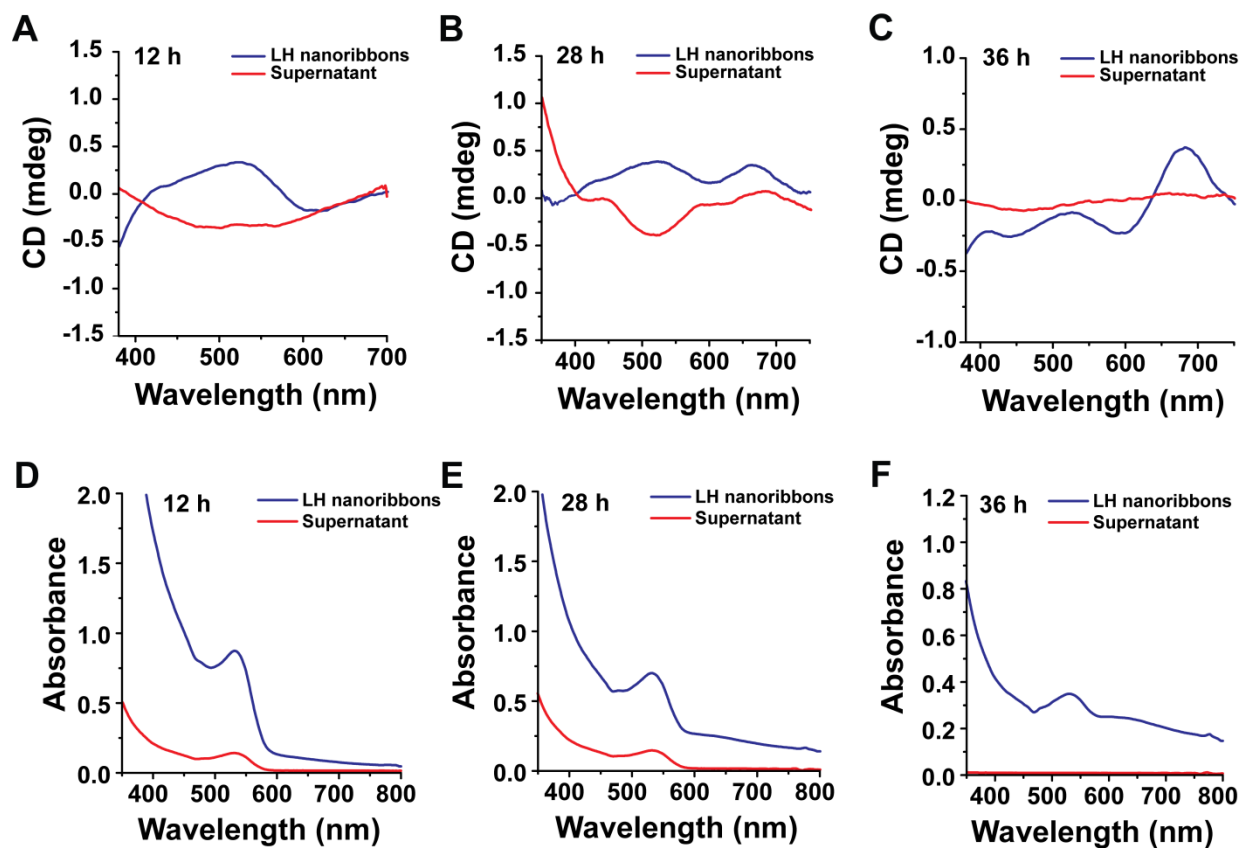
Figure 2.9. CD (A, B and C) and UV-Vis absorption spectra (D, E, and F) of LH nanoribbons and supernatant after illumination of 12h, 28h, and 36h, respectively.
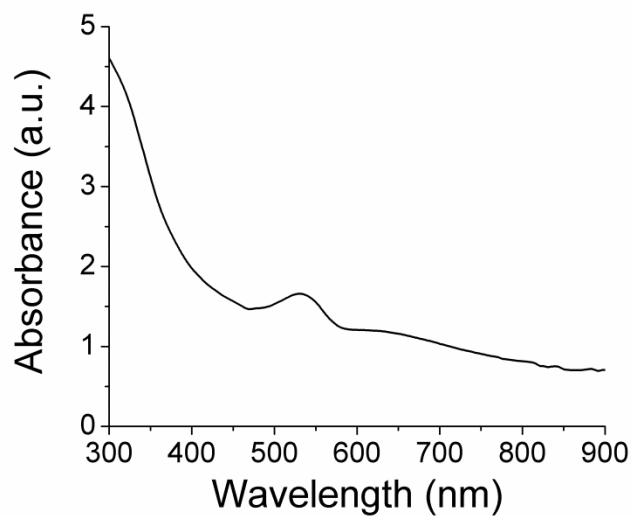
Figure 2.10. UV-Vis absorption spectra of RH nanoribbons corresponding to Fig. 2.1F.
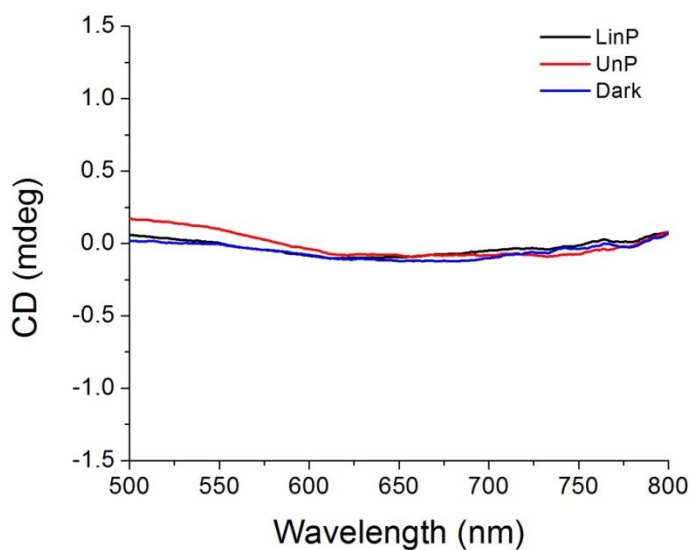
Figure 2.11. CD spectra of nanoribbons synthesized under UnP, LinP and in the dark.
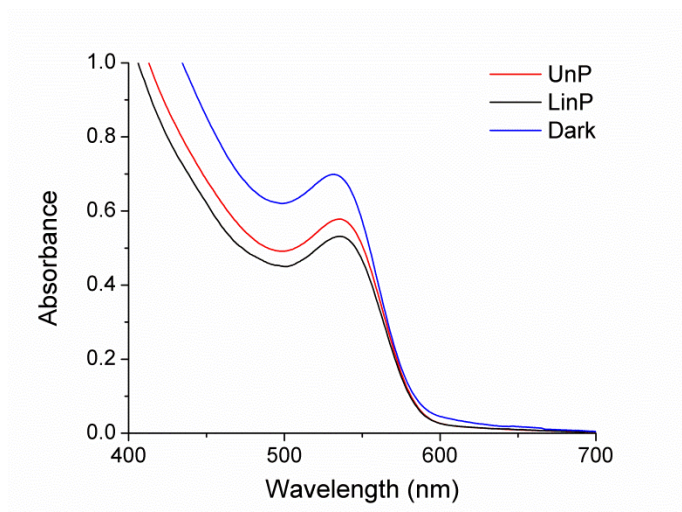
Figure 2.12. Absorption spectra of nanoribbons synthesized under UnP, LinP and in the dark.
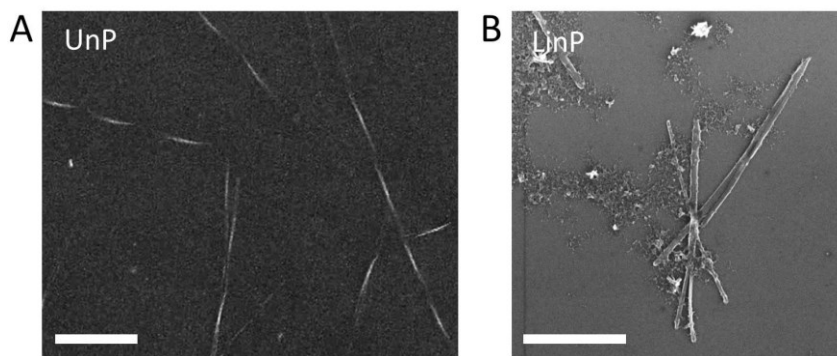
Figure 2.13. SEM images of nanoribbons self-assembled under UnP (A) and LinP (B). Both scale bars are 1 μm. The population of nanoribbons were significantly lower than NPs.
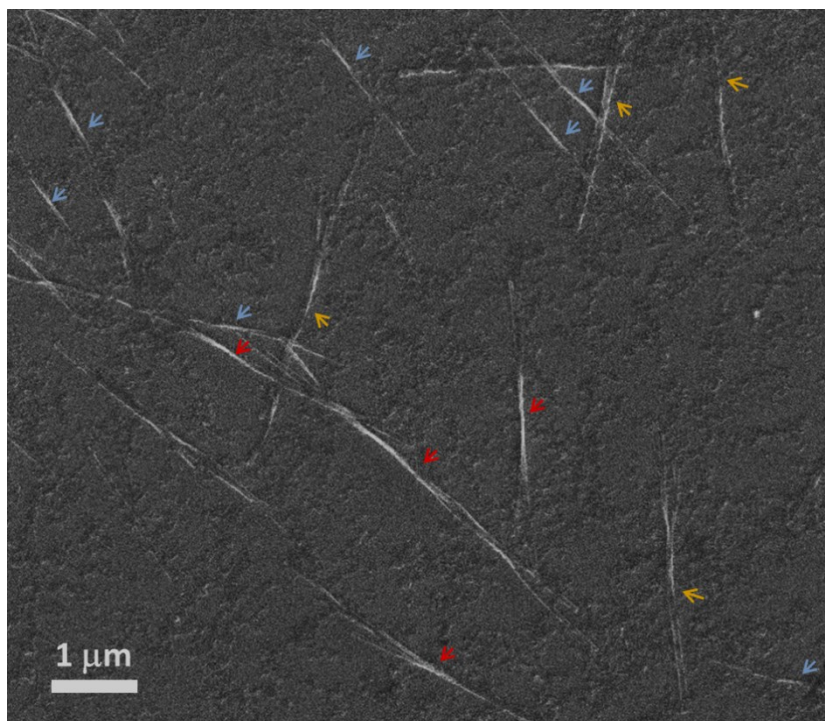
Figure 2.14. SEM image of nanoribbons after exposure to 603 nm LCP light for 50 h. Blue, red and yellow arrows indicate LH, RH and non-twisted nanoribbons respectively. With total 15 wires in the image, 46.6 % LH, 26.7 % RH, and 26.7 % non-twisted nanoribbons are observed.
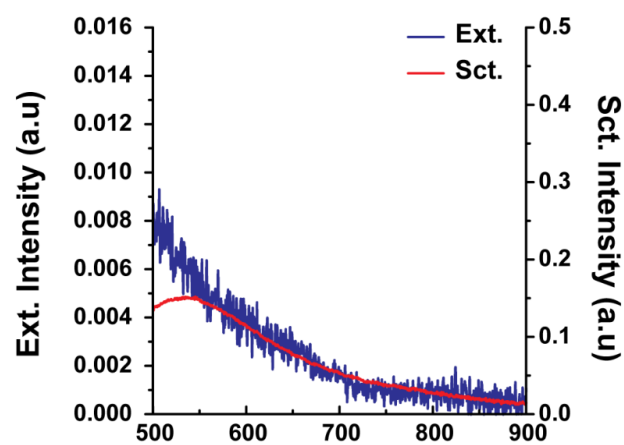
Figure 2.15. Extinction (blue) and scattering spectra (red) of a single nanoribbon assembled under LCP for 50 h.
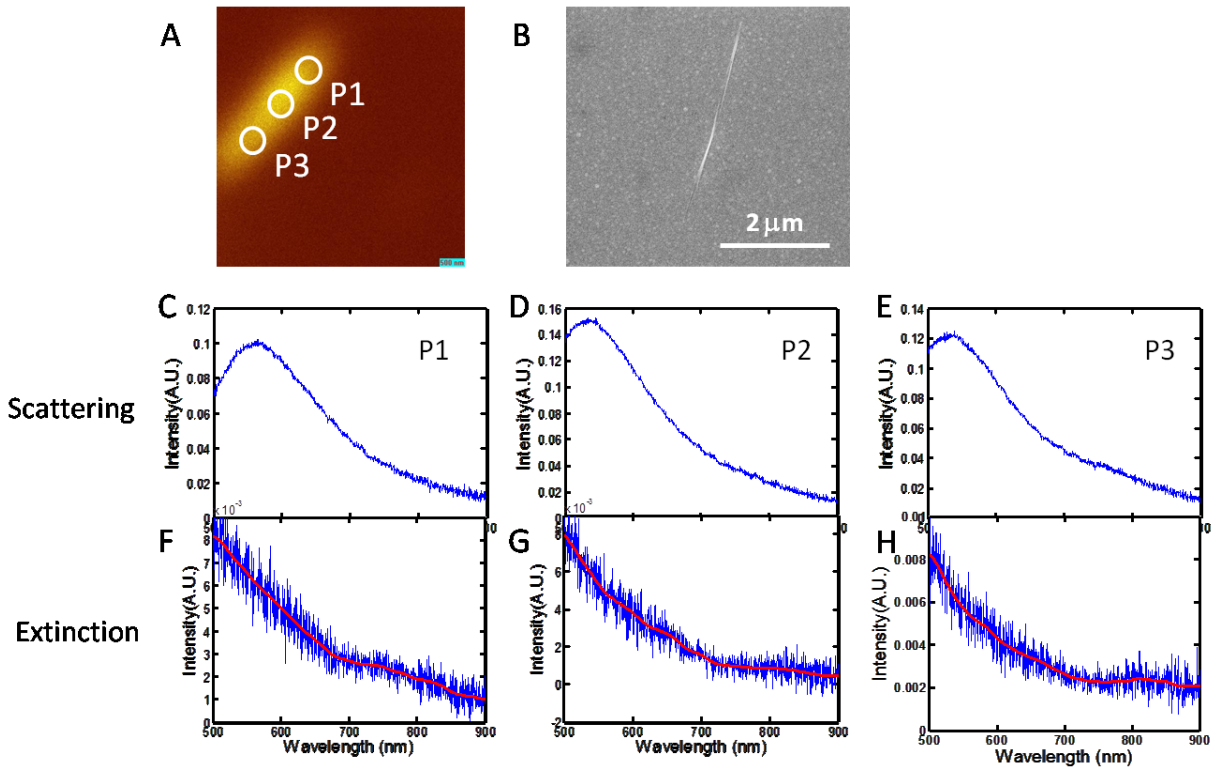
Figure 2.16. A, Optical image of measured LH nanoribbons synthesized by 50 h illumination of LCP. **B,** SEM image of the corresponding nanoribbon in A. **C, D,** and **E,** Scattering spectra from three different positions of the nanoribbon: P1, P2 and P3 as indicated in A. **F, G,** and **H,** Extinction spectra obtained from P1, P2 and P3.
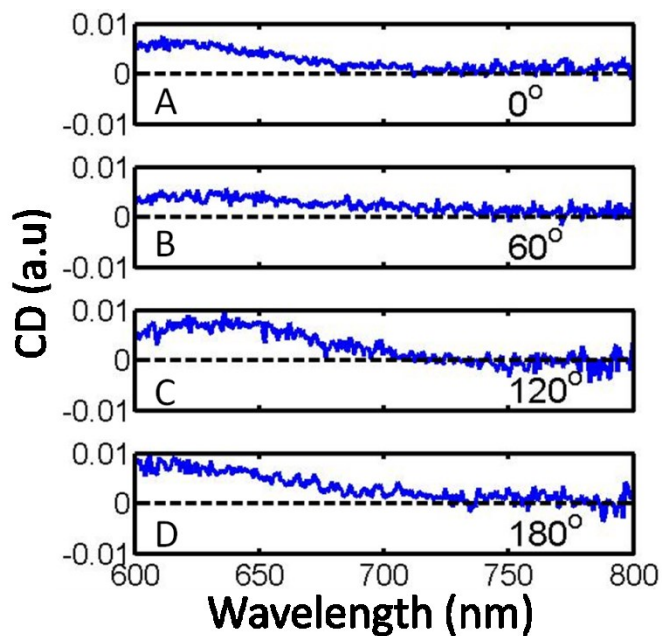
Fig 2.17. CD spectra of a single nanoribbon measured with the long axis of the nanoribbon orientated at 0° (A), 60° (B), 120° (C), and 180° (D) relative to the lab axis.
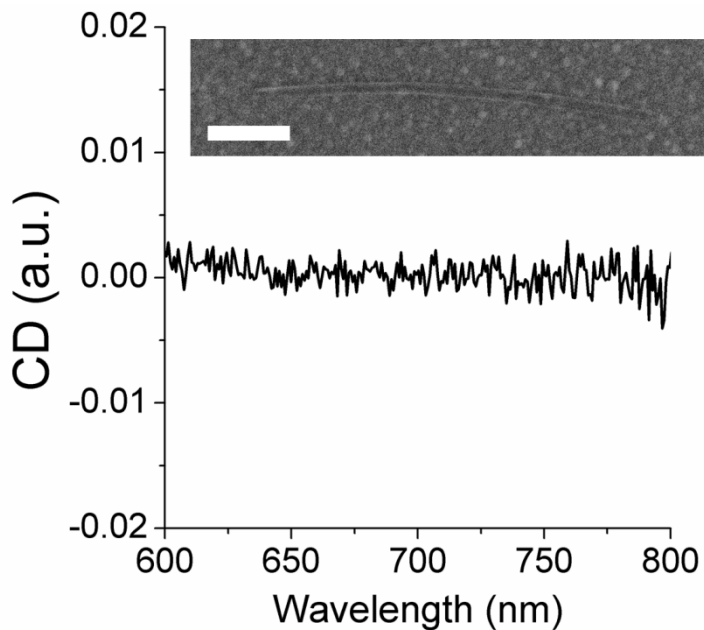
Fig 2.18. CD spectra of a single non-twisted nanoribbon. Inset: SEM image of the corresponding nanoribbon. Scale bar is 500 nm.

50
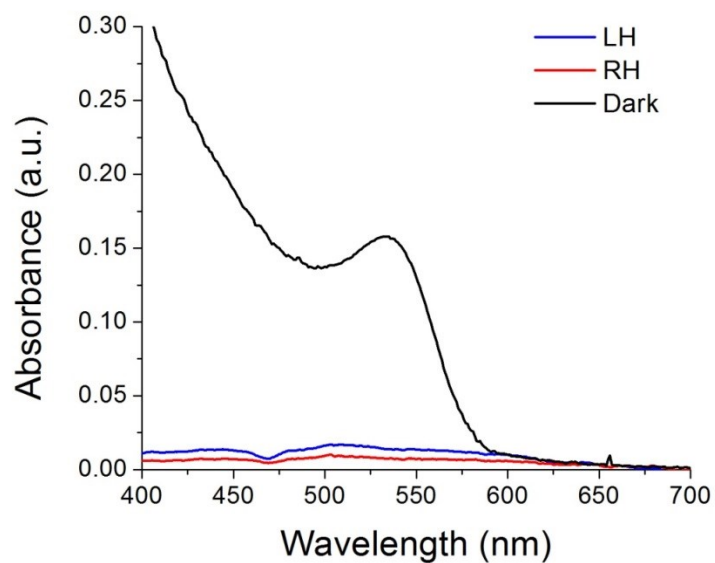
Figure 2.19. UV-Vis absorption spectra of supernatant separated by centrifugation from nanoribbons obtained with LCP (blue), RCP (red) illumination, or incubation in the dark (black) for 96 h. As shown in SEM images (Fig. S4), NPs present in dispersions aggregate around nanoribbons as a result of centrifugation, so that few NPs remain in the supernatant. Without exposure of light, NPs were well-dispersed in the solution.
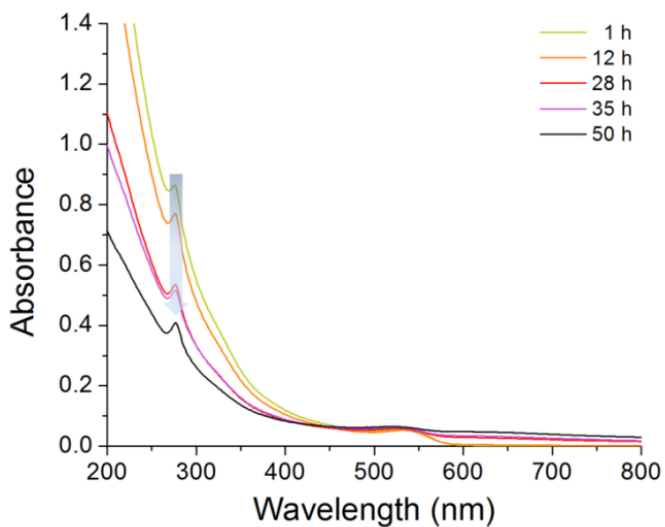
Figure 2.20. UV-Vis absorption spectra obtained for NP dispersions after illumination with RH
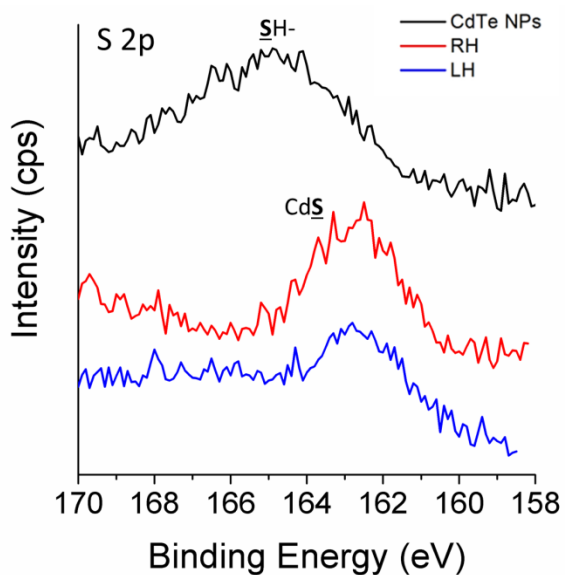
light for different lengths of time.

Figure 2.21. XPS spectra of S 2p region obtained for CdTe NPs, LH, and RH nanoribbons obtained after 50 h of illumination.
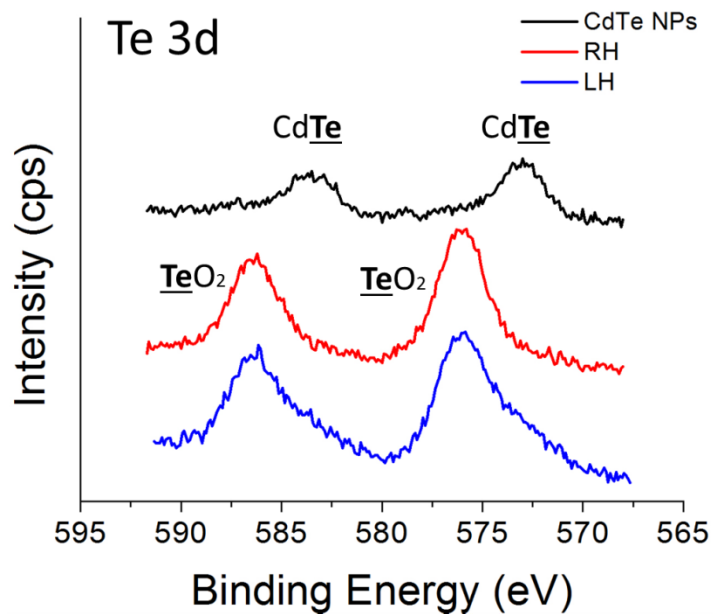
Figure 2.22. XPS spectra of Te 3d region obtained for CdTe NPs, LH, and RH nanoribbons obtained after 50 h of illumination.

Table 2.1. Atomic percentage of elements in nanoribbons obtained by EDS (Fig. 2.26-2.28).

Element	Atomic percentage, %
Cd L	51.5
S K	47.3
Te L	1.2

Table 2.2. Atomic percentage distributions of elements in NPs obtained by EDS (Fig. 2.29).

Element	Atomic percentage,%
Cd L	49.3
S K	14.5
Te L	36.2
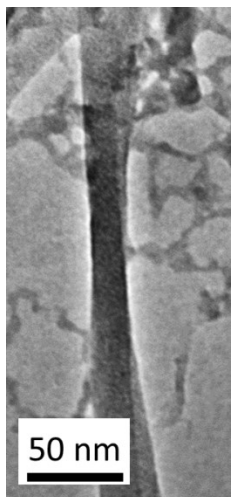
Figure 2.23. TEM image of LH nanoribbon obtained after 50 h of illumination.
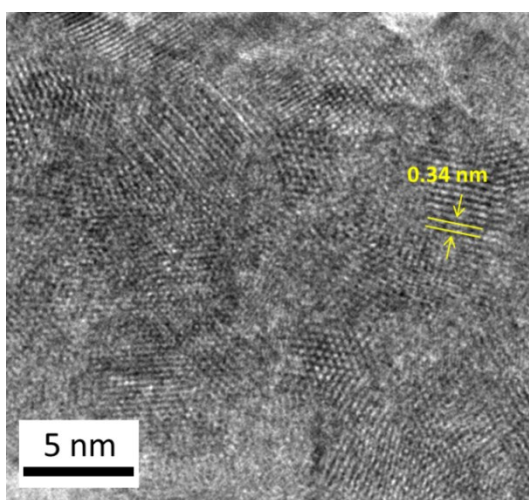
Figure 2.24. High resolution TEM image of the twist region in LH nanoribbon obtained after 50 h of illumination. The lattice spacing typical for CdS was observed.
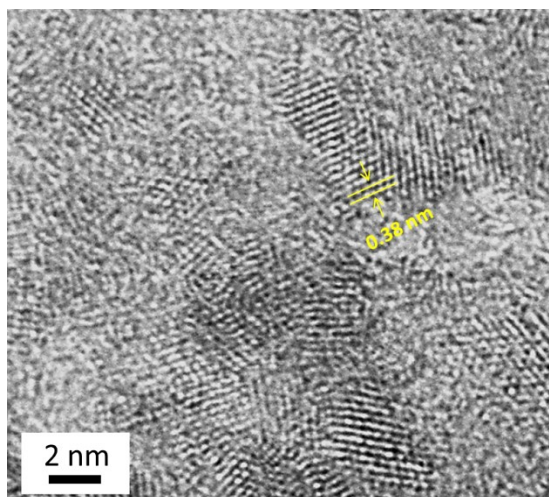
Figure 2.25. High resolution TEM image of the original CdTe NPs. The lattice spacing typical for CdTe was observed.
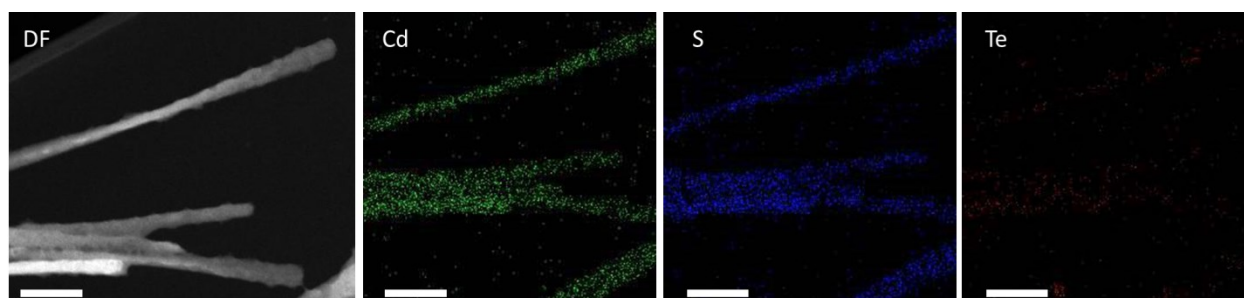
Figure 2.26. Atomic mapping images of RH nanoribbon obtained after 50 h of illumination time. (All scale bars are 500 nm).
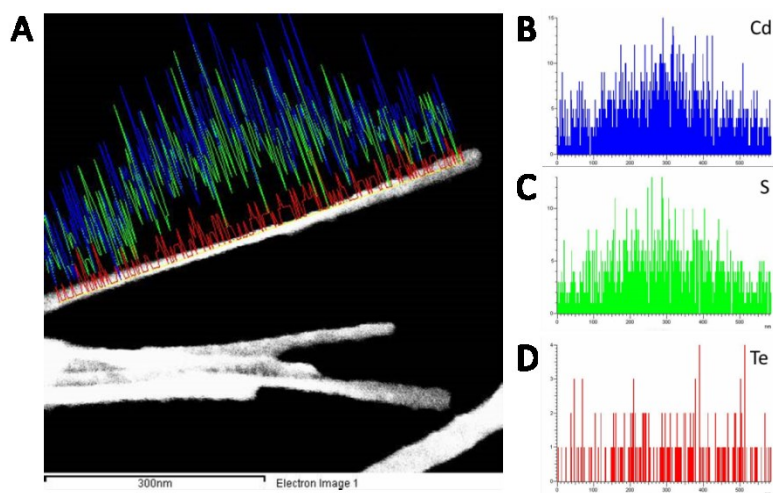
Figure 2.27. Line-scanned EDS spectra from a single RH nanoribbon obtained after 50 h of illumination.
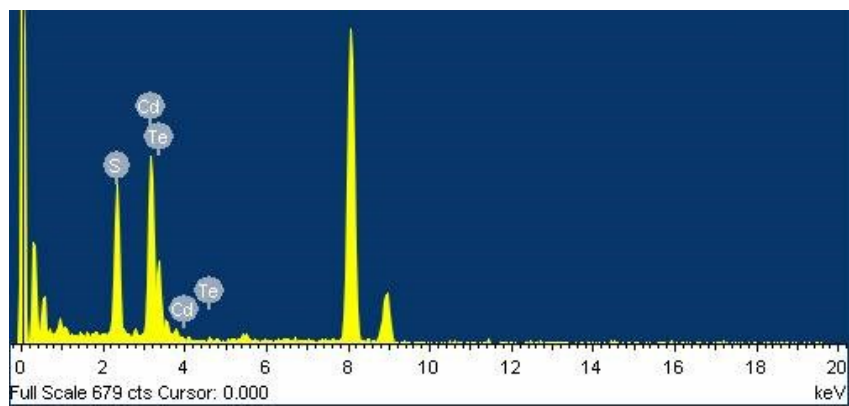
Figure 2.28. EDS data of RH nanoribbon obtained after 50 h of illumination time.
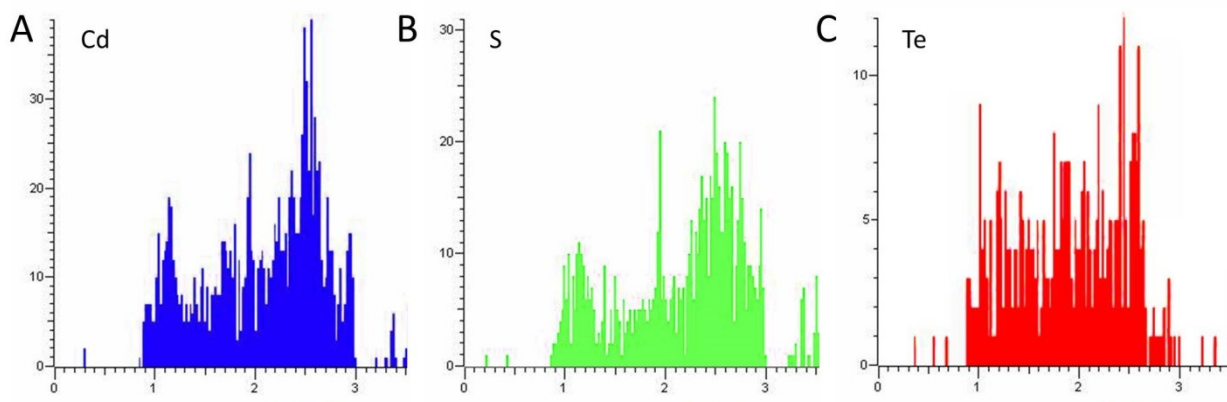
Figure 2.29. EDS spectra from CdTe NPs.
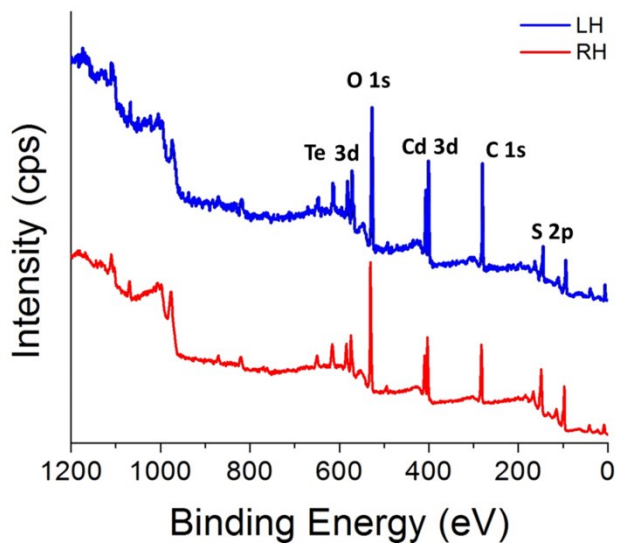
Figure 2.30. XPS survey spectra of LH and RH nanoribbons obtained after 50 h of illumination.

57
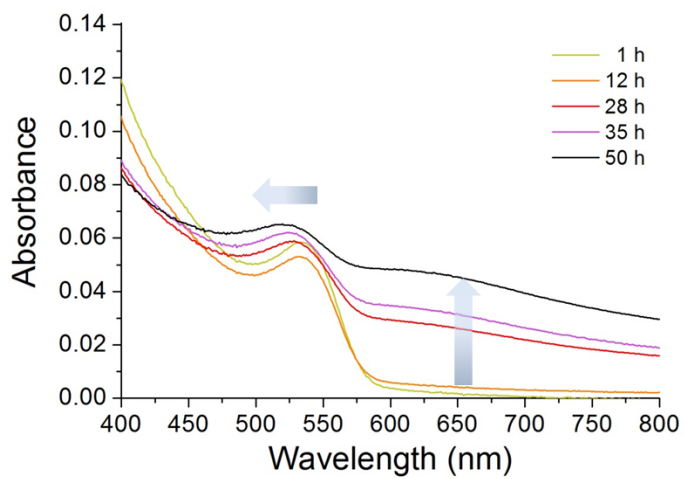
Figure 2.31. UV-Vis absorption spectra of TGA-stabilized aqueous NP dispersions obtained for various illumination times.
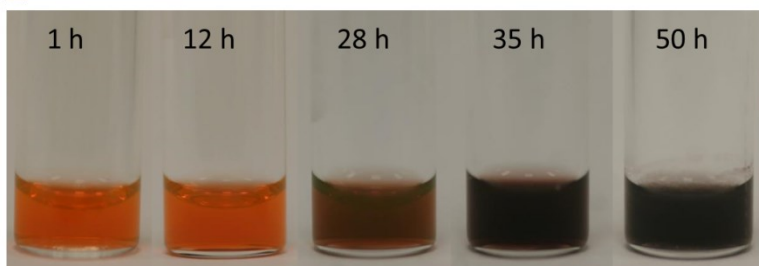
Figure 2.32. Photographs of the NP dispersions taken for various RCP illumination times.
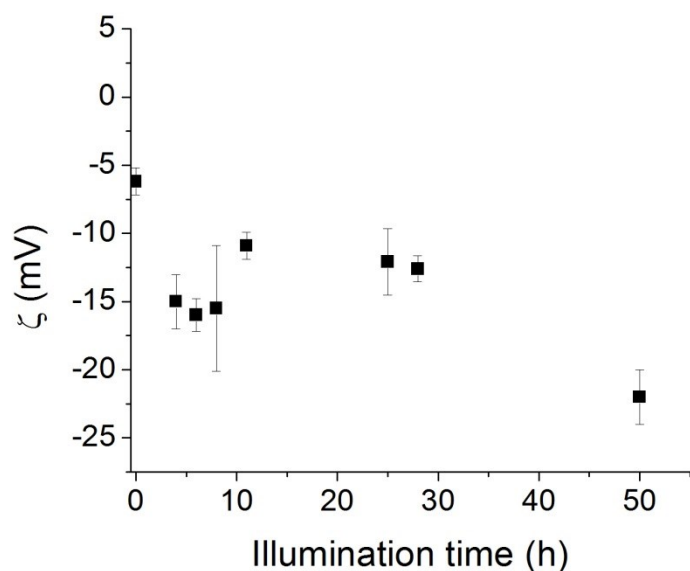
Figure 2.33. Electrokinetic zeta potential (ζ) for NPs and nanoribbons for various RCP illumination times.
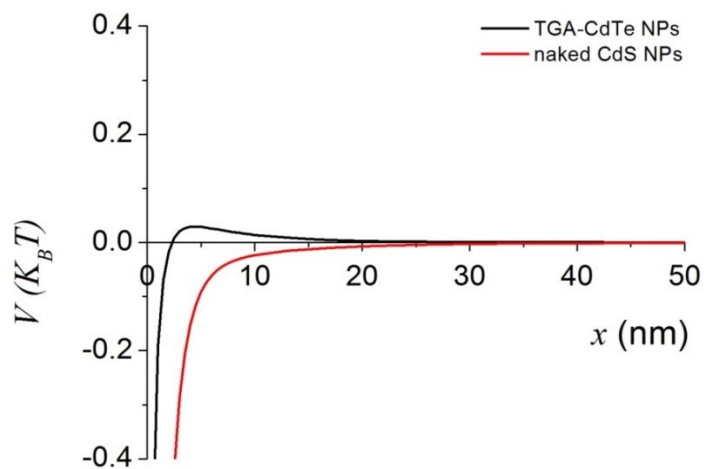
Figure 2.34. Pair potential calculated based on E-DLVO theory for TGA capped CdTe NPs and surface ligand-free ("naked") CdS NPs.
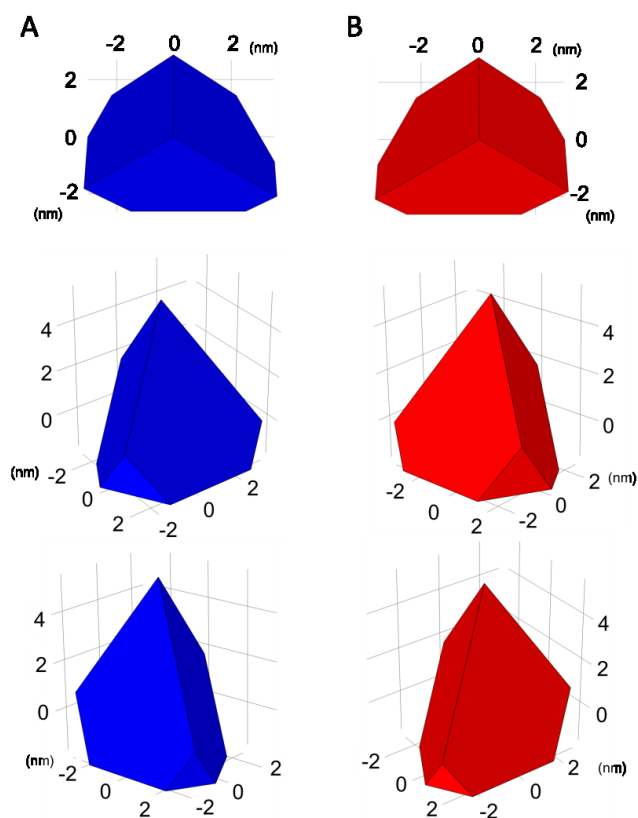
Figure 2.35. Additional views of COMSOL models of *L*-CdTe NP (A) and *R*-NP (B) used in ME-FEM simulation of CD spectra in Fig. 2.2D. These images are complementary to those in Fig. 2.2B.
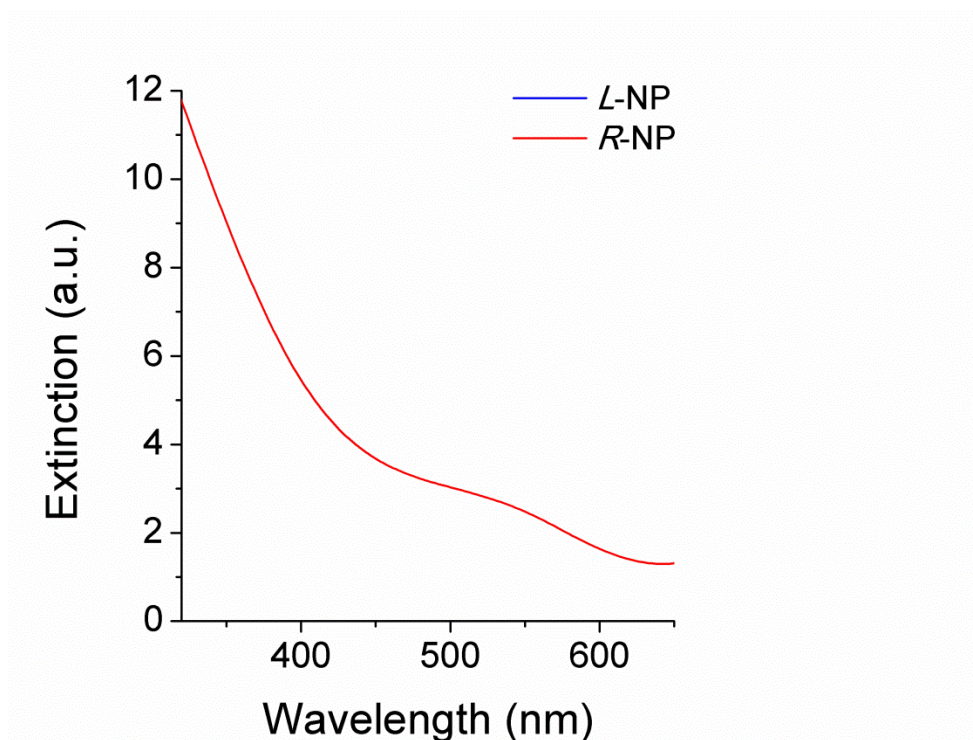
Figure 2.36. Simulated extinction spectra for *L/R*-NPs. The graphs were superimposed.
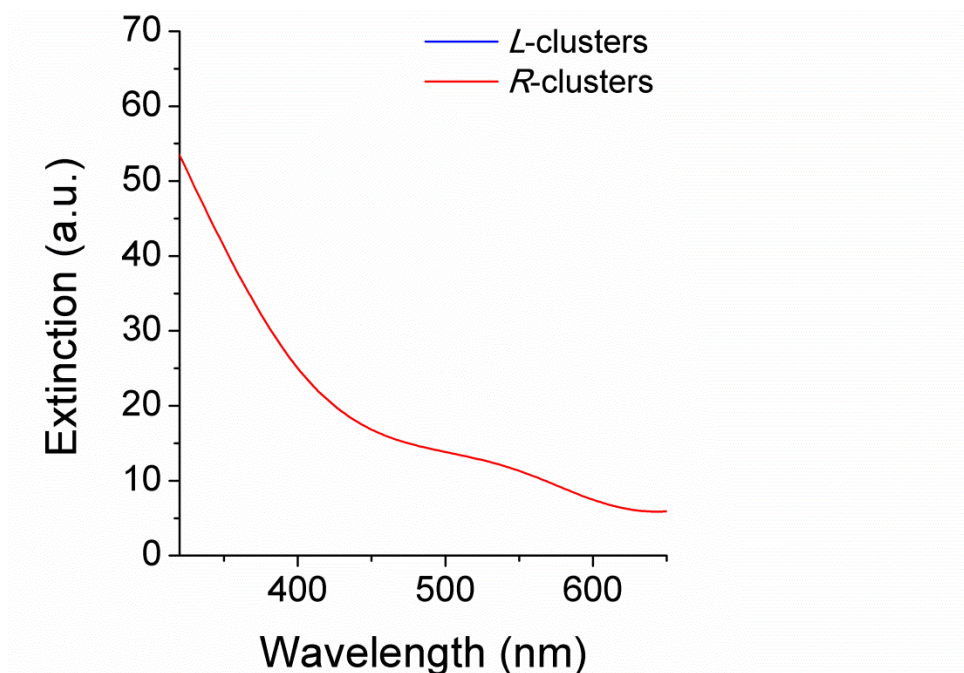
Figure 2.37. Simulated extinction spectra for*L/R*-clusters. The graphs were superimposed.
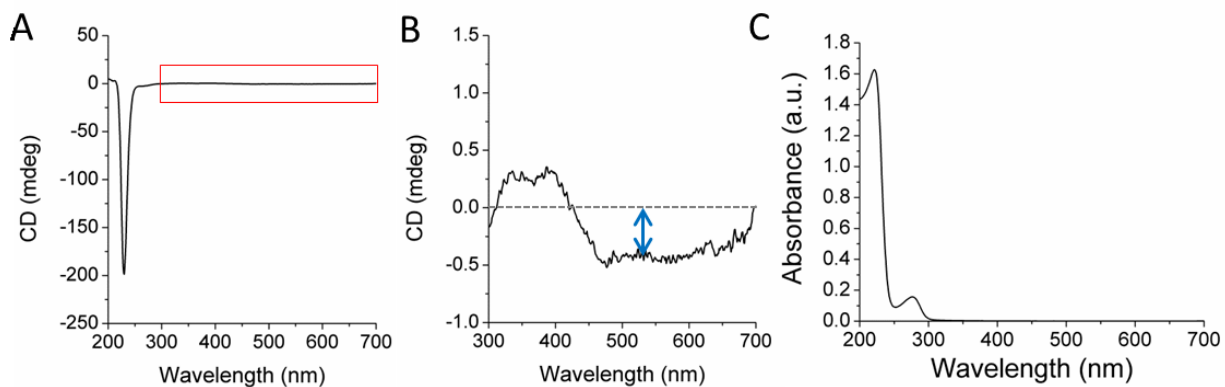
Figure 2.38. (A) Complete, (B) band-specific CD spectra highlighted in (A) with the red box, and (C) absorbance spectra of BSA .
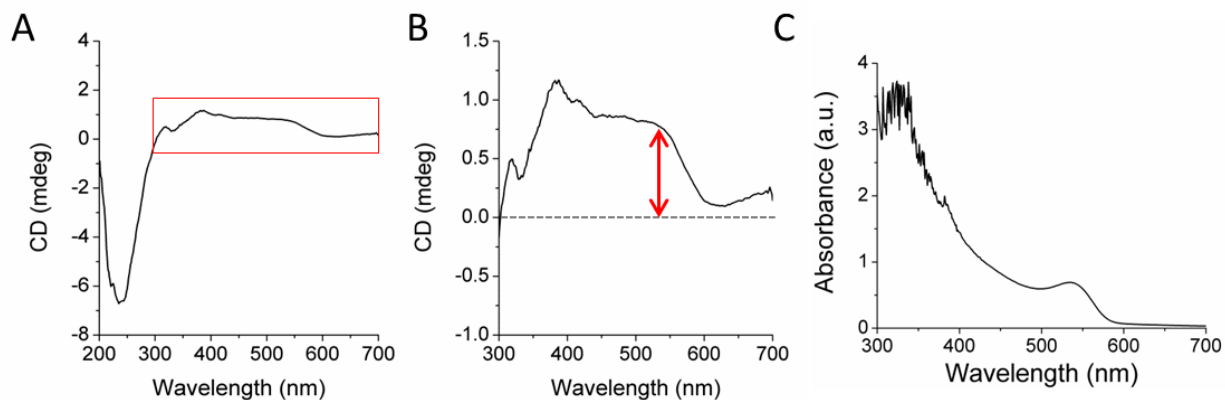
Figure 2.39. (A) Complete, (B) band-specific CD spectra highlighted in (A) with the red box, and (C) absorbance spectra of CdTe NPs after separation using BSA as an enantioselective agent.
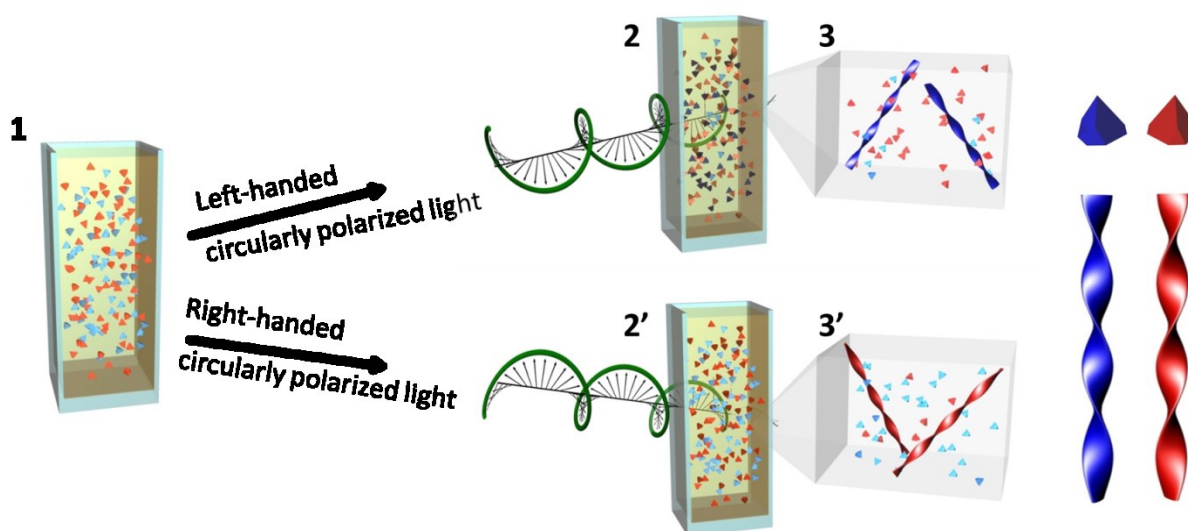
Figure 2.40. Schematics of the CPL–induced self-assembly process. 1. Racemic mixture of CdTe NPs are prepared. **2.** LCP selectively activates LH NPs. **2'.** RCP activates RH NPs. **3.** The excited LH NPs are self-assembled into LH nanoribbons. **3'.** RH NPs are self-assembled into RH nanoribbons

Comment 6: Light sensitivity of NPs is common. For a few examples other than CdTe, Jin et al.,[93] demonstrated controlling Ag NPs shapes using a photoinduced procedure where an aqueous dispersion of spherical Ag NPs were illuminated with a conventional 40W fluorescent light. After 70 h of irradiation, the spherical shapes converted into prisms. Their Ag prims showed unusual optical activities such as Rayleigh light-scatter in the red, and not scattering in the blue, which is common for NPs.

The sizes and polymorphs of NPs are also sensitive to the photoreaction rate.[94] Au NPs (3 ~ 30 nm) on TiO_2 were used for photocatalytic hydrogen production from ethanol. The size and polymorph (anatase versus rutile in the case of TiO_2) depended on how the photoreaction rate was controlled.

CHAPTER III

Chiral Growth of Gold Nanoparticles Driven by Circularly Polarized Light

3.1 Abstract

Examples of chemical reactions affected by spin angular momenta of circularly polarized photons are rare and display low enantiomeric excess.   High optical and chemical activity of nanoparticles (NPs) should facilitate the transfer of spin angular momenta of photons to nanoscale materials but such processes are rarely known. Here, we demonstrate that illumination of Au precursors in the presence of citric acid with right- (left-) handed circularly polarized light (CPL) induces the formation of right- (left-) handed chiral Au NPs. Linearly polarized light led instead to Au NPs dispersions that do not possess optical activity. The ability of Au NPs to retain the polarization information of incident photons shows versatile usage of CPL to synthesize chiral materials and open a door to understand the origins of homochirality of nature.

3.2 Introduction

Synthesis of metallic nanoparticles (NPs) with chiral structures is one of the intriguing and inspiring phenomena in nature due to its optical activities in the metal-based electronic transitions in the visible region. Since nano-scale materials have stronger interactions with light energy, circularly polarized light (CPL) has been suggested as a new tool to transfer spin angular momenta of photon to matter, retaining the chiral information as a permanent structure. [95]

The photoinduced shape transformation of Ag NPs is a well understood example of a photomorphic reaction. [96,97] The unpolarized light was used as a convenient tool to dynamically manipulate the original spherical shape of Ag NPs into nanoprisms. In this case, the transformation procedure was a two-dimensional coalescence mechanism. Here, we demonstrate three-dimensional deformation of NPs via transferring circularly polarized photon energy to metal precursor solution.

3.3 Seed-free Chiral Au NPs Formation using CPL

Gold(III) chloride ($HAuCl_4$) and citrate were used as Au precursors and achiral capping agent. In a quartz cuvette, 2 mL aqueous mixture of $HAuCl_4$ and citrate was placed and irradiated by left- (LCP) or right-handed circularly polarized light (RCP) with a wavelength of 543 nm. After 50 min illumination, the pale yellow color of the solution turned into red which indicates the formation of plasmonic Au NPs. The optical activities of obtained solutions were examined by circular dichroism (CD) spectrometer that measures absorption differences between LCP and RCP ($\Delta\varepsilon$ (CD) $= \varepsilon_{LCP} - \varepsilon_{RCP}$). Depends on the handedness of the incident CPL, samples showed mirror-imaged opposite CD bands (Fig. 3.1A) at the plasmonic resonance region that in good agreement with UV-Vis absorbance spectra (Fig. 3.1B). We observed the

morphology of obtained NPs using transmittance electron microscopy (TEM) (Fig. 3.1C and D). The shape of NPs was not a typical sphere but v-like twisted structures that were about 10 nm.

The CPL photolysis of $HAuCl_4$ in water can be described as a well-known sequence of reactions resulting in reduction of AuIII to Au0 and Au colloid formation.[98] Our experimental results suggest that circularly polarized momenta of photons can be transferred to the nano-geometry during the sequential light-induced reduction procedures. The photon energy effects were examined by checking the intermediate stages of the chiral growth of Au NPs. At various illumination times, we measured TEM images and CD spectra (Fig. 3.3) After 5 min of illumination, spherical ~ 2 nm NPs were observed, and with continuous illumination, the NPs were self-assembled into anisotropical structures. With the shape transformation and the size incensement to about 10 nm, CD and UV-vis absorbance bands arose accordingly at around 550 nm (Fig 3.3B and C). To our knowledge, this is the *first reported example* of transferring circularly polarized information of photon to seed-free solution to synthesize chiral metal NPs.

The appearance of optical dichroism due to NP shape deformation depends on polarized directions of irradiated laser is also an example showing the ability of NPs to retain polarization information. [99,100] Ag and Au NPs imbedded in glass composite transformed their shape with laser irradiation because the nanoparticles are ionized by the laser, and locally concentrated metal ions near the clusters migrated with the photon energy, and then coalescence. [99–101] In our case with CPL illumination, (1) Au precursors reduced to Au seed colloids, and while citrate providing hot electrons on the surfaces, (2) Au colloids assembles into anisotropic shapes accordingly depend on the handedness of the light. To confirm the circular momentum effect on the gold ion reduction reaction, use used linearly polarized light (LPL) as the illuminating source

(Fig. 3.4). After 50 min of illumination, the pale-yellow solution again turned into red color, but the solution did not show CD signals where it had an absorbance band (Fig 3.4A and B). We observed the shape of the obtained Au NPs that was elongated in 2-dimensional directions (Fig 3.4C). This result also confirms transformation of polarization information of photon to nano-geometry.

Since TEM only measures 2-dimensionally projected images, we carried out 3-demensional (3D) TEM tomography imaging of obtained NPs. The reconstructed images revealed complicated structures with pores and snags formed by small NPs assembly. Due to the complexity, it is hard to recognize representative handedness (Fig 3.2A and 2B) of each NPs. To confirm the chiral preference on the structures, we carried out computational calculation of their optical activities. Typically, computer calculation is demonstrated using simplified modeled structure. However, since our obtained structures did not show representative trends, we used experimentally obtained 3D information for the calculation.

We imported 3D tomographic geometries into wave-optics module of COMSOL Multiphysics 5.1, thus the simulated model had the same shape of the selected real particles. With our knowledge, this is the *first approach* using experimentally obtained 3D information for calculations. Despite the complicated structures, the individual NPs showed mirror-imaged like spectra (Fig 3.2). Considering that the experimental spectra was obtained from NPs dispersions that contains un-uniform shapes and sizes, calculated spectra of two individual NPs is generally well agreed with the experimental results. (Fig 3.3). It also confirms that the optical activity of Au NPs is originated from chiral structures that developed by circular momentum of photons.

3.4 Conclusion

In conclusion, we demonstrated a sustainable method to produce chiral Au NPs by illuminating CPL to metal precursor contained seed-free aqueous solutions. The produces Au NPs showed opposite optical activities depends on the handedness of illuminated CPL. Their chiral structures and optical activities were confirmed by 3D tomography imaging and theoretical calculations.
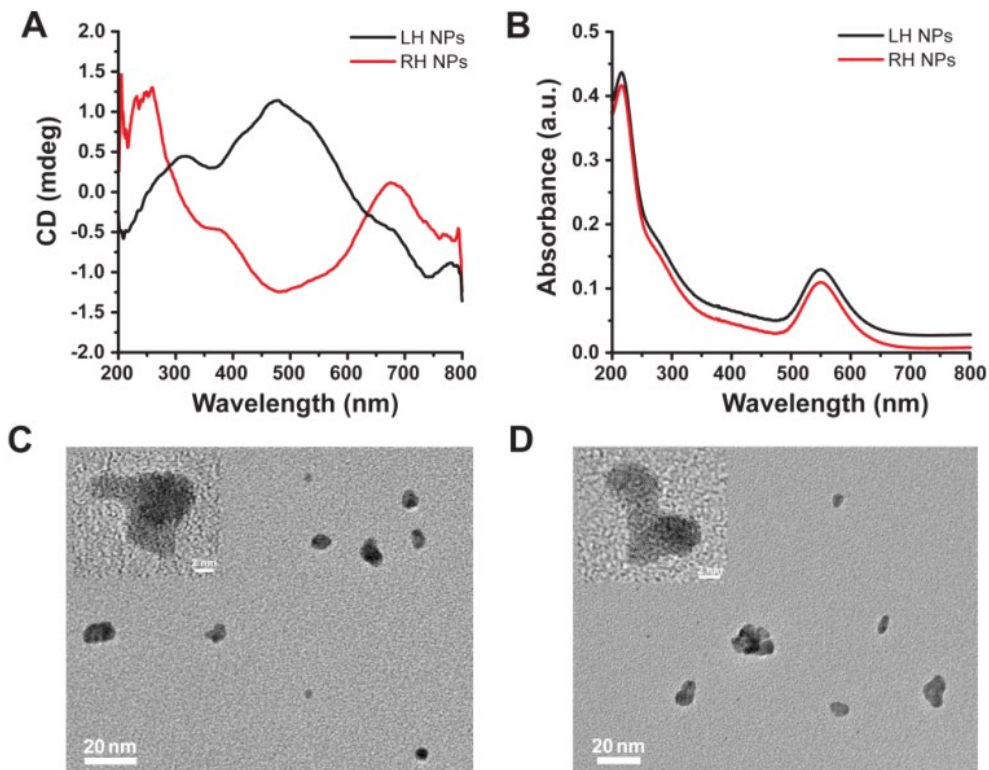
Figure 3.1. A and B, CD (A) and UV-Vis absorbance(B) spectra of LH (black) and RH (red) chiral gold NPs. C and D, HR-TEM images of Au NPs obtained after 50 min illumination of LCP (C) and RCP (D).
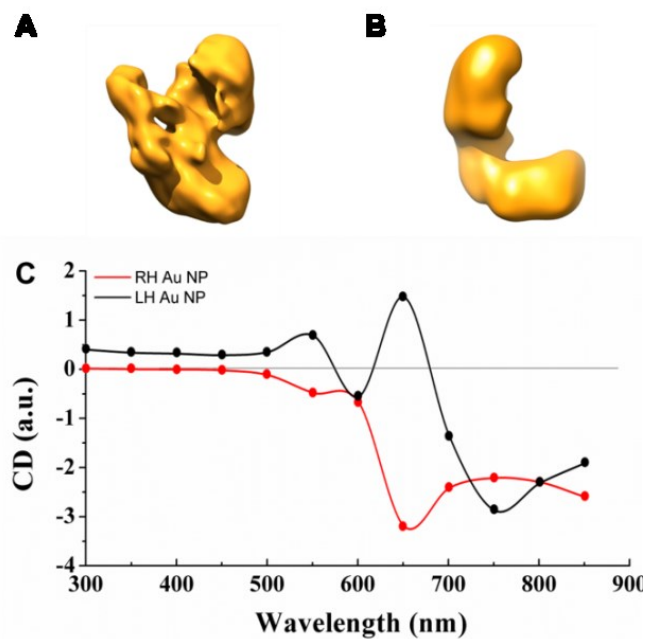
Figure 3.2. A and B, experimentally obtained TEM tomography reconstructed images of LH (A) and RH (B) gold NPs. C, theoretically calculated CD graph.

3.5 Supplementary Information

3.5.1 Experimental Methods

An aqueous solution was prepared by dissolving HAuCl4 and citrate 2.5 mM each in E-pure water. The solution was places in a dark room, and then exposed to CPL for 50 min. As NPs were formed, the pale-yellow color turned to red color. The obtained NPs were washed to remove remained salts by gentle centrifugation (bench-top centrifuge, 3000 rpm, 3 min) and re-dispersion in E-pure water. The morphology was analyzed by using transmission electron microscopy (TEM, JEOL 3011), and CD spectra were obtained by a JASCO J-815 instrument.

3.5.2 Computation of Chioptical Properties

We compute chiroptical property of Au nanoparticles by importing experimental 3D tomographic geometries into wave-optics module of COMSOL Multiphysics 5.1. Since we directly imported the 3D images obtained by TEM tomography, the simulating model had a same dimension and shape of the selected real particles. The imported structures were assigned as a domain of which material is gold and the environment was set as water whose refractive index is 1.33. Optical constants of gold were adapted from Ref [102]. Using the finite element method, we solved the frequency domain form of Maxwell's equations in the optics module. We obtained scattering and absorbance of the gold structures when they interact with left- and right-hand circularly polarized electromagnetic waves of which wavelength ranged from 300 nm to 850 nm with 50 nm interval. To remove directionality problem of the object in the model, we averaged CDs simulated for 144 different propagation direction defined by two spherical angles with a step of $\pi/6$. At the first glance, their shape looked irregular at first glance, however, the simulation results clearly show that these two geometries of each particle showed distinctive opposite chirality and even fit tendency of experimental CD signals. Note that the RH CD signal is amplified five times than original to offer better comparison of data. Considering size and volume difference between RH and LH particle, this intensity difference can be rationalized. In same context, although positions and intensity of peaks are different in some degree from, given the singularity of the selected 3D imaged particle and breadth of the size distribution, computed CDs are accurately matched with experimental observations.

3.5.3 Additional Figures
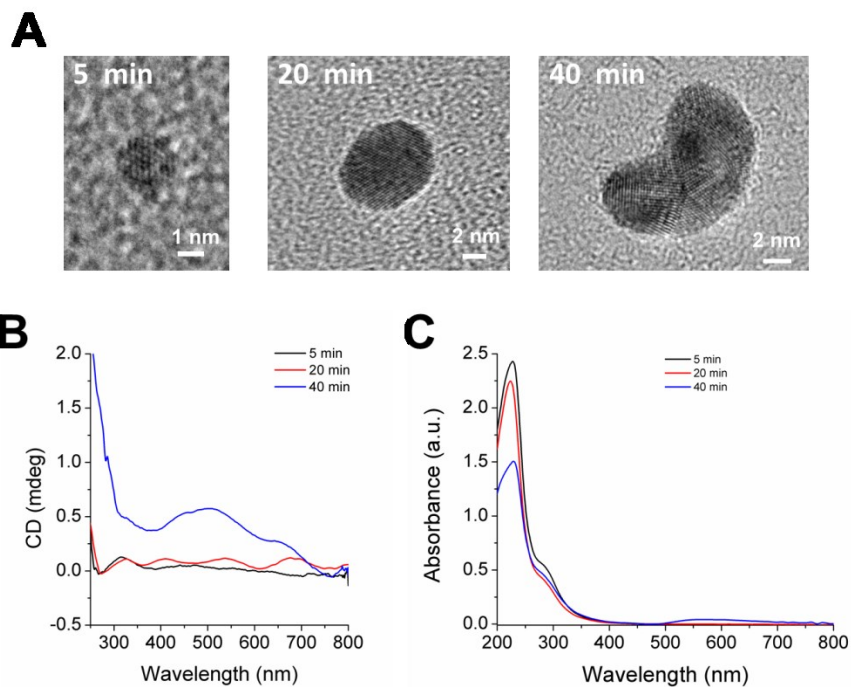
Figure 3.3. TEM images (A), CD (B) and absorbance (C) graphs of chiral nanoparticles at various illumination time points.
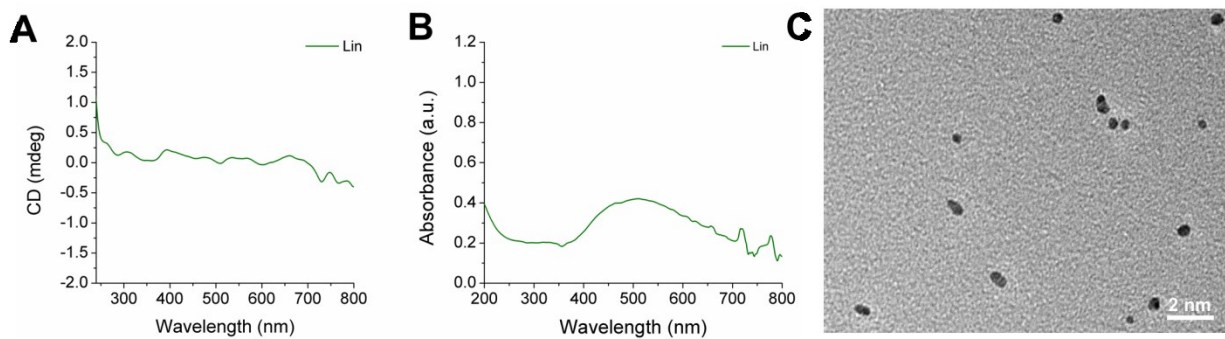
Figure 3.4. CD (A), absorbance (B) graphs and TEM images (C) of gold NPs illuminated by linearly polarized light for 50 min.

CHAPTER IV

Chiroptical Activity and Field modulated Optical Transmission of Paramagnetic Nanoparticles

4.1 Introduction

Optical materials that combine chirality and magnetism are essential for spintronics, magnetooptics, magnetochemistry, and chiral catalysts [7,8] as they allow one to modulate light beams, excited states, and chemical processes using magnetic fields. The nexus of chirality and magnetism is central to the emergence of skyrmions, spin catalysis, and the origin of Earth's life homochirality [3–5], thus representing some of the most pressing recent and long-standing problems of physics, chemistry, and biology. For all these physicochemical phenomena, it is essential to increase the coupling of the photon's magnetic field with the magnetic moments of electrons in chiral matter, which is expected to markedly increase the chiroptical activity and first/second order magnetoptical phenomena, such as the Faraday effect, magnetic circular dichroism, and magneto-chiral dichroism [11,14,22–26,103]. However, optical materials that combine large magnetic moments and chiral asymmetry are uncommon [13]. The most frequently

encountered examples of such chiro-magnetic materials are typically based on complexes of transition metals [9,10]. However, even for optical centers with rare-earth *f*-orbitals accommodating multiple unpaired spins, the long-distance spin-coupling, which enhances the magnetic field effect on electronic transitions, requires low temperatures of T=5-7 K [9,10] due to chiral organic ligands increasing the spacing between magnetic metal centers.

Chiral inorganic NPs [16,41,104,105] and their assemblies [103,106] provide a new toolbox for the design of materials combining chirality and magnetism. While the optical transitions in rare-earth coordination compounds involve localized molecular orbitals, the optical transitions in NPs may engage orbitals involving thousands of atoms, as does their chirality [107]. Unlike coordination compounds, the optical 'center' responsible for chiroptical properties in inorganic NPs becomes orders of magnitude larger in volume compared to coordination compounds from *f*-metals. Importantly, the chiral NPs may also show distorted crystal lattices [108,109] and exhibit (super)paramagnetism [103,110–112]. This set of characteristics of NPs enables enhancement and the spectral tuning of multiple chiroptical properties [113,114]. In this study, we shall focus on the first order effects of magnetic fields on light absorption and circular dichroism (CD). The importance of magnetic properties of NPs for the absorption of circularly-polarized photons can be easily inferred from the quantum mechanical parameter known as rotational strength, *i.e.*, $\boldsymbol{R_{0a}}$, which can be calculated as

$$\boldsymbol{R_{0a}} = \text{Im}[<\Psi_0|\hat{\mu}|\Psi_a>\cdot<\Psi_a|\hat{m}|\Psi_0>] = \text{Im}[\boldsymbol{\mu_{0a}} \cdot \boldsymbol{m_{a0}}] \qquad \text{(Eq. 1.3)}$$

where Ψ_0, and Ψ_a are the wavefunctions for the ground state *0* and excited state *a*; $\hat{\mu}$ and $\hat{m}$ are the corresponding electric and magnetic moment operators, and $\boldsymbol{\mu_{0a}}$ and $\boldsymbol{m_{a0}}$ are the electric and magnetic transition dipole moments respectively [22–24]. Eq. 1.3 holds true for any and all quantum

systems, whether or not they are chiral, bear unpaired electrons, or are in the presence of an external magnetic field [26,115]. Its universality is attractive, but as applied to specific chiral material it is usually simplified at the expense of the magnetic term [22–26]. For instance, in the case of plasmonic NPs, the magnetic moment term is reduced to a small constant, whereas the electric moment term is considered to be most essential [22]. However, in NPs with large numbers of unpaired electrons and chiral crystal lattices, the magnetic moment term $< \Psi_a|\hat{m}|\Psi_0 >$ should have a contribution comparable to that of the electrical moment term $< \Psi_0|\hat{\mu}|\Psi_a >$, which should lead to enhanced $\boldsymbol{R_{0a}}$ and potentially to practical realizations of NP chirality in magneto-optical devices operating at low fields and ambient temperatures.

4.2 Synthesized Chiral Cobalt Oxide NPs

To investigate this hypothesis we synthesized ~5 nm Co_3O_4 NPs using the *L-* and *D-* enantiomer of cysteine (Cys) as surface ligands. These NPs serve as the primary experimental model in this study and will be referred to as *D-*, *L-,* and *DL*-Cys Co_3O_4 when corresponding Cys enantiomers or their equimolar mixture were used for NP synthesis. The choice of cobalt oxide as the inorganic core of the NPs was governed by its known magnetism, structural versatility, and the environmental robustness of cobalt-based ceramics. The chemical structure and atomic composition of the NPs was established by STEM (**Fig. 4.1D, inset**), X-ray photoelectron spectra (XPS) (Fig. 4.10), and atomic mapping imaging (Fig. 4.11). Transmission electron microscopy (TEM) indicated the frequent presence of NPs with seemingly amorphous inorganic phases (Fig. 4.10 A-C). When the crystal structure was observed, the lattice planes distances can be adequately described by the cubic spinel phase. The crystaline domains are confined to the

central part of the NPs, indicating that the seemingly amorphous shells originate from the crystal lattice distortions in the vicinity of the NP surface.

The brown transparent dispersions of these NPs reveal CD spectra of high intensity with up to eight positive and negative peaks in the UV and visible spectral range (**Fig. 4.1A,C**) corresponding to various intraparticle Co(II)→Co(III) (230, 280, 250 nm) and transition surface states (including ligands) →Co(III) (450, 550, 600 nm), as demonstrated by the sTD-DFT calculation of a model NP (Fig. 4.8 and table 4.16). The CD spectra for *D*- and *L*-Cys Co_3O_4 NPs show a nearly perfect mirror symmetry, while Co_3O_4 NPs made with equal amounts of *D*- and *L*-Cys are chiroptically silent (**Fig 4.1A**). The spectral positions of the CD peaks were nearly perfectly aligned with those in the absorption spectrum (**Fig 4.1C**). Chiroptical anisotropy *g* factors as high as 0.02 were obtained (**Fig. 4.1B**), which is ~10 times greater than other NPs of similar size, including plasmonic particles with established strong chiroptical activity [15,18]. The large *g*-factor in the visible range can also be appreciated by the naked eye, as the appearance of a distinct color when light passes through the NP-poly(acrylomide) gel and between crossed polarizers (**Fig. 4.1D,** and **SI**) [116]; the green color corresponds to the 550 nm peak in the *g*-factor spectra in **Fig. 4.1B**.

The strong chiroptical activity was also observed for Co_3O_4 NPs synthesized with and capped by *L*- and *D*-penicillamine, but the CD peaks were at different positions (Fig. 4.12) than those for Cys, especially in the visible range. Importantly, little change in the CD spectra was observed when Cys ligands were exchanged to penicillamine after formation of NPs (Fig. 4.13), indicating that chiroptical activity in the 400 ~ 700 nm range is associated with the inorganic core of the NPs. Conservation of NP chirality after the ligand exchange is consistent with

observations of chiral memory [35] and a high activation barrier for reconstruction of the Co_3O_4 lattice once NPs are formed.

Raman scattering spectra further validate the chirality of the inorganic cores in the NPs. Characteristic bands at 380, 475, 516, 613, and 680 cm^{-1} observed for *D*- and *L*-Cys Co_3O_4 NPs are associated with the Raman-active vibration modes of Co_3O_4 [117]. Raman optical activity (ROA) spectra show peaks of opposite polarity at 377, 465, 531, 719 cm^{-1} for NPs bearing opposite enantiomers of Cys (**Fig. 4.2C,D**). Of particular importance is the strong peak at 380 cm^{-1}, which corresponds to lattice phonons of Co_3O_4. The peak appears at a frequency higher than expected for Co_3O_4 with the cubic spinel crystal lattice [117] and displays a distinct antisymmetric signals of these vibrations in Co_3O_4 NPs bearing *L*- and *D*-Cys. Both facts indicate the occurrence of chirality transfer from amino acids to the crystal lattice of the inorganic core of NPs, which manifests as crystal lattice distortions [118] propagating from the surface of the NPs into the core, which can also be seen in STEM images (Fig. 4.10 A-C).

4.3 Theoretical Study of Optical Activity

A computational study of atomic scale dynamics in Co_3O_4 NPs having either surface-bound *L*- or *D*-Cys was carried out to better understand the nature of the chirality transfer and distortions in the NP core. In the silumations, relatively small NPs with Cys residues coordinated identically with the experimental NPs were used (Fig. 4.18). In the course of full geometry optimization, emblematic chiral geometries with mirror-image symmetries independently evolved for *L*- or *D*-Cys-bearing NPs. Namely, three ligands on each corner of the tetrahedral model NP formed ring-like structures with either a clockwise or counterclockwise sense of rotation with respect to the *C₃* axis (Fig. 4.2A,B). Using the Cahn-Ingold-Prelog system, these can be classified as M

(clockwise) and P (counterclockwise) enantiomers. Taking into account the hierarchical chirality in these structures that arises from superposition of the molecular chirality of the amino acids and their orientation on the surface, they can be denoted M-*D*-Cys and P-*L*-Cys Co_3O_4 NPs.

The normal mode analysis of the model NP indicated that peaks at 505, 529, 601, and 693 cm^{-1} correspond to the Raman-active breathing mode of the inorganic core and ligand-core coupling (Fig. 4.8). The experimental peaks in **Fig. 4.2C** match calculations for the M-*D*-Cys/P-*L*-Cys NPs well, with many of the bands representing the coupled vibrations of the surface atoms and ligands (**video file 1**).

During the *ab initio* molecular dynamics (AIMD) simulations, both enantiomers evolved independently, as demonstrated by the energy transient of each model (Fig. 4.9). Concomitantly, the degree of chirality increased fourfold as measured by the Hausdorff chirality measure (HCM) for both M-*D*- and P-*L*-Cys NPs (**Fig. 4.2E**), indicating that thermal fluctuations increase the degree of distortion of the NPs. It is remarkable that even though they are subjected to a range of vibrational distortions and bond reorganizations, the two model NPs follow nearly mirrored paths during the entire AIMD simulations (Fig. 4.3F).

MD simulations allow one to follow the distortions being caused by the surface ligands in the ceramic crystal lattice. The NP cores carrying *L* and *D* surface ligands present a pair of nearly mirrored structures after 2000 fs of structural relaxation (**Fig. 4.3B,C** and **Fig. 4.21**). One can analyze selected dihedral angles in these structures with respect to the value for the ideal crystallographic packing of cubic spinel Co_3O_4 (**Fig. 4.3A).** The three dihedral angles we have chosen share O atom number 35, located at the center of one of the faces of the NP model, $\phi_{35-15-8-18}$, $\phi_{35-12-11-22}$, and $\phi_{35-13-14-27}$ (**Fig. 4.3A-C and 4.21**) which have values $\phi_{35-15-8-18}=\phi_{35-12-11-}$

$_{22}=\phi_{35\text{-}13\text{-}14\text{-}27}=0$ in the undistorted cubic spinel of Co_3O_4. The binding of the surface ligands led to non-coplanarity of these atoms already in the energy minimization step, and these distortions increased during MD simulation. The mutual correlation of these angles, stemming from concerted movement of all the atoms in these nanoscale structures, can be carried out using Ramachandran-like plots. Similarly to proteins and other biomolecules, the pairwise probability of $\phi_{35\text{-}15\text{-}8\text{-}18}$, $\phi_{35\text{-}12\text{-}11\text{-}22}$, and $\phi_{35\text{-}13\text{-}14\text{-}27}$ acquiring specific values display unmistakable cross-correlation in the MD trajectories (**Fig. 4.3D-I**). Importantly, the pattern of distortion is mirrored for both *D*- and *L*-Cys NPs. These plots and MD simulations vividly show the mechanism of chirality transfer in Co_3O_4 NPs that occurs during the growth of the NPs.

Chiral distortion of the original cubic spinel lattice changes the local magnetic fields within the Co_3O_4 NPs because the overlap between the atomic orbitals of Co^{3+} and O^{2-} and the lattice symmetry are changed [119]. Instantiating this point, the spin population of two Co(III) atoms changed from a value near zero to approximately two (Tables 4.7 and 4.11) upon geometry optimization due to the distortions. The large spin (*S*) and orbital (*L*) magnetic moments contribute to the chiroptical activity of the NPs according to Eq. 1.3 via magnetic transition dipole moments with the corresponding operator taking the form

$$\widehat{m} = \frac{-e\hbar}{2mc} (\boldsymbol{L} + g\boldsymbol{S}) \qquad \qquad (Eq.4.1)$$

where *g* is the gyromagnetic ratio [120,121]. Note that *g*-factors near the upper limit can only result from large |*m*| (*m*-allowed) and small |*μ*| (*μ*-forbidden) values [23] and either parallel ($\theta = 0°$) or antiparallel ($\theta = 180°$) orientations of the transient electrical and dipole moments [27]. This is indeed the case for the bands at 500, 550, and 650 nm in (**Fig. 4.1B**) that give experimental

evidence for a strong contribution of magnetic transition dipole moments to – and paramagnetic enhancement of – the optical activity of Co_3O_4 NPs.

The significance of magnetically coupled unpaired electrons of Co atoms for the chiroptical activity of NPs was further confirmed by synthesizing mixed-metal NPs that include Cu^{2+} ions. Since the number of unpaired electrons in the Cu^{2+}-containing NPs is smaller compared to neat Co_3O_4, transition magnetic dipole moments are expected to be lower according to Eq. 4.1. Indeed, the g-values gradually decrease as the amount of Cu^{2+} increases (Fig. 4.23).

The generality of the magnetic effects on the chiroptical activity of NPs was confirmed for chiral nickel oxide NPs, which also showed strong optical activity and g-factors up to 0.01 (Fig. 4.24).

4.4 Interactions with Magnetic Fields

As one could expect from Eqs. 1.3,and 4.1, the rotatory optical activity of D- and L-Cys NPs can be altered by external magnetic fields, which has important technological implications for information technologies and photonics. To test these magnetic field effects, the Co_3O_4 NPs were encapsulated in a transparent polyacrylamide gel (**Fig. 4.4C**) to avoid variation of optical properties due to translational movement of the NPs. The NP gels showed the same optical and chiroptical bands at same wavelengths in the zero-field as dispersions (**Fig. 4.4** and 4.30-32). The magnetic field effect is fundamentally different than the magnetic circular dichroism (MCD) found for Au, Ag, or Fe_3O_4 NPs [122–125] due to (a) the dramatic increase in UV transparency for circularly polarized light, and (b) its disappearance for racemic DL-Cys NPs (Fig. 4.28B). Importantly, the field on/field off ratios of the 280 nm NP absorption peaks of left- and right-circularly polarized beams and their sum (**Fig. 4.4A,B**) markedly exceeds those ratios, even for

the giant Faraday rotation found in nanoscale plasmonic systems [105,106,126] and giant Zeeman splitting [127,128]. Note also that the chiroptical effects of this magnitude are observed for *D*- and *L*-Cys NPs at room temperature, as opposed to liquid helium temperatures, which are often used for experimental observations of the chiroptical effects in magnetic nanomaterials [9,10] and the magnetooptical effects mentioned above.

While containing components of light-matter interactions from 'natural' CD, the Faraday effect and MCD [115,129], the magnetic-field-induced transparency for circularly polarized light originates from the decrease of the absorption cross-section of the NPs when a magnetic field is applied to non-cubic crystal lattices [130]. The chiral distortions caused by the *L*- and *D*-Cys attachment to the surface of the Co_3O_4 NPs make the dielectric permitivity and magnetic susceptibility tensors strongly anisotropic. The external magnetic field polarizes the paramagnetic NPs so that the spin and orbital magnetic moments become preferentially oriented in the direction of the field. The effect will be small for NPs with crystal lattices of high symmetry (*e.g.* cubic) and their experimental observation would require low temperatures to mitigate thermal broadening of the chiroptical peaks due to the lower anisotropy of the dielectric permittivity and magnetic susceptibility tensors. Indeed, the transparency increase is minimal in *DL*-Cys NPs, wherein chiral distortions are partially compensated (**Fig. 4.1A**, and 4.29). The effect is also minimal for optical transitions involving surface states, as the near-spherical symmetry of NPs averages the effect of external polarization on all the terms in Eq. 1.3. Consequently, the visible part of the CD spectra (>450 nm) of both *D*- and *L*-Cys NPs experience little influence of the magnetic field, despite a high *g*-factor (**Fig. 4.1B)**. However, the spectral region associated with Co(II)→Co(III) electronic transitions displays very strong effects because the external magnetic field forces both donor and acceptor states to acquire

simultaneous alignment that is not averaged in the individual NPs or their ensembles. A simplified reasoning for the reduced absorption cross-section of the circularly polarized light is the alignment of the transient magnetic moment for the Co(II)→Co(III) transition along the external magnetic field, which makes it orthogonal to the magnetic moment of incident photons and leads to a markedly reduced amplitude of the $< \Psi_a | \hat{m} | \Psi_0 >$ term.

The strong absorbance drop allows optical modulation using a magnetic field, which was observed with excellent fidelity over 60 cycles (**Fig. 4.4E**). Note that no agglomeration of the NPs was observed. The cyclic switching of the gel transparency in the deep UV absorption band of the NPs can also be converted into the modulation of photons in the visible range using fluorescent targets (**Fig. 4.4 D, F,** and **SI Note 5**).

4.5 Conclusion

In conclusion, structural design aimed at maximizing the contribution of the transient magnetic moment to the circular dichroism of chiral NPs was undertaken. This design and synthesis resulted in the discovery of large increases of their *g*-factors in the visible wavelength range, as well as intense magnetic-field-induced light modulation in the UV range. In addition to Co_3O_4, a large family of ceramic NPs with structural chirality and tunable optical/magnetic properties can be prepared using the synthetic approach described herein, as exemplified by the multiferroic oxides. Besides their technological relevance to magneto- and opto-electronic devices, the chiral ceramic NPs prepared in this work offer a uniquely versatile experimental system for the fundamental study of second-order magneto-chiral phenomena and magneto-dielectric effects.
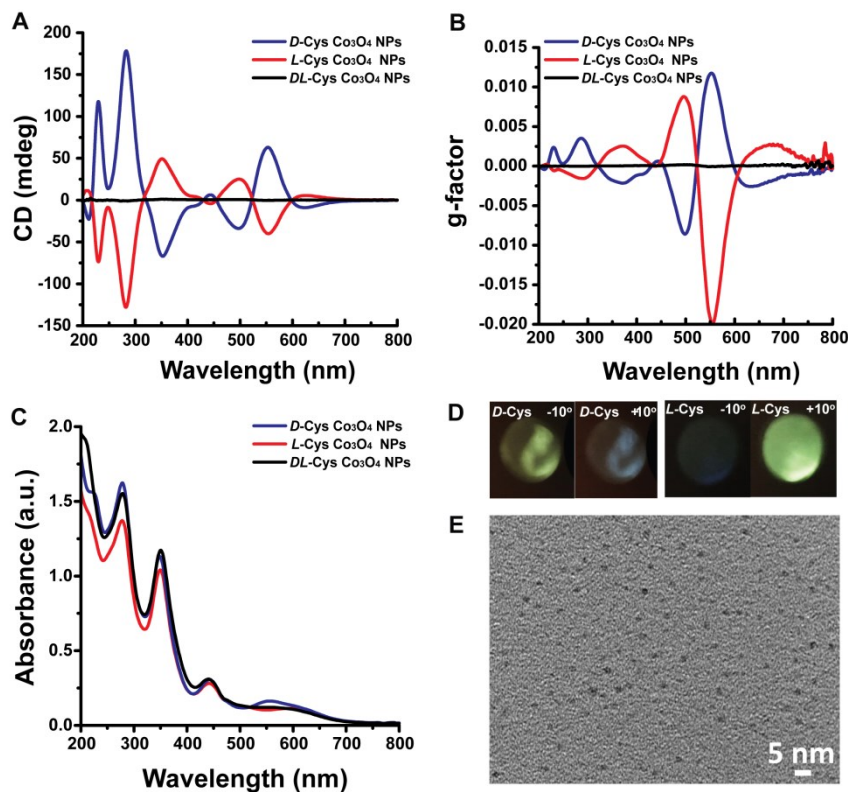
Figure 4.1. Synthesized chiral Co₃O₄ NPs. A, B and **C,** CD (A), g-factor, defined as the ratio between the molar circular dichroism $\Delta\varepsilon$ and the molar extinction coefficient ε (g = $\Delta\varepsilon/\varepsilon$), graphs (B), and UV-vis absorption spectra (C) of Co₃O₄ NPs stabilized by *D*-Cys, *L*-Cys, and *DL*-Cys. **D**, Photographs of NPs transmitted light with the rotation of the linear analyzer counter-clockwise (−10°), and clockwise (+10°) **E,** TEM image of *L*-Cys capped Co₃O₄ NPs. The *d* spacings of 0.285 nm and 0.202 nm observed correspond to the Co₃O₄ (220) and (400) crystal planes, respectively.
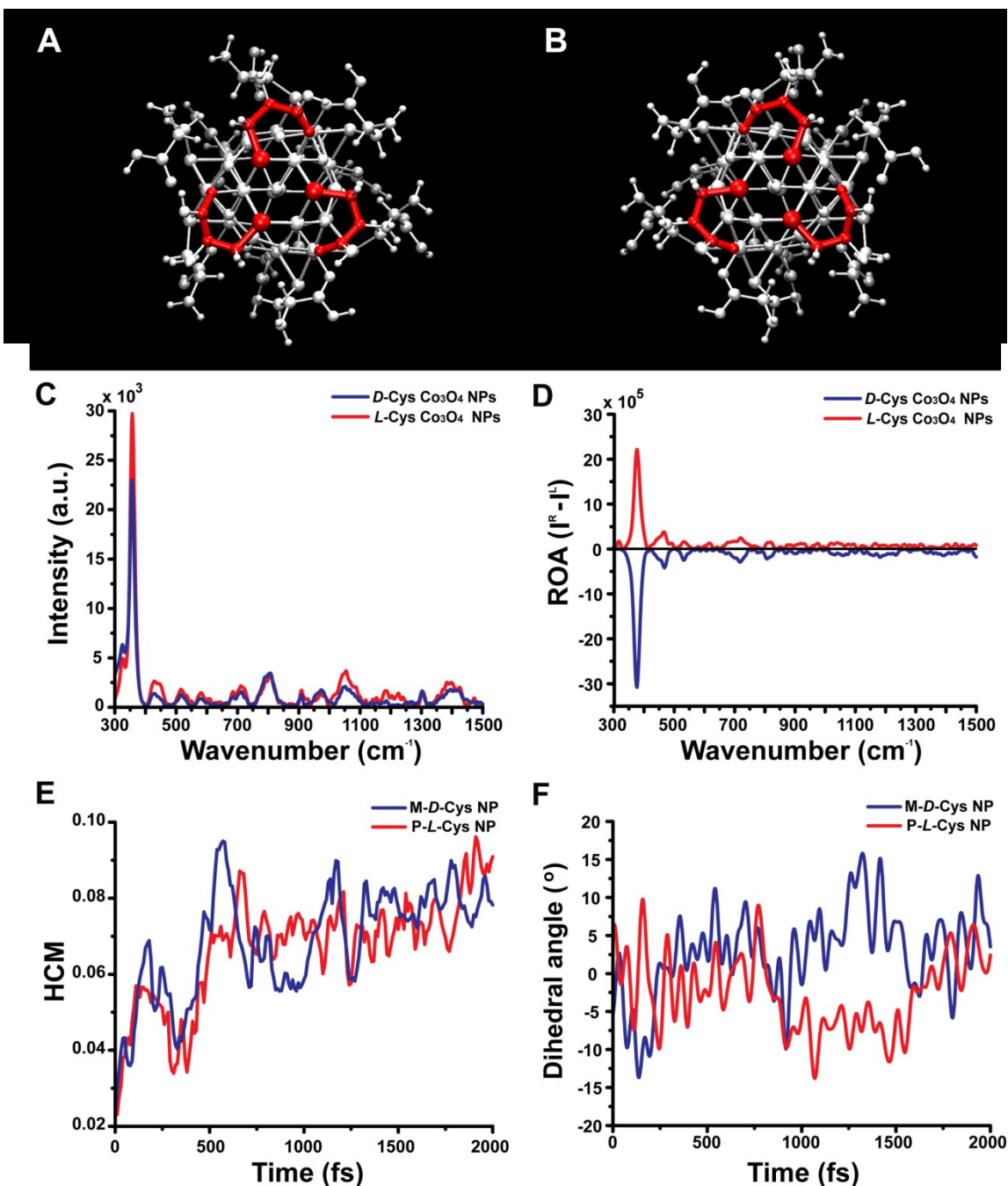
Figure 4.2. Rotations of crystalline structures. A and **B,** *D*-Cys (A) and *L*-Cys (B) Co_3O_4 NPs. Sulfur atoms are the larger red spheres forming one corner of the tetrahedra and remaining atoms depicted in red are the C-C-C-O atoms of the Cys ligands. **C** and **D,** Raman (C) and ROA (D) spectra with excitation of 532 nm of *D*-Cys and *L*-Cys Co_3O_4 NPs. These spectra are courtesy of *BioTools, Inc*. **E,** Hausdorff chirality measure for the NP cores. **F,** Dihedral angles between atoms 18-7-9-22 (O-Co(III)-Co(III)-O) of *L*-Cys and *D*-Cys Co_3O_4 NPs.
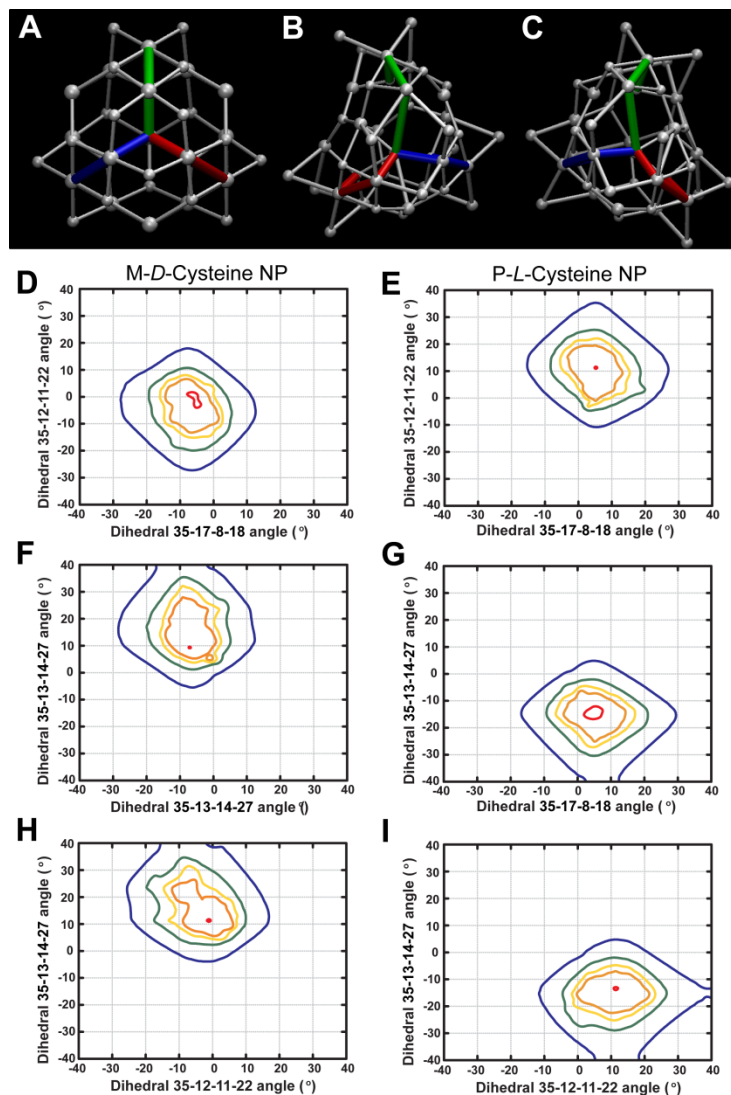
Figure 4.3. Atomic chiral arrangements. Graphical representation of the dihedral angles formed by four atoms $\phi_{35\text{-}12\text{-}11\text{-}22}$ (red), $\phi_{35\text{-}17\text{-}8\text{-}18}$ (blue), and $\phi_{35\text{-}13\text{-}14\text{-}27}$ (green). A detailed description of the atomic types and numbering of each dihedral angle may be found in Fig. 4.21. **A,** NPs with ideal crystallographic structure. **B,** NPs with M-*D*-Cys after 2000 fs of MD simulation. **C,** NPs with P-*L*-Cys after 2000 fs of MD simulation. The direction from the S atom to the carbonyl atom in the Cys molecules is taken as the basis for the geometry classification according to the Can-Ingold-Prelog rules. Ligands have been omitted for the sake of clarity. **D to I**, Two-dimensional probability maps for the relative orientation of adjoining octahedra pairs sharing the O atom number 35. Average probabilities were computed along the 2000 fs MD simulation for the NP functionalized with either M-*D*-Cys (left) or *L*-Cys (right). The isovalues depicted in the plots are probabilities of 0.0002 (blue), 0.0003 (green), 0.0004 (yellow), 0.0005 (orange) and 0.001 (red).
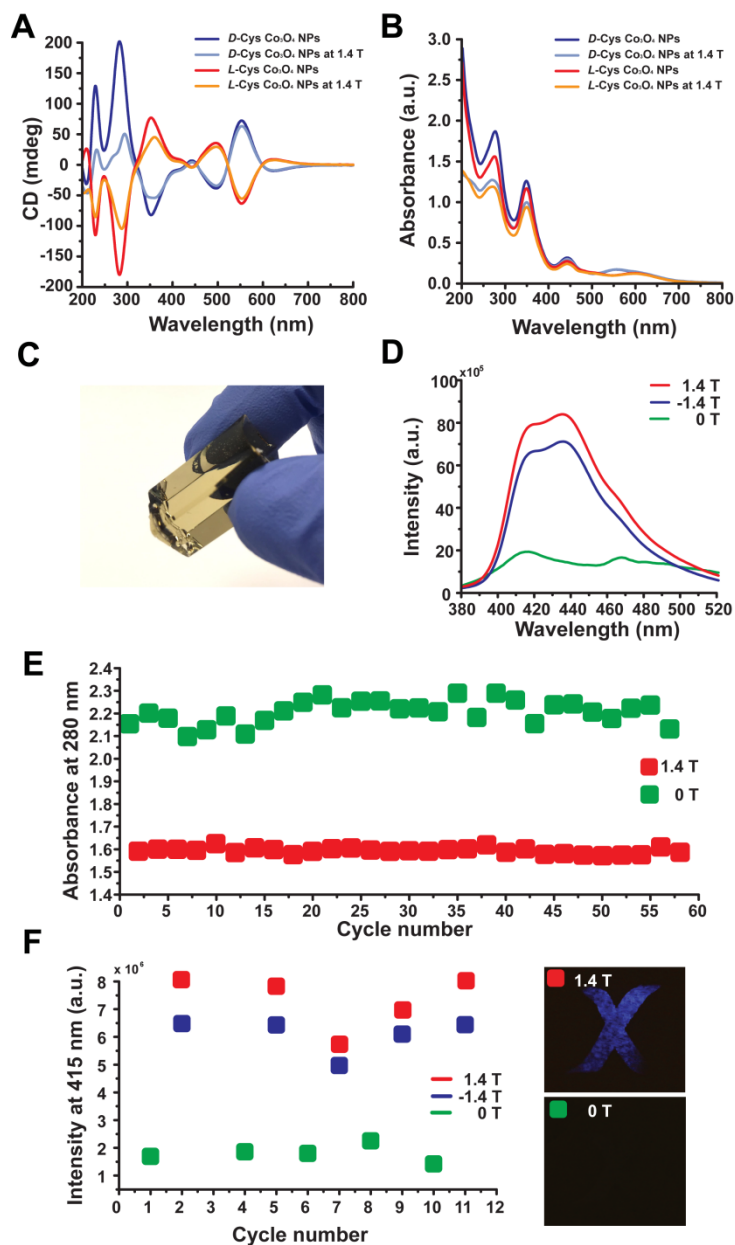
Figure 4.4. Optical modulation. A and B, CD and MCD (A) and corresponding absorbance spectra (B) of *L*-Cys and *D*-Cys Co₃O₄ NPs. **C,** Photograph of the optically transparent gel made from *L*-Cys Co₃O₄ NPs. **D,** Emission intensities of fluorescence paper plus the NP gel in front, with a magnetic field applied to the NP gel (red and blue), and without magnetic field (green). (Excitation: λ_{ex} = 280 nm.). **E,** Cycling performance of the absorbance of the NP-containing gels at 280 nm with and without magnetic fields. **F,** Cycling profile of emission intensity at 415 nm with and without magnetic field and corresponding photographic images of blue emitted light from the fluorescence paper.

4.6 Supplementary Information

4.6.1 Experimental Information

Synthesis and analysis of cobalt oxide NPs

We developed a simple synthesis procedure using cobalt (II) chloride and *L*- or *D*-Cys as metal precursors and chiral ligands. All procedures were conducted in aqueous conditions. In 15 mL of E-pure water, add 2.5 mL of 100 mM $NaBH_4$, 2 mL of 100 mM *L*- or *D*-Cys, 2 mL of 100 mM sodium citrate, and 1 mL of 200 mM cobalt (II) chloride. All chemicals were purchased from Sigma-Aldrich. After two hours of magnetic stirring at room temperature, brownish transparent nanoparticle dispersions are obtained. The synthesized nanoparticles were analyzed after sufficient purifications by rinsing NPs with E-pure water. The precipitation was done by dialysis using a 1 kDa MWCO membrane, or precipitation with addition of a seven-times larger volume of isopropanol followed by centrifugation for 20 min at 10,000 rpm.

Optical rotation

Linearly-polarized light (LPL) can be considered as a superposition of LCP and RCP. Due to the speed differences of LCP and RCP during the travel through chiral materials, the polarized plane of LPL rotates into a certain direction depending on the handedness of the sample. Since the degree of rotation varies related to the wavelength, it is possible to observe a series of different colors by rotating the second polarizer.
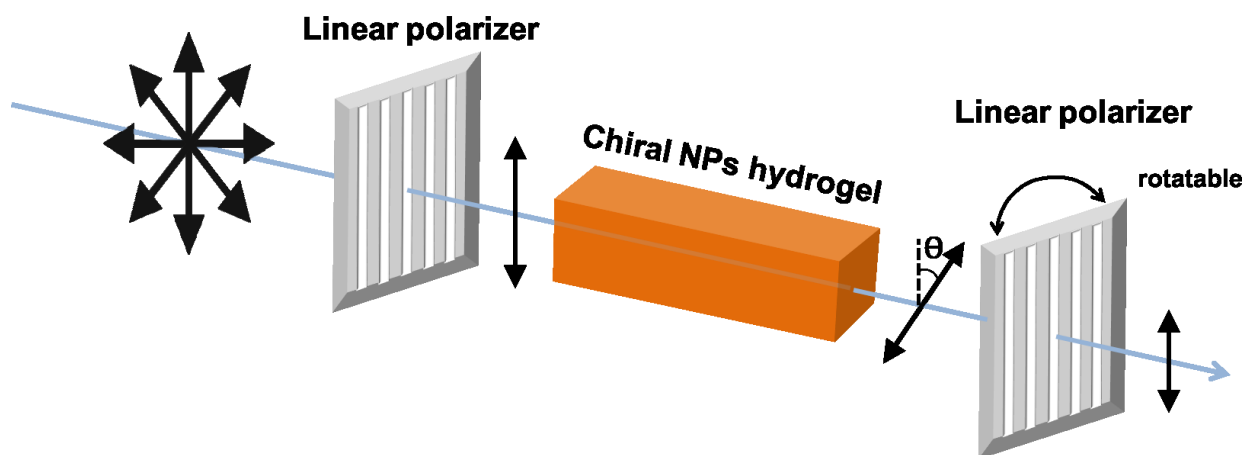
Scheme 4.1. Optical rotation experimental set up.

Ligand exchange

In the dispersion of *L*-Cys-capped NPs we dissolved an excess amount of *D*-Cys or *D*-penicillamine, and to the *D*-Cys-capped NP dispersion we added *L*-Cys or *L*-penicillamine. The samples were incubated for 72 hours with 15 hours of sonication (five hours per day, for three following days). CD spectra were measured after purification via dialysis.

To confirm the ligand replacement, we decomposed NPs by adding HCl to the thoroughly rinsed NPs and then incubating them at 85 $^{\circ}$C. After four hours, the color turned to transparent pale yellow, indicating decomposition of the NPs, and showed CD signals of the replaced ligand with significantly reduced intensity of NPs (Fig 4.14). These results indicate that the optical activity originated from the NPs' chiral core structure, which twisted into a certain direction depending on the chiral ligands used during their synthesis.

It is noteworthy that the strong conservation of NP chirality, even after full ligand exchange, is consistent with the existence of activation barriers much higher than the thermal energy. This chiral memory arising from the kinetic stability preventing both racemization and chirality inversion should be important for any potential application, since ligands might be exchanged at will to add new functionalities to the NPs while retaining the tailored chirality imprinted during the synthesis stage.

4.6.2 Computational Simulations
Simulation of atomic structures, chiral indexes and chiroptical properties

All calculations were performed within the density functional theory (DFT) framework using Becke's three-parameter exchange functional and the Lee-Yang-Parr correlation functional (the so-called B3LYP hybrid functional) [131], using the 6-31G basis set [132–134]. All calculations have been performed using NWChem version 6.6 [135], running in parallel on the Brazilian Supercomputer SDumont with up 1200 cores per job. Besides specifying the technical details of the calculation, we deem it necessary to discuss at length all the reasoning behind the buildup of the model systems, so as to provide to the readership a perspective of the choices we had to make, many of which were necessarily arbitrary.

The simulation of Co_3O_4 spinels poses a series of challenges from the computational standpoint. Besides the obvious difficulty of treating systems with a large number of electronic degrees of freedom, the magnetic character of the Co_3O_4 nanoparticles requires the assessment of spin states with large numbers of unpaired electrons. Since the number of unpaired electrons depends on the actual size of the NP, we shall begin the discussion by the description of the size and shape of the base NP core.

Choosing one Co(II) atom to be at the center of the NP and defining a spherical cutoff of 0.5 nm around this reference site yielded a tetrahedral NP. This is the smallest and yet still meaningful structure we might consider, with the stoichiometry $Co(II)_5Co(III)_{12}O_{28}{}^{10-}$. The most important structural features of this model NP may be summarized as follows:

- Although minimalist, the model NP contains one fully coordinated tetrahedral Co(II) atom at the center, which is representative of bulk Co(II) atoms of the actual physical system;

- There are four Co(II) atoms (one at each face of the tetrahedron) which are triply coordinated to O atoms and are representative of surface Co(II) atoms;

- Twelve octahedral Co(III) atoms were added, two at each edge of the NP.

The lowest allowed spin state for this NP is the doublet, in which one Co(II) atom is in a low-spin state with only one unpaired electron, while all other atoms have a closed-shell structure. This is not expected for the Co_3O_4 spinel, however, which should have all Co(II) atoms in high-spin $t_{2g}{}^5e_g{}^2$ state (with three unpaired electrons per atom) and the Co(III) atoms with three possible states, ranging from the low-spin $t_{2g}{}^6e_g{}^0$ state (all electrons paired), to the intermediate-spin $t_{2g}{}^5e_g{}^1$ state (with two unpaired electrons) and maybe even a high-spin $t_{2g}{}^4e_g{}^2$ state (with four unpaired electrons).[136]

Thus, in principle eight different spin multiplicities should be considered (2, 4, 6, 8, 10, 12, 14 and 16) only to account for the spin states of the five Co(II) atoms, assuming that all Co(III) atoms are in their low-spin state. The geometry of the NP should be optimized for each spin state, and the lowest-lying state (*i.e.*, the spin multiplicity yielding the lowest energy after geometry

optimization) should be regarded as the ground state for the model system, at least within the range of choices being made for sake of simplicity.

Even with this *ad hoc* choice to restrict ourselves to study the total electronic spin in the range from S=1/2 to S=7 1/2, it soon became clear that this preliminary investigation could not be undertaken for NPs with ligands. Firstly because the number of degrees of freedom was too large to be efficiently tackled, and secondly because the ligands are flexible and would easily be trapped in local energy minima during the geometry optimization. We switched to the bare NPs with crystallographic geometry and capped with 12 H atoms, which was small enough to be tackled by the DFT geometry optimization. As a general trend, the total energy decreased as the spin multiplicity increased, but with a slightly erratic path with alternating local maxima and local minima.

We tried to improve the reliability of spin scan by performing cycles of geometry optimization: (1) beginning with the same structure, the NP was optimized independently at each spin multiplicity; (2) the lowest energy among these spin multiplicities was obtained for 2S+1=16, so this structure was used as the input for the optimization with 2S+1=14, and this was the input for the optimization with 2S+1=12 and so on until the spin multiplicity was 2S+1=2; (3) the optimization then proceeded back from 2S+1=2 to 2S+1=16. We expected that this procedure might become self-consistent, in the sense that after a few cycles the energy for each multiplicity would be nearly the same regardless of the sampling direction, but we still observed a considerable hysteresis, arising mostly from the subtle but noticeable differences in the relative orientation of the H atoms with respect to the NP surface. Since we cannot at this point of the investigation split the energy into contributions from either the spin multiplicities or the atomic

arrangements, and considering that unpaired electrons should arise preferably from the high-spin state Co(II) atoms, we decided that all subsequent models would have 15 unpaired electrons (spin multiplicity 2S+1=16).

Although subject to some intrinsic uncertainty, the optimized NP for spin multiplicity 16 corresponded to a stationary point of the potential energy surface, as demonstrated by the vibrational normal modes analysis, which yielded only real frequencies (Fig. 4.5). It is noteworthy that normal modes arising exclusively from the NP core fall below 700 cm^{-1}, defining a frequency range for the coupling of vibrational modes between the NP core and the ligands.
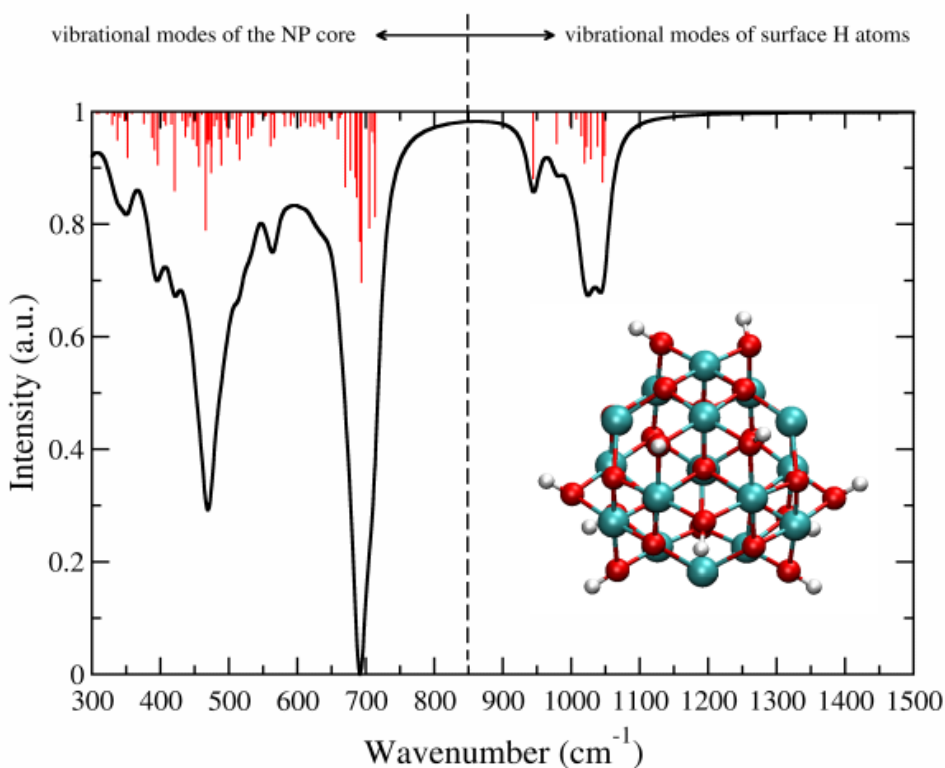
Figure 4.5. Vibrational normal modes for the bare NPs capped with H atoms. Vertical red lines stand for the calculated transition intensities whereas the black line is the convoluted Lorentzian line shape (half-width of 12 cm^{-1}). The inset structure is the optimized geometry for this NP.

91

The capped NP is far more complex than the bare case, both because the number of degrees of freedom is larger and because the ligands are intrinsically flexible. On the one hand, flexibility poses a serious challenge to gradient-based optimization strategies, due to the incredibly large number of close-lying conformers. On the other, coordination chemistry studies on Co(II)/Co(III) complexes formed with Cys and other ligands with multiple coordination sites point out to the larger stability of doubly and triply coordinated ligands with respect to their singly coordinated counterparts [137]. Thus it is not advisable to draw ligands randomly and let the structure relax during geometry optimization. Instead, it is necessary to place the ligands with starting orientations that are suitable to form at least doubly coordinated structures (triply coordinated ligands could not be drawn – although they are preferred for single Co(II)/Co(III) atoms in solution, there seems to be a steric hindrance in the case of crystalline NPs).

Taking the NP depicted in Figure 4.5, each H atom was replaced by a Cys molecule, two on each edge and three on each face (24 ligands altogether). Both *D*- and *L*-Cys had to be considered here as well as their relative orientation with respect to each other. As regards the relative orientation of each ligand, two possibilities had to be considered for the faces: either clockwise or counterclockwise with respect to the C_3 rotation axis passing through each face/corner. This sense of rotation refers to the relative orientation of a vector pointing from the S atom to the carbonyl O atom of each ligand, corresponding to either the M or the P chirality in the Cahn-Ingold-Prelog classification, respectively (Fig. 4.6 and Fig. 4.2 A-B of main text).
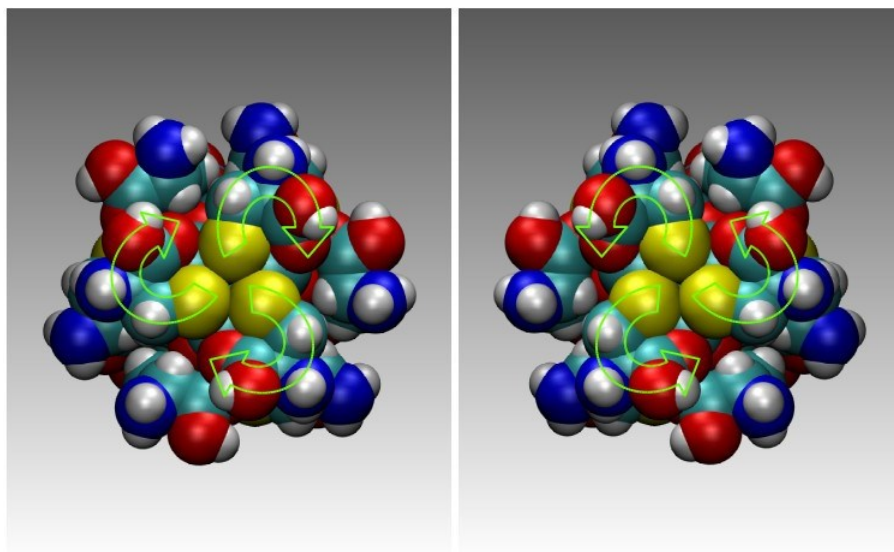
Figure 4.6. Starting structures for the NP with *D*-Cys ligands. The curved arrows indicate the sense of rotation of the ligands for the M chirality (left) and the P chirality (right).

It should be clearly stated that the sense of rotation was assigned as either M or P for the starting configurations, but it only makes sense to keep these classifications for the relaxed structures if and only if the ligands should become doubly our triply coordinated to the NP, since singly coordinated ligands would eventually racemize the sense of rotation due to thermal agitation.

It should also be noted that the superposition of two types of chirality yields pairs of diastereomer-like structures: the NP with M-*D*-Cys is the mirror image of the NP with P-*L*-Cys, whereas the NP with P-*D*-Cys is the mirror image of the NP with M-*L*-Cys. So only the M-*D* and the M-*L* combinations were actually drawn and have been optimized.

The NP with M-*L*-Cys yielded all ligands singly coordinated after full geometry optimization (Fig. 4.7). All NH_2 and COOH groups point outward and the COOH groups formed H-bonded bunches of ligands (each bunch with 3 ligands). Although some degree of chirality was imparted by the ligands, as demonstrated by the Hausdorff chirality measure (HCM) of the

core, which increased from zero to 0.0112 as the geometry optimization proceeded, we considered that the isomer M-L as well as its mirror image P-D should not be considered as proper candidates for the remainder of the investigation.
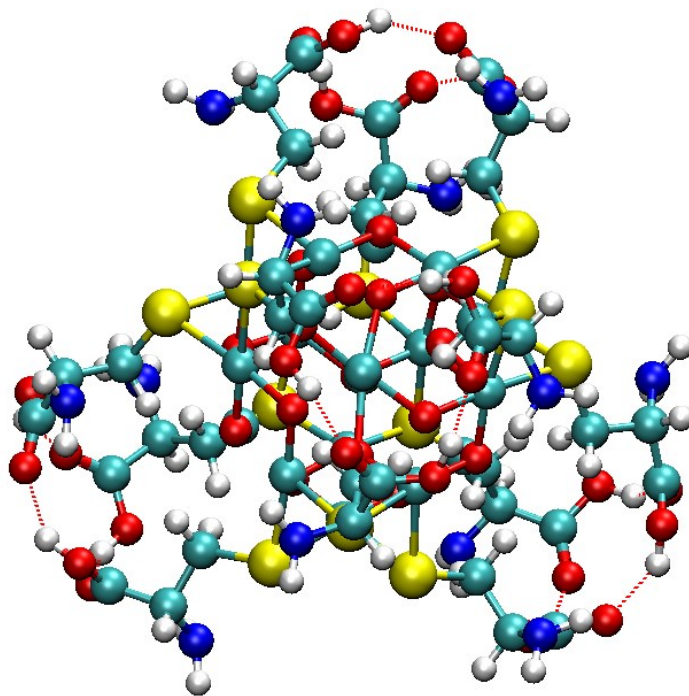
Figure 4.7. Optimized structure of the NP with M-*L*-Cys ligands. H bonds between COOH groups of the ligands are depicted as dashed red lines.

As regards the NP with M-*D*-Cys ligands, the geometry optimization led to the double coordination of all but one ligand molecule, which remained singly coordinated and interacting with a neighboring Cys. This geometry optimization was a computationally overwhelming task, which consumed *ca.* 120 hours of a premium allocation of computer time running 1200 dedicated cores. The frequency calculation was also a daunting task, using the same 1200-core allocation for over 250 hours of dedicated calculation.

The normal mode analysis yielded nine imaginary frequencies with wavenumbers below 100 cm^{-1}. From a strictly formal point of view, we acknowledge that further optimization should be done until all vibrational modes were fully optimized, but the amount of computing time was already enormous. These few modes corresponded to either poorly located optimal geometries of a few groups or poorly described forces on those groups, or a combination of both. Whichever is the case, the energy range of these modes lies well below the region of interest studied by our ROA measurements, so it is safe to disregard these modes for the time being.

The calculated IR spectrum for the functionalized NP (Fig. 4.8) was far more complex than that we obtained for the bare NP (Fig. 4.5), as might be expected. Our goal here is to demonstrate that low-wavenumber normal modes of the NP core may and indeed do couple with modes in the same wavenumber range arising from the organic layer around the NP. As usual, several normal modes with only slightly different wavenumbers may be grouped together and classified into classes of vibrational modes with the same physics, so we now describe some remarkable modes we have identified for this system (wavenumbers refer to the lowest frequency at which these modes became discernible):

- 106 cm^{-1}: Cys molecules pivoting in a rigid-body librational movement around their chiral atom, with a subtle breathing movement of the NP core as a whole;

- 126 cm^{-1}: collective breathing mode of the Co(II) atoms coupled to the rigid librational movement of the Cys molecules;

- 402 cm^{-1}: collective breathing mode of both Co(II) and Co(III) atoms mediated by the intervening O atoms between them, coupled to low-amplitude rocking modes of the NH$_2$

groups. The movement of the O atoms cause the equatorial planes of two adjoining octahedra to vibrate up and down with respect to their equilibrium positions;

- 505 cm^{-1}: out-of-phase, in-plane deformation of the equatorial planes of two adjoining octahedra strongly coupled to the rocking mode of a nearby NH_2 group. Closer Co(III) atoms are slightly coupled, whereas Co(II) atoms hardly move;

- 529 cm^{-1}: angular deformation of the axial Co(III)-O bond for the carbonyl O atom of a doubly coordinated Cys molecule. The rocking of nearby NH_2 groups are strongly coupled to this deformation;

- 601 cm^{-1}: C-O-H bending of the Cys carboxylic group, with only minor coupling to the NP modes;

- 693 cm^{-1}: angular deformations of O atoms inside the NP coupled to OH angular deformation and other vibrations along the Cys molecules;

- 707 cm^{-1}: Cys S-C bond stretching coupled to the Cys OH bending;

- 797 cm^{-1}: Cys CH_2 rocking;

- 968 cm^{-1}: angular deformation between two H-bonded Cys molecules (no coupling with the NP);

- 983 cm^{-1}: Cys C-C bond stretching.
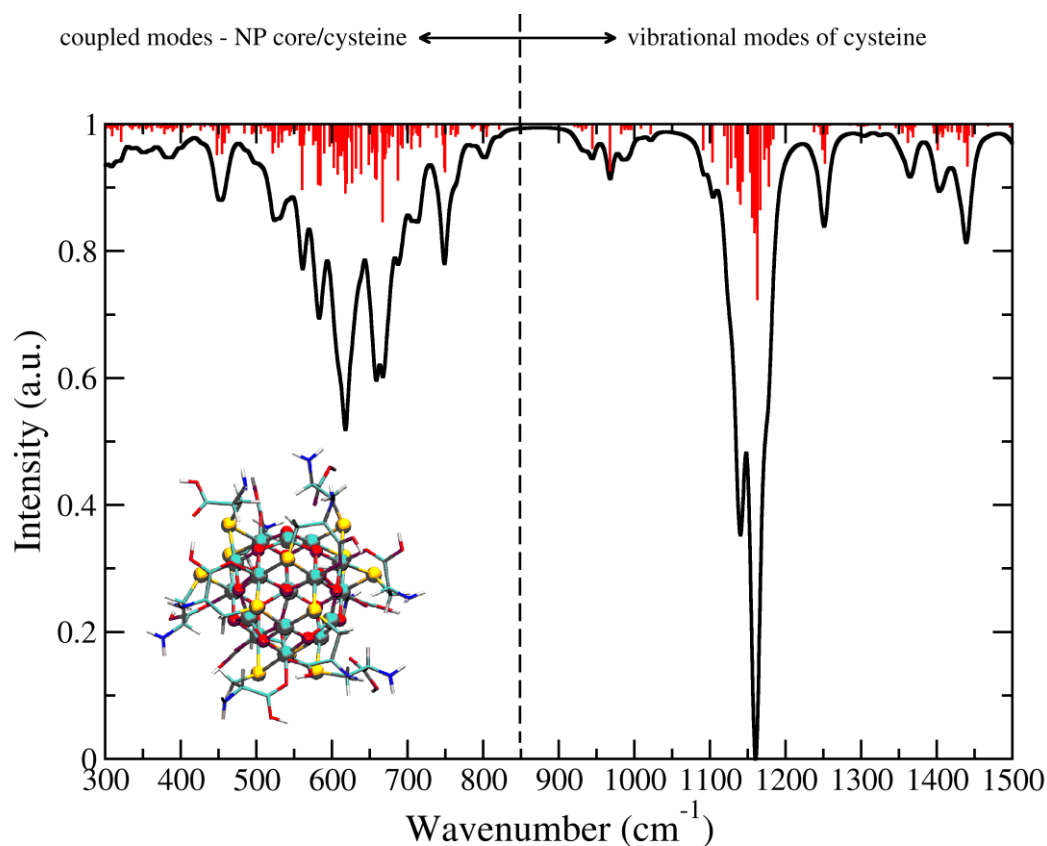
Figure 4.8. Vibrational normal modes of the NP functionalized with *M*-*D*-Cys (optimized structure for the spin multiplicity 2s+1=16 shown in the lower left corner of the plot). The red vertical lines are the calculated transitions whereas the black line stands for the convoluted spectra calculated with a Lorentzian broadening (half-width of 6 cm^{-1}).

The breathing modes of the NP are observed at very low wavenumbers and their relative importance decreases steadily until the spectrum becomes totally dominated by the normal modes arising exclusively from the ligands, just above 700 cm^{-1}. It should be emphasized that the NPs with P-*L*-Cys have exactly the he same vibrational modes. The discrimination between these mirror image isomers can only be done by means of chiroptical vibrational analysis – either vibrational circular dichroism (VCD) or Raman optical activity (ROA).

Although geometry optimizations should be regarded as being successfully accomplished, we decided to take one further step in the direction of obtaining a fully relaxed structure. Namely,

we decided to perform *ab initio* molecular dynamics (AIMD) for the optimized NP with M-*D*-Cys ligands, using the same level of theory of the geometry optimization and frequency calculations (B3LYP/6-31G). NWChem performs adiabatic AIMD using the Verlet integrator. The following options have been set for the AIMD simulations:

- Temperature controlled using the velocity rescale method;

- Target temperature of 300 K;

- Linear and angular momenta removed every five time steps;

- Integration time step of 1 fs;

- Number of integration steps: 2000.

Since numerical integration of the atomic trajectories is sensitive to the starting configuration, we considered this might be the best opportunity to assess whether chirality mirroring actually takes place beyond the static geometries provided by the geometry optimization techniques. We took the optimized geometry for the NP with M-*D*-Cys and mirrored all atomic coordinates, yielding the NP with P-*L*-Cys, but truncated the x, y and z coordinates to six decimal places (instead of the 12 decimal places used by the simulation software). Although tiny, these slightly different initial coordinates were different enough to ensure that each system should evolve by an independent path along the phase space, as demonstrated by the evolution of the total energy along the simulations (Fig. 4.9).

Each one of these two AIMD simulations required 250 hours of the premium supercomputer allocation running 1200 dedicated cores, so altogether the simulations presented here (geometry optimization, frequency calculation and AIMD simulations) used 1200 computational cores for *ca.* 35 days. Although only large-scale facilities can provide such impressive amounts of

computer power, we consider this is the direction we should proceed in future investigations, so

as to avoid or at least minimize the well-known drawbacks of geometry optimization approaches.
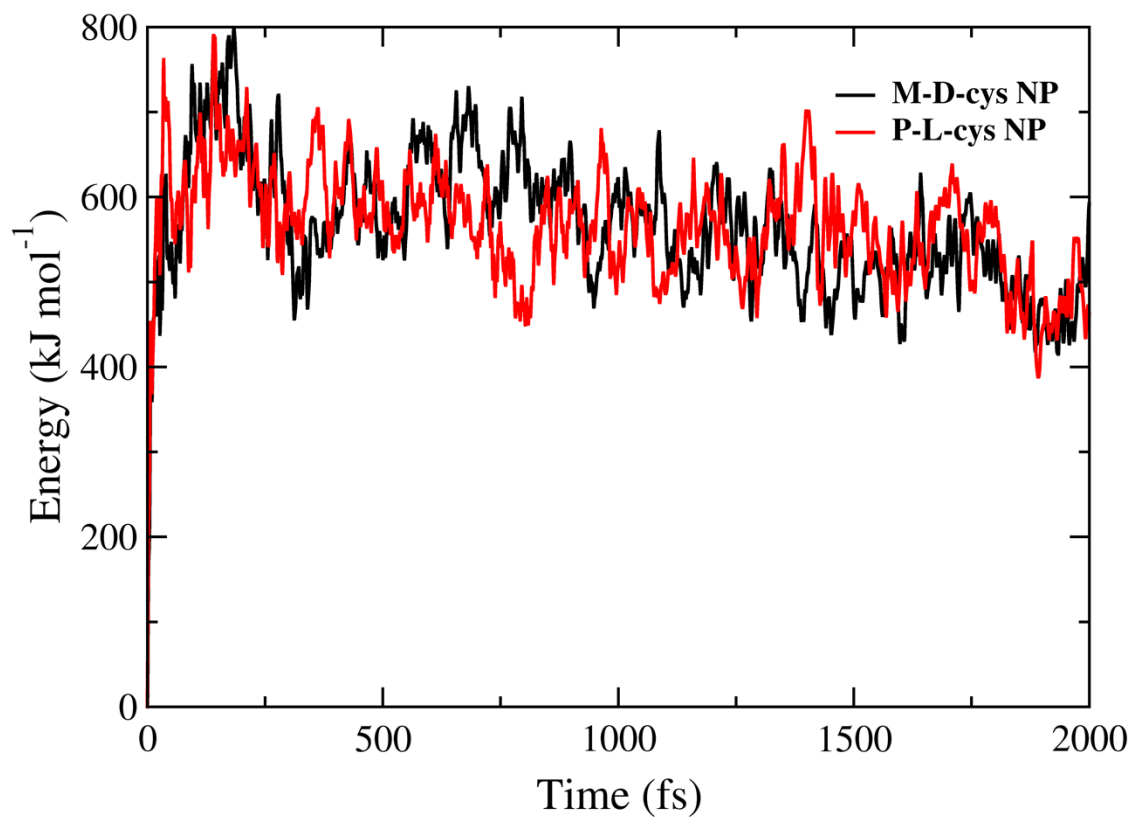
Figure 4.9. B3LYP/6-31G energy during AIMD simulation.

4.6.3 Additional Figures and Comments
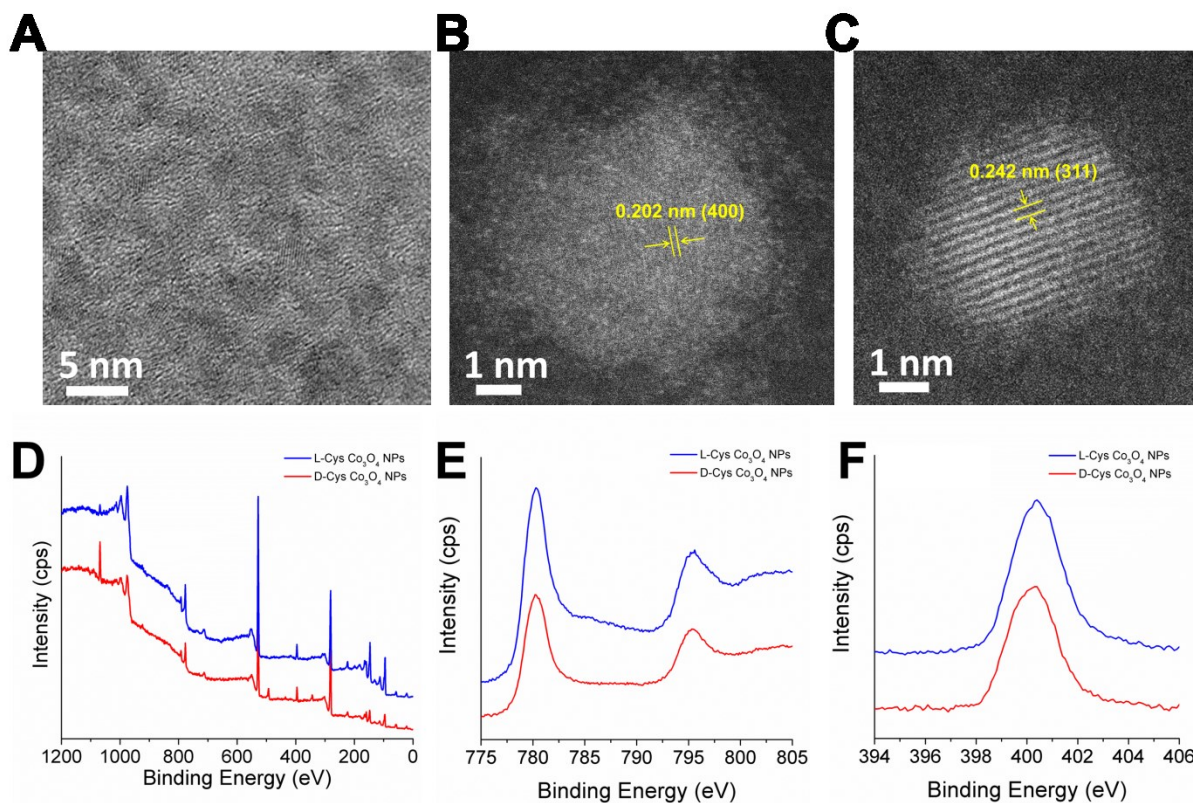
Figure 4.10. HR TEM (A) and STEM (B and C) images of *L*-Cys Co_3O_4 NPs. Survey (D), Co 2p region (E), and N 1s region (F) XPS spectra of *L*-Cys and *D*-Cys Co_3O_4 NPs.

Elemental analysis carried out using X-ray photoelectron spectra (XPS) (Fig. 4.10), atomic mapping image (Fig. 4.11) and the elemental atomic composition of 37% Co, 52% O confirmed the oxidation state of the NPs is Co_3O_4 spinel in which Co^{2+} and Co^{3+} cations are situated at tetrahedral and octahedral sites, respectively.
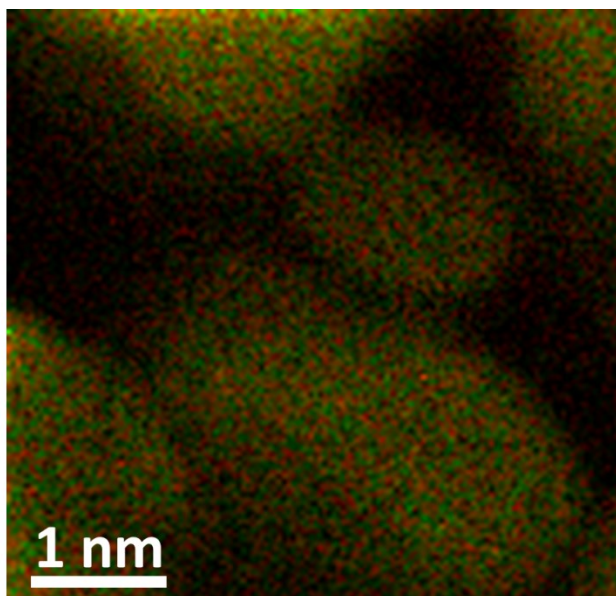
Figure 4.11. Atomic composition image. The green color indicates cobalt and red indicates oxygen.
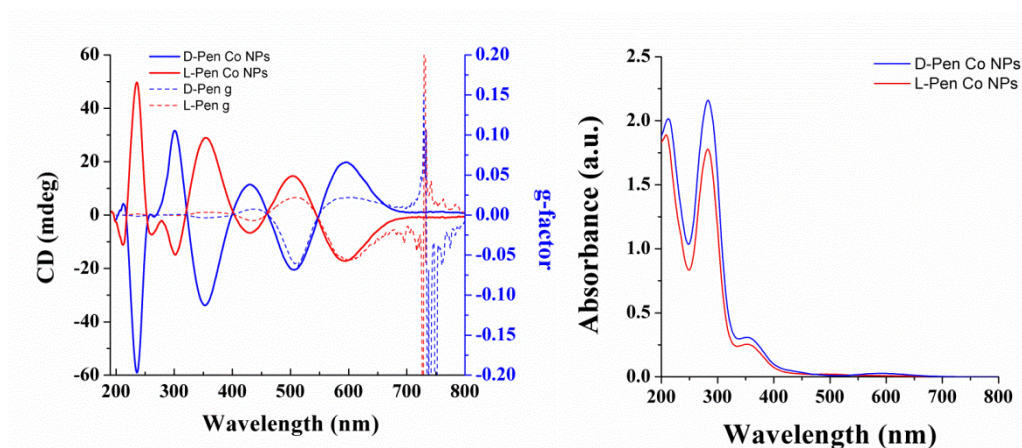
Figure 4.12. CD and g-factor (A) and UV-vis absorption spectra (B) of Co_3O_4 NPs stabilized by *D*- and *L*-penicillamine.
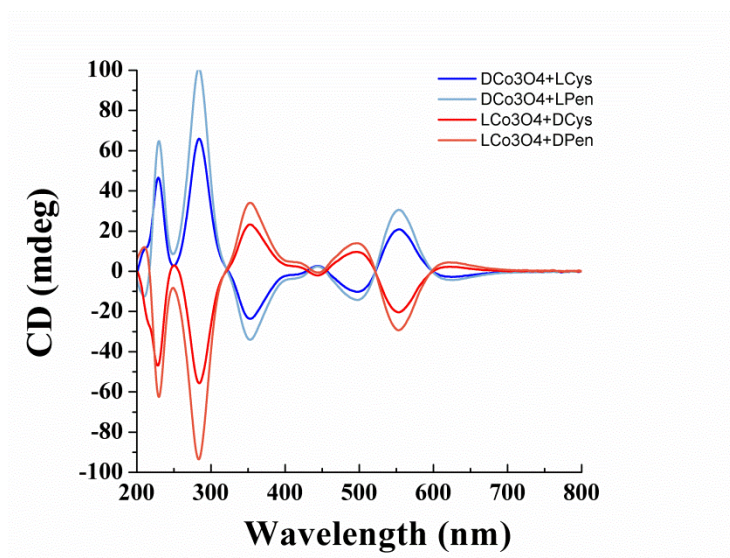
Figure 4.13. CD spectra of ligand-exchanged NPs when NPs initially synthesized with *L*- or *D*-Cys were exposed to *L*- or *D*-penicillamine.
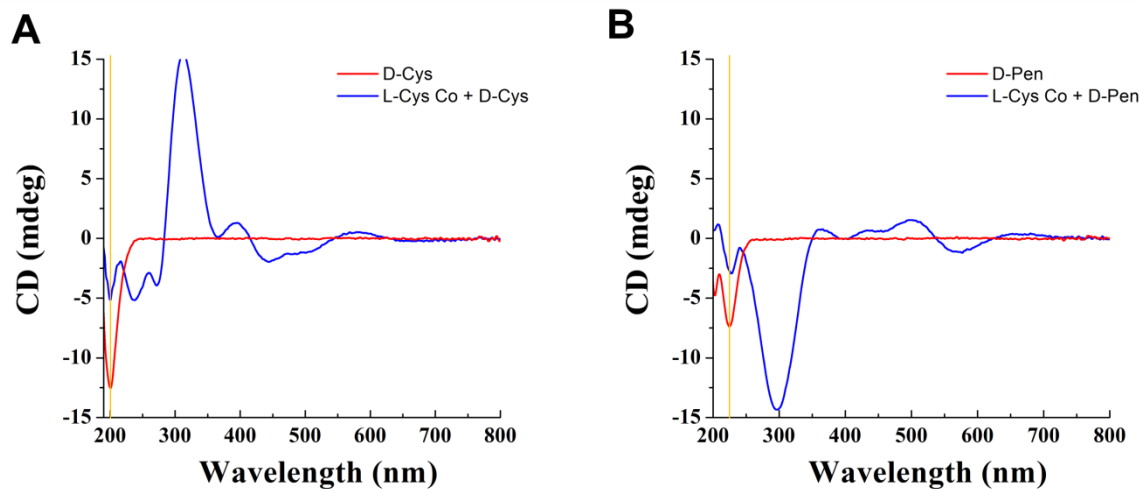
Figure 4.14. CD after decomposition of NPs that were ligand-exchanged from *L*-Cys to *D*-Cys (A) and to *D*-penicillamine (B).
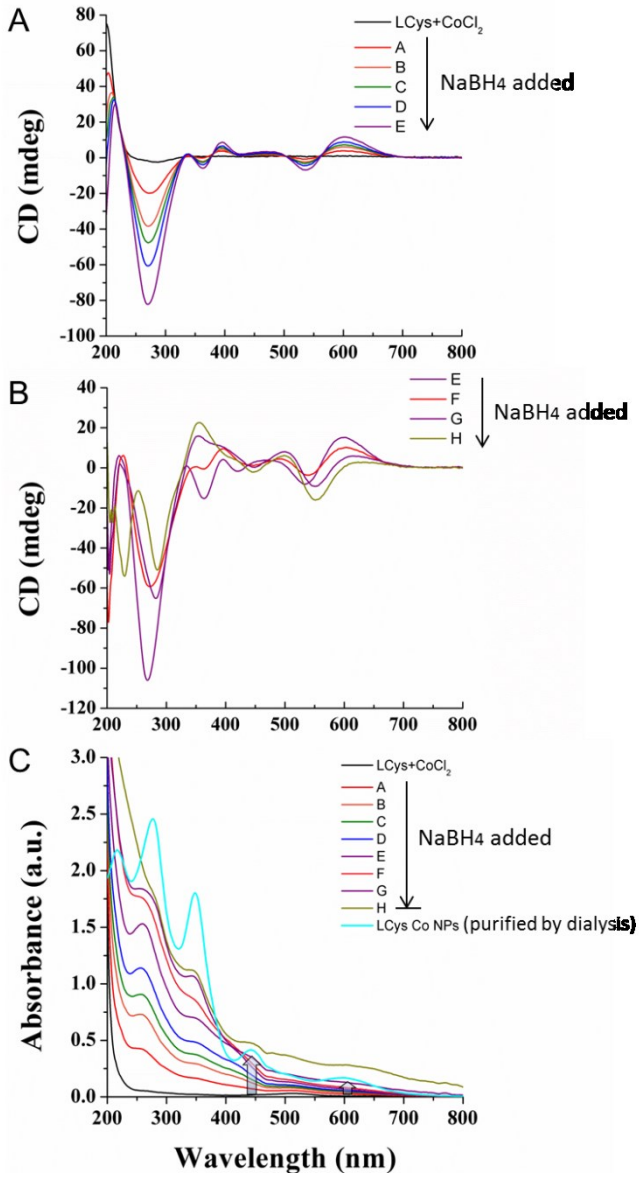
Figure 4.15. A and **B**, Continuously measured CD by adding a 1 mM NaBH$_4$ solution dropwise to a mixture of *L*-Cys and CoCl$_2$. **C**, Corresponding UV-vis absorbance spectra.
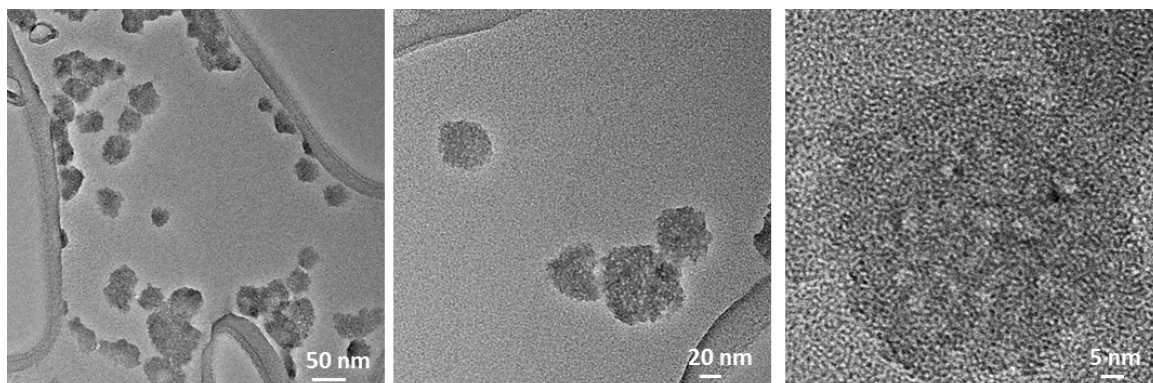
Figure 4.16. TEM images of sample E indicated in Fig. 4.12.
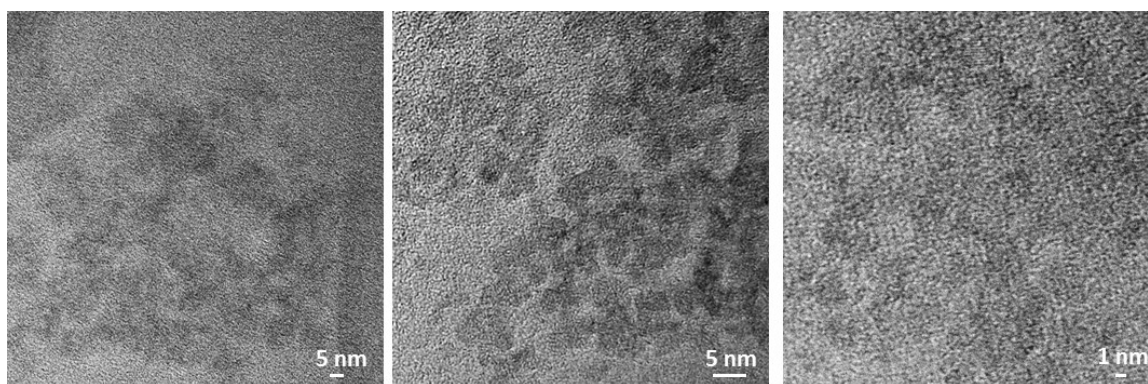
Figure 4.17. TEM images of sample **H** from in Fig. 4.12.

Note 1. Ligand effects on the chirality of NPs during the synthesis

Many factors can impose the crystalline structure of NPs. One of them is the geometry of metal-ligand complex. Bronstein *et al.* [138] demonstrated that the Fe oleate complexes, used to initiate NP formations, influences on structures, size and size distributions of developed iron oxide NPs. Other well-known examples are observed in Au NPs which show a twinned structure or a single-crystalline structure when made using citrate or cetyltrimethylammonium bromide (CTAB) stabilizers, respectively [139]. Since cobalt ions are Lewis acids, they easily form complexes with Lewis bases including Cys and penicillamine. The Cys molecules are expected to form at least one coordination with the NP, replacing one O atom from the NP surface with its S atom.

We examined the complex structural effects on the chirality of developed NPs during the synthesis by measuring absorbance and CD signals on every step after adding a 1 mM NaBH$_4$ solution dropwise to a mixture of L-Cys and CoCl$_2$. The mixture of L-Cys and CoCl$_2$ revealed a CD signal only at around 210 nm. As we added NaBH$_4$, new peaks appeared at 215, 274, 363, 396, 470, 536, and 603 nm (Fig. 4.10A). These peaks increased as more NaBH$_4$ was added. From the fifth addition (Fig. 4.10B, sample E), peaks gradually shifted to 230, 285, 356, 446, 498, and 551 nm (sample H). With TEM imaging, sample E shows more entangled metal-organic complexes, even larger than 50 nm (Fig. 4.11). After further reaction, they became solidified-core- and amorphous-shell-structured smaller NPs (Fig. 4.12), which confirms that the NPs were developed from Cys-cobalt complexes. According to the previously reported absorption spectrum of Cys-cobalt complexes [140,141], the optical signals at 230 nm and 285 nm are from the ligand-metal complex, and the new signals arising at around 500 nm are from inorganic cores (Fig . 4.15)

(a)   (b)
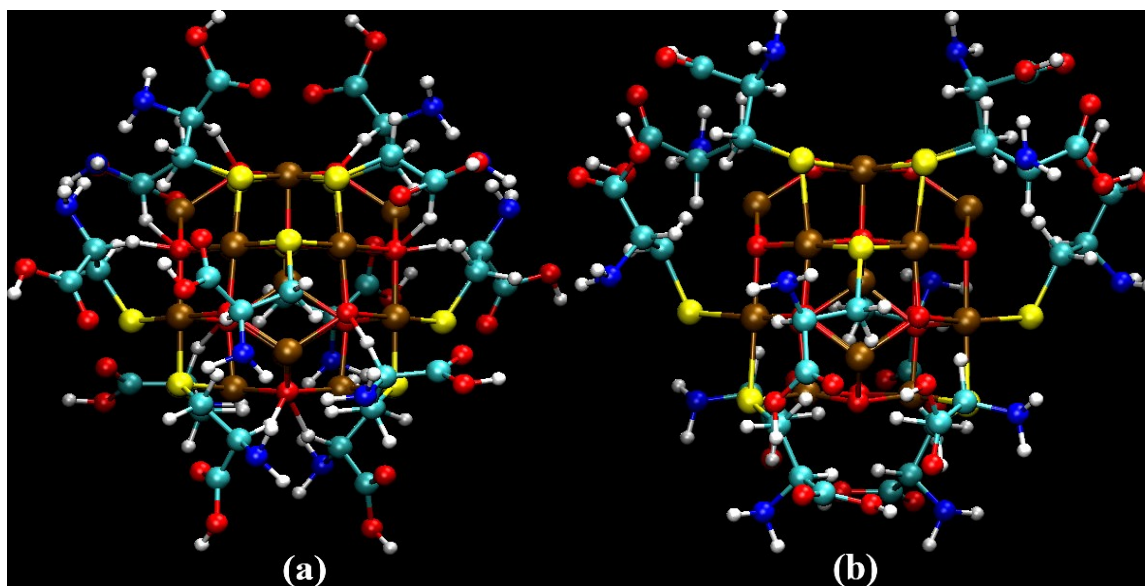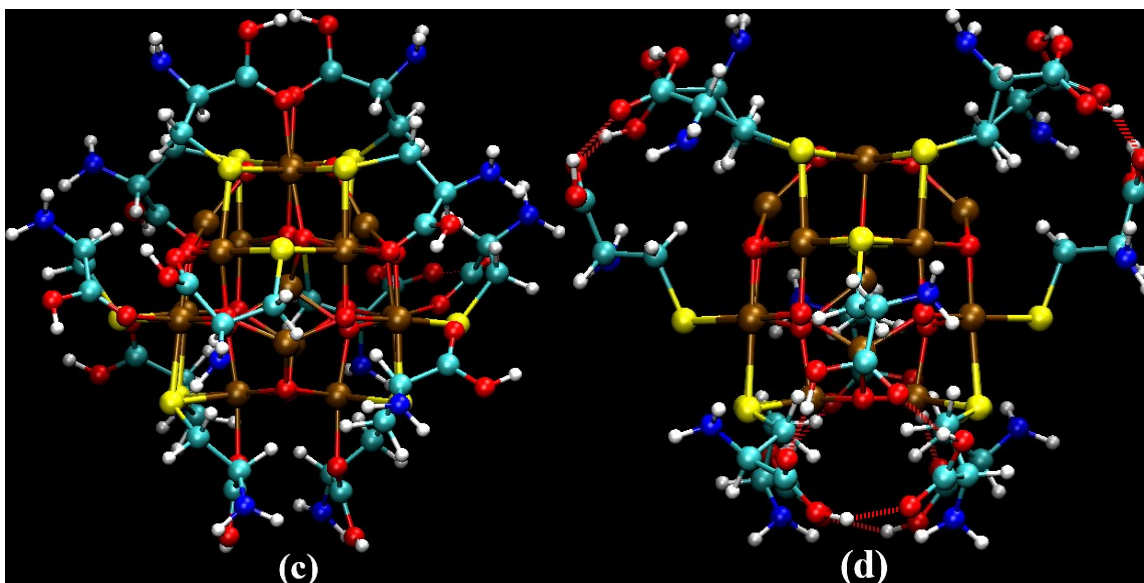
Figure 4.18. Structure of the cobalt oxide spinel NP functionalized with 12 ligand molecules. **(A)** Initial structure with *D*-Cys. **(B)** Initial structure with *L*-Cys. **(C)** Optimized structure with *D*-Cys. **(D)** Optimized structure with *L*-Cys.

Note 2: Raman active signals during the synthesis

The NP core movements are mostly breathing modes, which should be particularly active in the Raman measurements. As regards the ligands, the backbones of the Cys molecules either move as a liberating rigid body or open and close alternately like tweezers, while the amino groups presented rocking, wagging or twisting modes. It is important to acknowledge the fact that Cys molecules have these same modes in this wavenumber range, except for the librational motion, which typically arises due to constraints, in this case the double coordination of the ligands to the NP.

We experimentally verified this by measuring the Raman signal from *L*-Cys only, a mixture of *L*-Cys and CoCl$_2$, and the mixture with the gradual addition of NaBH$_4$ (Fig. 4.19). With increasing amounts of added NaBH$_4$, typical peaks from *L*-Cys gradually decreased while the 370 cm^{-1} peak and characteristic peaks of Co$_3$O$_4$ appeared.
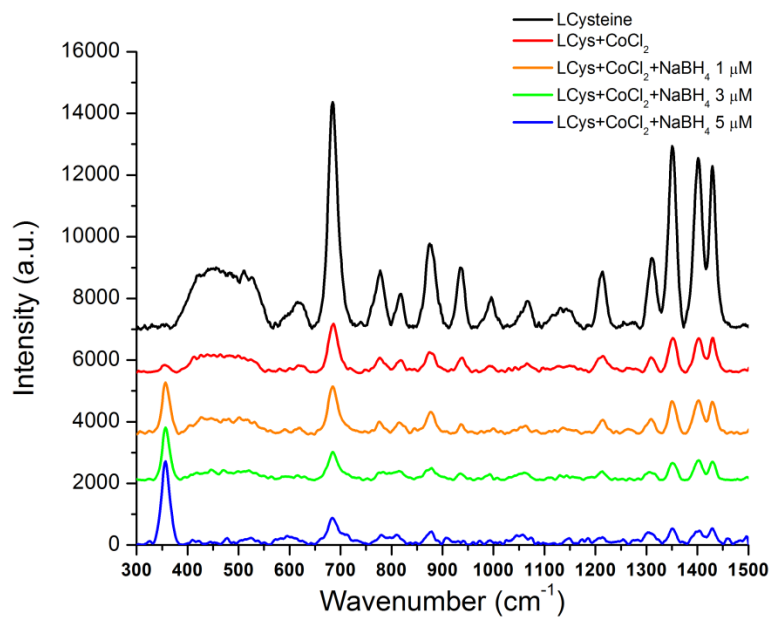
Figure 4.19. Raman spectra of *L*-Cys, mixture of *L*-Cys and CoCl$_2$, and the mixture with the gradual addition of NaBH$_4$.
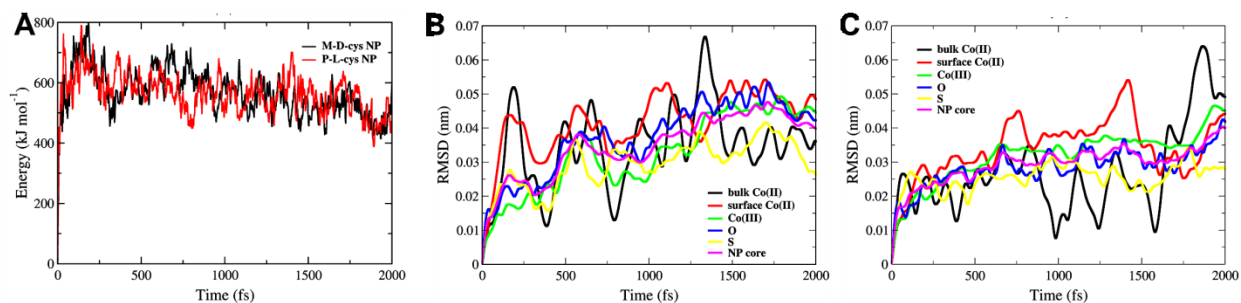
Figure 4.20. (A) Root-mean-square deviations (RMSD) of atomic positions for selected atomic species comprising the core of the M-*D*-Cys NP. Root-mean-square deviations (RMSD) of atomic positions for selected atomic species comprising the core of the P-*L*-Cys NP (B).
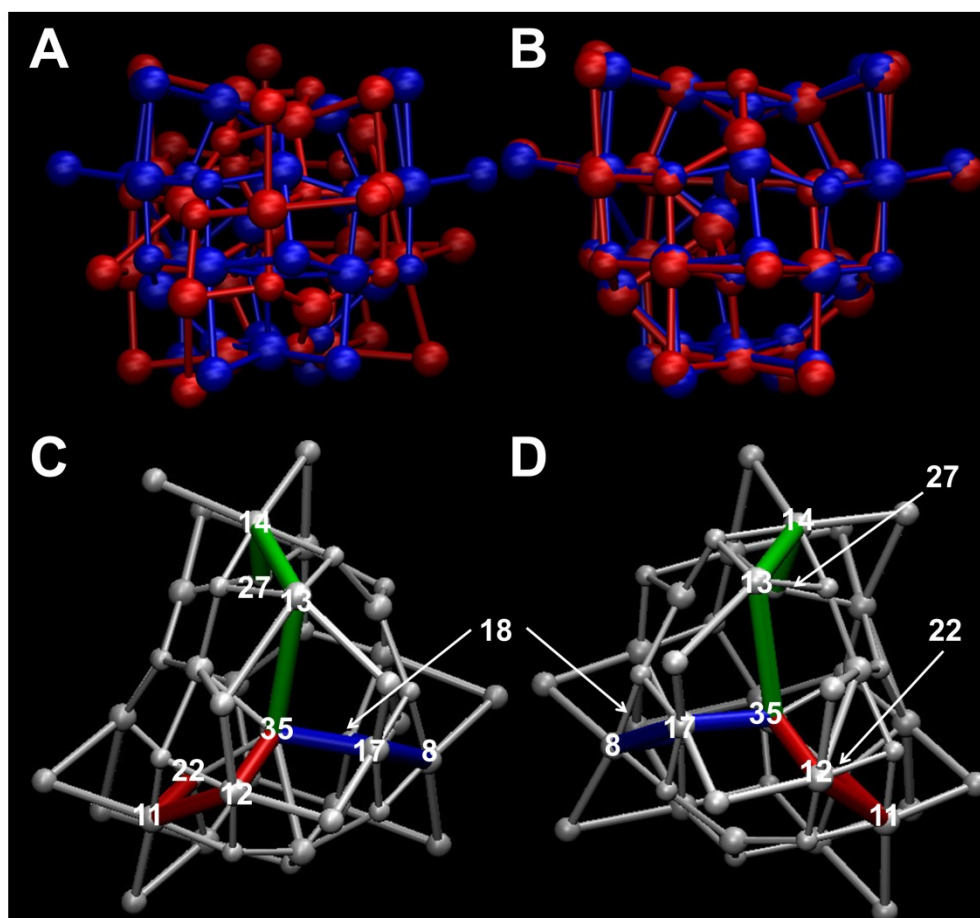
Figure 4.21. (A) Superimposed M-*D*-Cys (blue) and P-*L*-Cys (red) NP cores after 2000 fs of AIMD. **(B)** Superposed M-*D*-Cys (blue) and mirrored P-*L*-Cys (red) NP cores after 2000 fs of AIMD. **(C and D)** NP with M-*D*-Cys (C) and P-*L*-Cys (D) after 2000 fs of MD simulation with indicated atomic numbers.
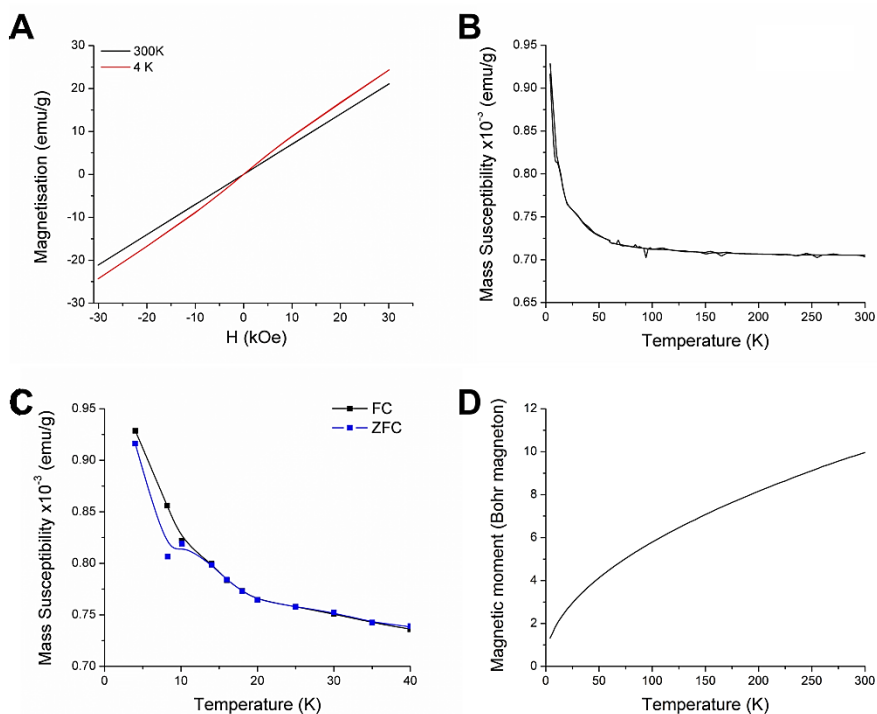
Figure 4.22. Magnetic properties of _L_-Cys Co₃O₄ NPs. (A) Magnetization hysteresis loop of at 300 K and 4 K indicating the paramagnetic properties of the NPs at different temperatures. (B) Mass magnetic susceptibility. (C) FC/ZFC curves. (D) Bohr magneton moments.
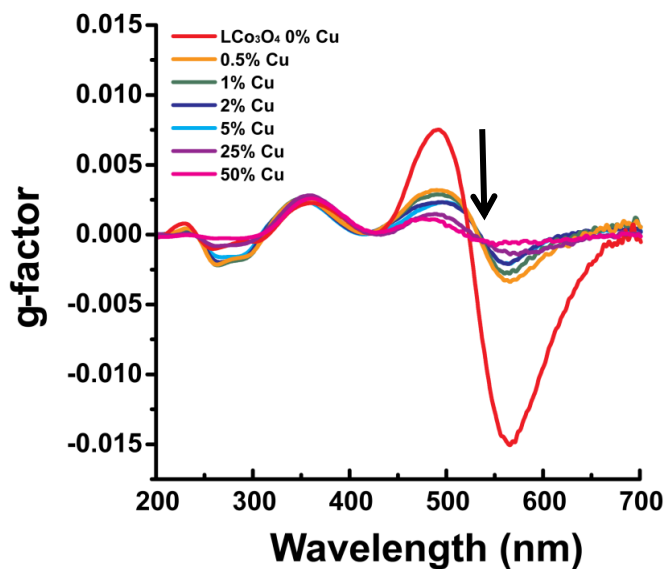
Figure 4.23. g-factor spectra of _L_-Cys Co₃O₄ NPs containing various amounts of Cu atoms.
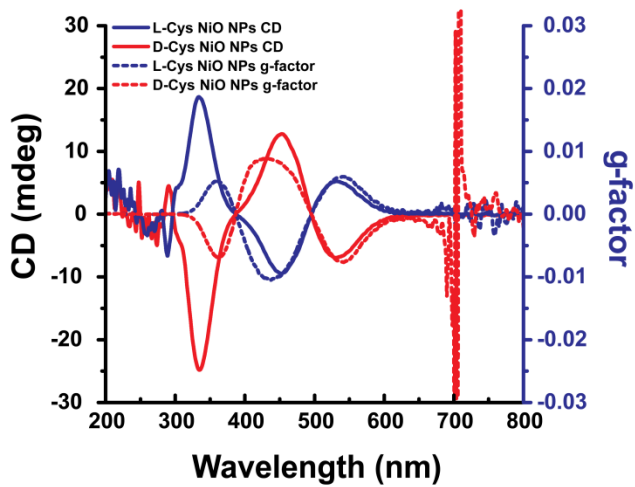
Figure 4.24. CD (solid) and g-factor (dotted) spectra of *L*-Cys- and *D*-Cys-stabilized NiO NPs.
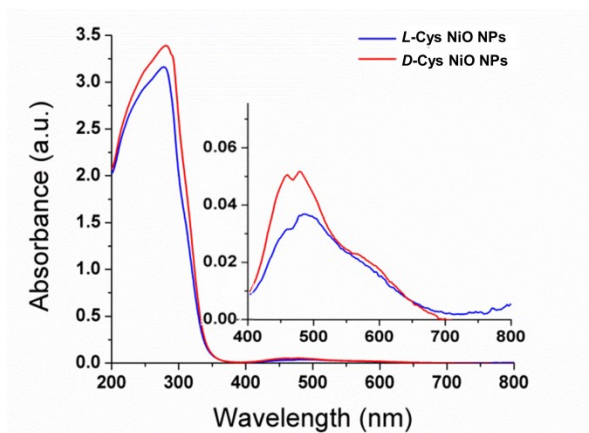
Figure 4.25. UV-vis absorbance spectra of *L*-Cys and *D*-Cys stabilized NiO NPs.
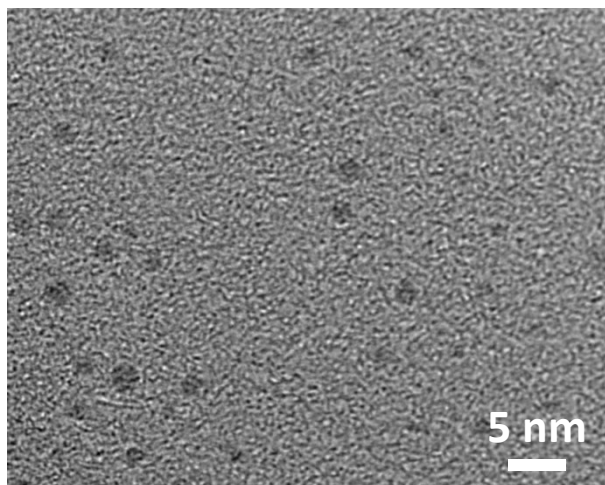
Figure 4.26. TEM image of *L*-Cys-stabilized NiO NPs.
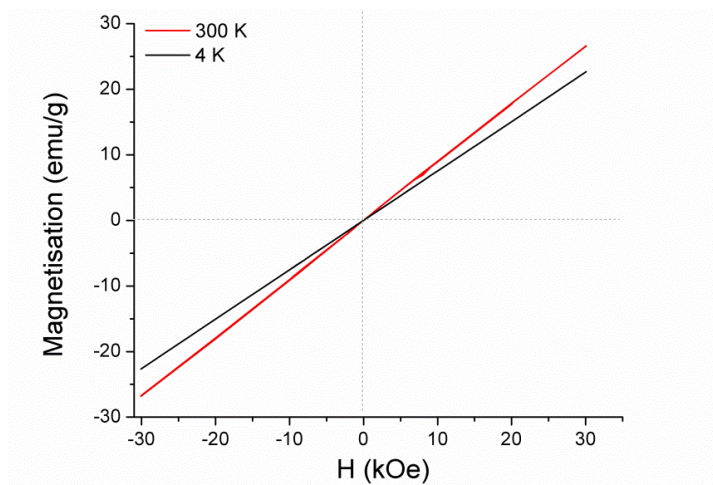
Figure 4.27. Magnetization hysteresis loop of *L*-Cys NiO NPs at 300 K and 4 K indicating the paramagnetic properties of *L*-Cys-stabilized NiO NPs at different temperatures.

Note 3. The magnetic dipole line strength and integrated absorption coefficient

The magnetic dipole line strength (also called dipole strength) for a transition between states 0 and a is defined as [120,121,142–144]

$$D_{MD} = \frac{-e\hbar}{2mc} \sum_{\Psi_a, \Psi_0} |<\Psi_0|\boldsymbol{L} + g\boldsymbol{S}|\Psi_a>|^2 \propto \boldsymbol{m}_{a0}{}^2$$

which is proportional to the square of magnetic transition dipole moment. The strong line strength induces strong absorption because the square is proportional to the Einstein A and B coefficients [120,121,142–144] which decide the transition rates and integrated absorption coefficient (IAC) as follows [144]:

$$\boldsymbol{m}_{a0}{}^2 = \frac{3hA_{a0}}{64\pi^4\omega^3}$$

$$B_{0a} = B_{a0} = \frac{A_{a0}}{8\pi hc\omega^3}$$

$$\text{IAC} = \int \varepsilon\, d\omega = \frac{B_{a0}h\omega N_0}{ln10}$$

Above, h is Planck's constant, ε is molar attenuation coefficient, $\omega=1/\lambda$ where λ is the wavelength of the transition, and N_0 is Avogadro's number. Consequently, strong angular momentum induces strong transition intensity of the magnetic moment and the absorbance of a material which agrees with the well-known theoretical derivations [23,145,146].

$$\Delta\varepsilon = \frac{16\pi^2\lambda N\beta\sigma_{0a}(\omega)R_{0a}}{3(2303)\hbar c}$$

$$\varepsilon = \frac{4\pi^2\lambda N}{3(2303)\hbar c}\frac{\beta^2}{n}D_{0a}\rho_{0a}(\omega)$$

Note 4. Anisotropy g factor

According to the Lorentz theory, the field on the chromophore is given by $F = \beta E$ with $\beta = (n^2 + 2)/3$ [147]. From these two equations, the g factor is given by

$$g = \frac{4n}{\beta} \frac{\sigma_{0a}(\omega)}{\rho_{0a}(\omega)} \frac{R_{0a}}{D_{0a}}$$

g is seen to depend on the ratio of the shape factors for CD and absorption as well as a weak variation with n/β. Moscowitz [26] has shown that in many strong bands the CD signal and the absorption signal have the same shape. In this case $\sigma_{0a}(\omega) / \rho_{0a}(\omega) = 1$ and

$$g = \frac{4n}{\beta} \frac{R_{0a}}{D_{0a}}$$

considering

$$\frac{n}{\beta} = \frac{3n}{n^2 + 2}$$

This is close to unity for most realistic values for n. It is unity at $n = 1$, reaches a maximum of 1.06 at $n = \sqrt{2}$, goes through unity at $n = 2$, and attains a value of 0.91 at $n = 2.5$. We see then the validity of this formula depends not on the absence of an internal field but in the cancellation of the intrinsic effect of refractive index by the internal field dependence. Thus, g is given as $g = 4R/D$.
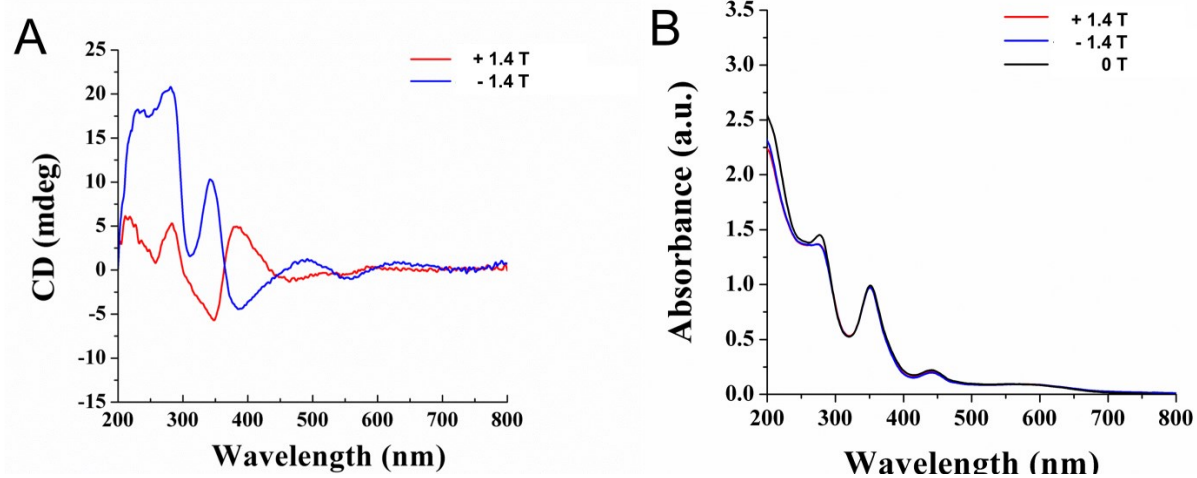
Figure 4.28. MCD (A) and absorbance (B) spectra for *DL*-Cys Co_3O_4 NPs.
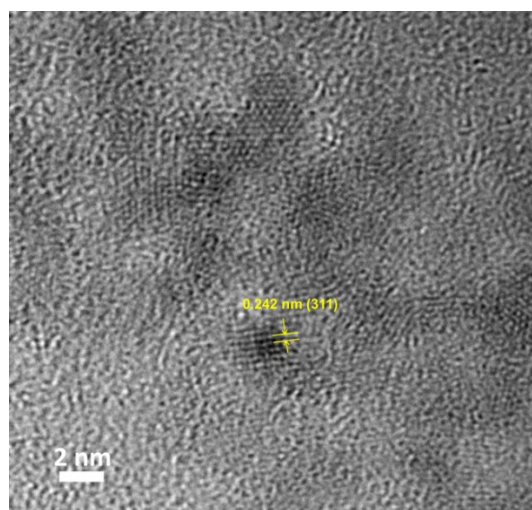
Figure 4.29. HR TEM image of *DL*-Cys Co_3O_4 NPs demonstrating the undistorted crystal lattice.
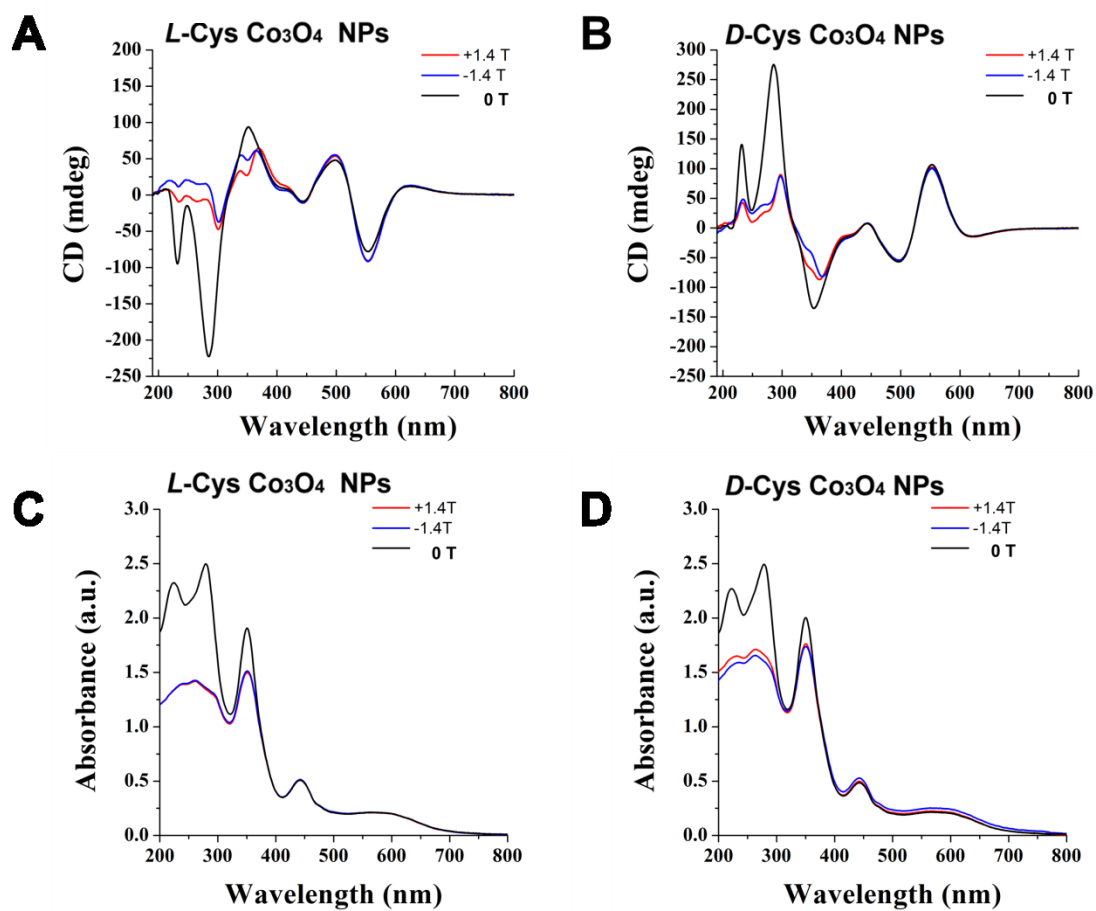
Figure 4.30. MCD of *L*-Cys (A) and *D*-Cys (B) Co$_3$O$_4$ NPs, and absorbance spectra of *L*-Cys (D) and *D*-Cys (D) Co$_3$O$_4$ NPs at +1.4 T, -1.4 T, and 0 T magnetic fields.
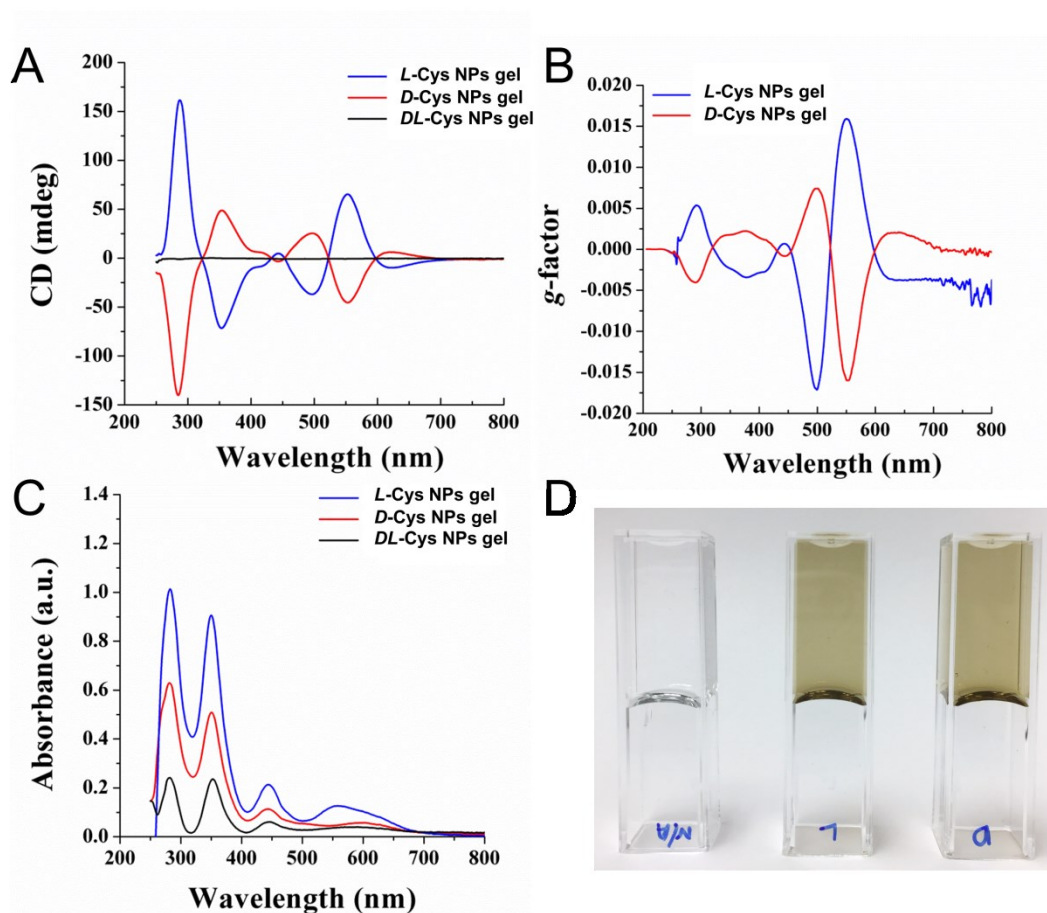
Figure 4.31. **A** and **B,** CD (A) and calculated g-factor graphs (B) of Co NPs hydrogels. **C,** UV-vis absorption graphs. **D**, Photographic images of gels that do not contain NPs (left) and that contain NPs (middle and right).
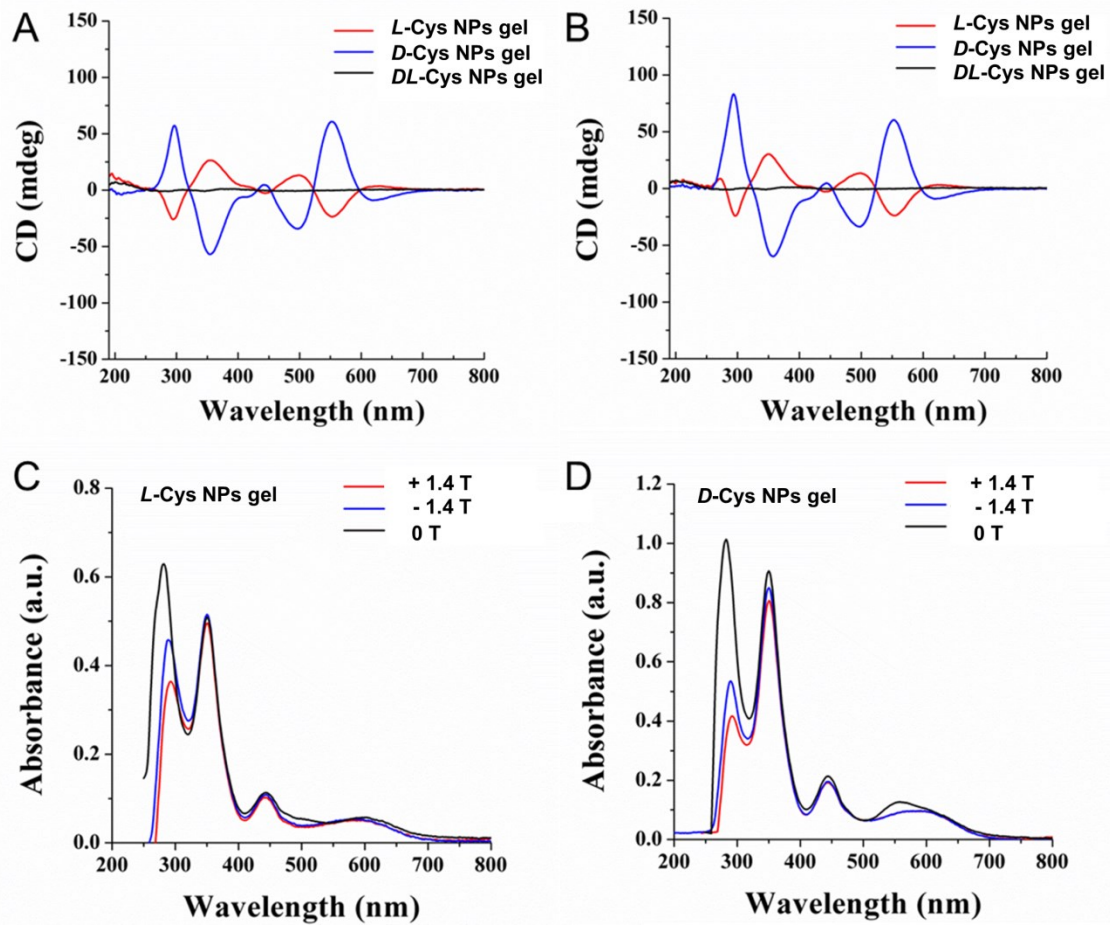
Figure 4.32. A and **B**, MCD data of Co NPs hydrogels at 1.4 T (A) and -1.4 T (B) magnetic fields. **C** and **D**, Corresponding UV-vis absorbance graphs of A (C) and B (D).
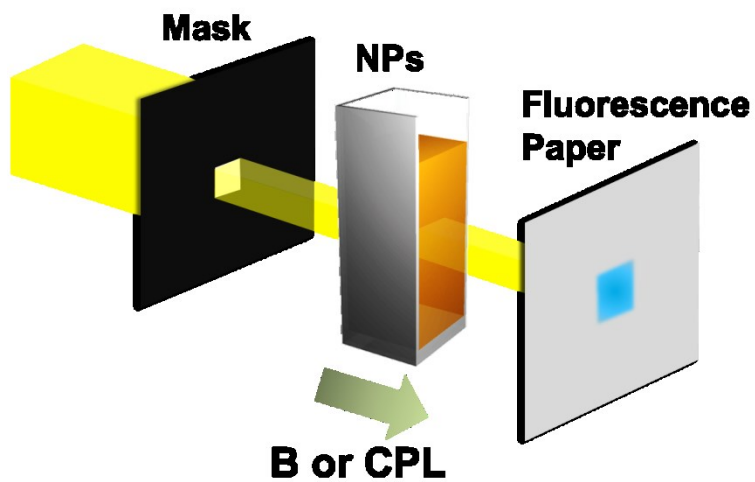
Scheme 4.2. Experimental set up for optical modulations.
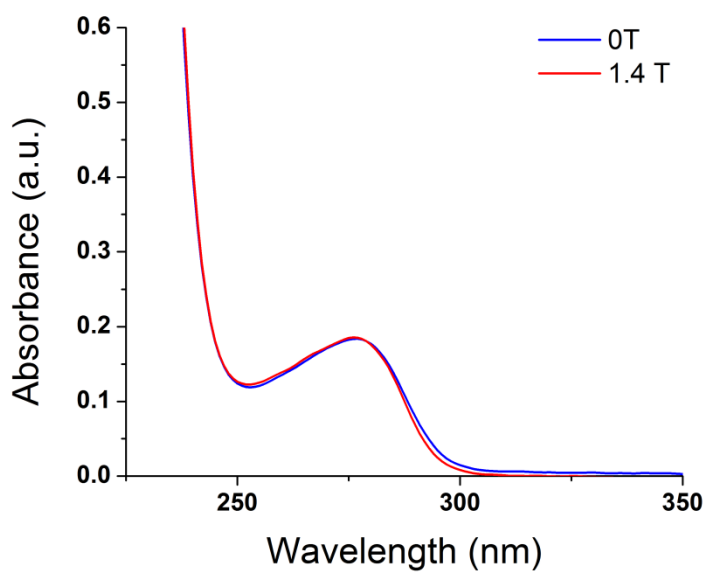
Fig 4.33. UV absorbance of human serum albumin with and without external magnetic field.
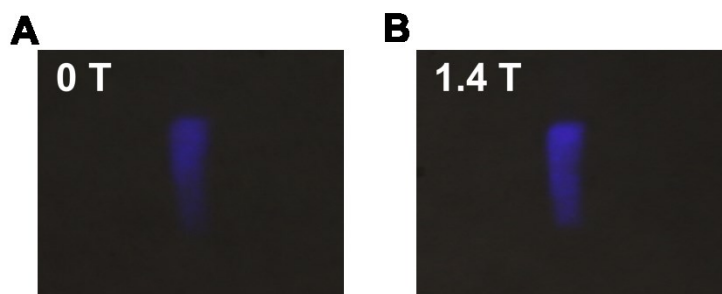
Figure S34. Photographic images of blue emitting light from the fluorescence paper with 350 nm excitation wavelength without magnetic field (A) and with magnetic field (B).

Note 5. Optical modulations

The total intensity of MCD and absorbance was significantly decreased (~30% for *D*-cys at 280 nm) upon the application of the magnetic field (Fig. 4.30). This effect is attributed to magneto-dielectric coupling in the distorted lattice of Co_3O_4 NPs [148,149]. The dielectric constant is directly related to the absorption coefficient, and decreases when a magnetic field is applied to magnetite, liquid crystals, and ceramics due to a coupling between the magnetization and the polarization [150–152]. When dipoles are fixed in a particular direction, polarizability is lost, inducing the decrement of the dielectric constant. A protein (human serum albumin), which also has an absorbance at 280 nm, did not show this effect (Fig. 4.33). As a control experiment, we also used a 350 nm light source with the **Scheme 2** experimental set up. Almost no change was observed in the emission intensity with changing magnetic field (Fig. 4.34) since the magneto-dielectric effect is not strong enough in that range (Fig. 4.30).

Table 4.1. Reference hexacoordinated Co(III) octahedron with crystallographic bond lengths and angles. The chirality index G_0 is null for this highly symmetrical structure.
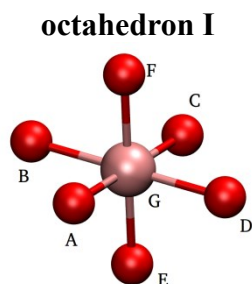
Octahedron Structure and Chirality Index	Bond Length (nm)	Angle (°)
	$r_{G-A} = 0.192$	$a_{A-G-B} = 83.73$
	$r_{G-B} = 0.192$	$a_{A-G-D} = 96.27$
	$r_{G-C} = 0.192$	$a_{A-G-E} = 83.73$
octahedron I	$r_{G-D} = 0.192$	$a_{A-G-F} = 96.27$
	$r_{G-E} = 0.192$	$a_{B-G-C} = 96.27$
	$r_{G-F} = 0.192$	$a_{B-G-E} = 83.73$
		$a_{B-G-F} = 96.27$
		$a_{C-G-D} = 83.73$
$G_0 = 0.000$		$a_{C-G-E} = 96.27$
HCM = 0.0000		$a_{C-G-F} = 83.73$
		$a_{D-G-E} = 96.27$
		$a_{D-G-F} = 83.73$

Note: Figures in Table 4.2 to 4.12 use the same labels for the atoms coordinated to the central Co(III) atom (G), namely: A and B are S atoms from two different *D*-Cys units, whereas C, D and E are O atoms from the NP core and F is a carbonyl O atom from the same *D*-Cys molecule of atom B.

Table 4.2. Bond lengths, bond orders, angles between coordination positions and atomic spin population on atomic sites for the octahedron around atom Co(III) number 9. The Osipov chirality index G_0 and the Hausdorff chirality measure (HCM) are below the atomic structure of the octahedron.

Octahedron Structure and Chirality Indexes	Bond Length (nm)	Bond Order	Angle (°)	Spin Population
	$r_{G-A} = 0.242$	$BO_{G-A} = 0.62$	$a_{A\text{-}G\text{-}B} = 84.79$	$A = -0.01$
	$r_{G-B} = 0.239$	$BO_{G-B} = 0.73$	$a_{A\text{-}G\text{-}D} = 98.07$	$B = 0.00$
octahedron II	$r_{G-C} = 0.190$	$BO_{G-C} = 0.51$	$a_{A\text{-}G\text{-}E} = 89.86$	$C = 0.05$
	$r_{G-D} = 0.192$	$BO_{G-D} = 0.59$	$a_{A\text{-}G\text{-}F} = 86.01$	$D = 0.13$
	$r_{G-E} = 0.193$	$BO_{G-E} = 0.57$	$a_{B\text{-}G\text{-}C} = 95.68$	$E = 0.02$
	$r_{G-F} = 0.202$	$BO_{G-F} = 0.45$	$a_{B\text{-}G\text{-}E} = 86.02$	$F = 0.00$
			$a_{B\text{-}G\text{-}F} = 84.72$	$G = -0.01$
$G_0 = -0.008$			$a_{C\text{-}G\text{-}D} = 81.47$	
HCM = 0.0195			$a_{C\text{-}G\text{-}E} = 91.43$	
			$a_{C\text{-}G\text{-}F} = 92.76$	
			$a_{D\text{-}G\text{-}E} = 93.26$	
			$a_{D\text{-}G\text{-}F} = 96.15$	

Table 4.3. Bond lengths, bond orders, angles between coordination positions and atomic spin population on atomic sites for the octahedron around atom Co(III) number 12. The Osipov chirality index G_0 and the Hausdorff chirality measure (HCM) are below the atomic structure of the octahedron.

Octahedron Structure and Chirality Index	Bond Length (nm)	Bond Order	Angle (°)	Spin Population
	$r_{G-A} = 0.243$	$BO_{G-A} = 0.52$	$a_{A-G-B} = 85.65$	$A = 0.12$
	$r_{G-B} = 0.235$	$BO_{G-B} = 0.71$	$a_{A-G-D} = 95.10$	$B = -0.09$
octahedron III	$r_{G-C} = 0.190$	$BO_{G-C} = 0.58$	$a_{A-G-E} = 95.31$	$C = 0.03$
	$r_{G-D} = 0.191$	$BO_{G-D} = 0.58$	$a_{A-G-F} = 87.84$	$D = 0.07$
	$r_{G-E} = 0.199$	$BO_{G-E} = 0.58$	$a_{B-G-C} = 96.75$	$E = 0.17$
	$r_{G-F} = 0.198$	$BO_{G-F} = 0.49$	$a_{B-G-E} = 85.31$	$F = 0.00$
			$a_{B-G-F} = 86.07$	$G = 0.03$
$G_0 = -0.007$			$a_{C-G-D} = 82.51$	
HCM = 0.0290			$a_{C-G-E} = 86.77$	
			$a_{C-G-F} = 90.45$	
			$a_{D-G-E} = 94.65$	
			$a_{D-G-F} = 93.92$	

Table 4.4. Bond lengths, bond orders, angles between coordination positions and atomic spin population on atomic sites for the octahedron around atom Co(III) number 14. The Osipov chirality index G_0 and the Hausdorff chirality measure (HCM) are below the atomic structure of the octahedron.

Octahedron Structure and Chirality Index	Bond Length (nm)	Bond Order	Angle (°)	Spin Population
	$r_{G-A} = 0.241$	$BO_{G-A} = 0.61$	$a_{A-G-B} = 84.86$	$A = -0.01$
	$r_{G-B} = 0.240$	$BO_{G-B} = 0.67$	$a_{A-G-D} = 100.4$	$B = 0.00$
octahedron IV	$r_{G-C} = 0.190$	$BO_{G-C} = 0.56$	$a_{A-G-E} = 84.93$	$C = 0.09$
	$r_{G-D} = 0.189$	$BO_{G-D} = 0.61$	$a_{A-G-F} = 88.46$	$D = 0.01$
	$r_{G-E} = 0.199$	$BO_{G-E} = 0.54$	$a_{B-G-C} = 93.17$	$E = 0.03$
	$r_{G-F} = 0.199$	$BO_{G-F} = 0.47$	$a_{B-G-E} = 88.85$	$F = 0.00$
			$a_{B-G-F} = 85.09$	$G = 0.05$
$G_0 = -0.007$			$a_{C-G-D} = 81.66$	
HCM = 0.0338			$a_{C-G-E} = 97.47$	
			$a_{C-G-F} = 88.96$	
			$a_{D-G-E} = 90.52$	
			$a_{D-G-F} = 96.08$	

Table 4.5. Bond lengths, bond orders, angles between coordination positions and atomic spin population on atomic sites for the octahedron around atom Co(III) number 8. The Osipov chirality index G_0 and the Hausdorff chirality measure (HCM) are below the atomic structure of the octahedron.

Octahedron Structure and Chirality Index	Bond Length (nm)	Bond Order	Angle (°)	Spin Population
	$r_{G-A} = 0.237$	$BO_{G-A} = 0.68$	$a_{A-G-B} = 86.13$	$A = 0.01$
	$r_{G-B} = 0.239$	$BO_{G-B} = 0.69$	$a_{A-G-D} = 96.60$	$B = -0.08$
octahedron V	$r_{G-C} = 0.192$	$BO_{G-C} = 0.46$	$a_{A-G-E} = 88.00$	$C = 0.07$
	$r_{G-D} = 0.189$	$BO_{G-D} = 0.58$	$a_{A-G-F} = 89.11$	$D = 0.09$
	$r_{G-E} = 0.195$	$BO_{G-E} = 0.59$	$a_{B-G-C} = 95.48$	$E = 0.11$
	$r_{G-F} = 0.200$	$BO_{G-F} = 0.45$	$a_{B-G-E} = 88.69$	$F = 0.00$
			$a_{B-G-F} = 85.05$	$G = 0.03$
$G_0 = 0.003$			$a_{C-G-D} = 81.78$	
HCM = 0.0130			$a_{C-G-E} = 92.58$	
			$a_{C-G-F} = 90.48$	
			$a_{D-G-E} = 92.53$	
			$a_{D-G-F} = 93.84$	

Table 4.6. Bond lengths, bond orders, angles between coordination positions and atomic spin population on atomic sites for the octahedron around atom Co(III) number 15. The Osipov chirality index G_0 and the Hausdorff chirality measure (HCM) are below the atomic structure of the octahedron.

Octahedron Structure and Chirality Index	Bond Length (nm)	Bond Order	Angle (°)	Spin Population
	$r_{G-A} = 0.246$	$BO_{G-A} = 0.64$	$a_{A-G-B} = 86.69$	$A = 0.00$
	$r_{G-B} = 0.235$	$BO_{G-B} = 0.74$	$a_{A-G-D} = 96.62$	$B = -0.01$
octahedron VI	$r_{G-C} = 0.191$	$BO_{G-C} = 0.54$	$a_{A-G-E} = 88.62$	$C = 0.04$
	$r_{G-D} = 0.191$	$BO_{G-D} = 0.58$	$a_{A-G-F} = 89.25$	$D = -0.01$
	$r_{G-E} = 0.196$	$BO_{G-E} = 0.53$	$a_{B-G-C} = 95.33$	$E = 0.03$
	$r_{G-F} = 0.198$	$BO_{G-F} = 0.48$	$a_{B-G-E} = 87.08$	$F = 0.00$
			$a_{B-G-F} = 85.54$	$G = 0.01$
$G_0 = 0.006$			$a_{C-G-D} = 81.37$	
HCM = 0.0081			$a_{C-G-E} = 90.53$	
			$a_{C-G-F} = 91.86$	
			$a_{D-G-E} = 93.89$	
			$a_{D-G-F} = 93.58$	

Table 4.7. Bond lengths, bond orders, angles between coordination positions and atomic spin population on atomic sites for the octahedron around atom Co(III) number 13. The Osipov chirality index G_0 and the Hausdorff chirality measure (HCM) are below the atomic structure of the octahedron.

Octahedron Structure and Chirality Index	Bond Length (nm)	Bond Order	Angle (°)	Spin Population
	$r_{G-A} = 0.243$	$BO_{G-A} = 0.54$	$a_{A-G-B} = 84.15$	$A = -0.09$
	$r_{G-B} = 0.245$	$BO_{G-B} = 0.55$	$a_{A-G-D} = 99.41$	$B = 0.09$
octahedron VII	$r_{G-C} = 0.190$	$BO_{G-C} = 0.52$	$a_{A-G-E} = 83.31$	$C = 0.01$
	$r_{G-D} = 0.187$	$BO_{G-D} = 0.67$	$a_{A-G-F} = 89.29$	$D = 0.09$
	$r_{G-E} = 0.198$	$BO_{G-E} = 0.48$	$a_{B-G-C} = 94.30$	$E = 0.17$
	$r_{G-F} = 0.200$	$BO_{G-F} = 0.40$	$a_{B-G-E} = 96.49$	$F = 0.04$
			$a_{B-G-F} = 82.73$	$G = 2.06$
$G_0 = 0.010$			$a_{C-G-D} = 82.14$	
$HCM = 0.0567$			$a_{C-G-E} = 96.72$	
			$a_{C-G-F} = 90.67$	
			$a_{D-G-E} = 87.17$	
			$a_{D-G-F} = 94.04$	

Table 4.8. Bond lengths, bond orders, angles between coordination positions and atomic spin population on atomic sites for the octahedron around atom Co(III) number 7. The Osipov chirality index G_0 and the Hausdorff chirality measure (HCM) are below the atomic structure of the octahedron.
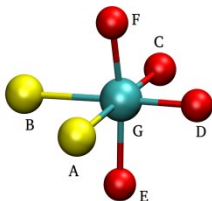
Octahedron Structure and Chirality Index	Bond Length (nm)	Bond Order	Angle (°)	Spin Population
	$r_{G-A} = 0.243$	$BO_{G-A} = 0.57$	$a_{A\text{-}G\text{-}B} = 84.19$	$A = -0.11$
	$r_{G-B} = 0.238$	$BO_{G-B} = 0.66$	$a_{A\text{-}G\text{-}D} = 94.58$	$B = 0.01$
octahedron VIII	$r_{G-C} = 0.191$	$BO_{G-C} = 0.55$	$a_{A\text{-}G\text{-}E} = 87.42$	$C = 0.13$
	$r_{G-D} = 0.187$	$BO_{G-D} = 0.64$	$a_{A\text{-}G\text{-}F} = 89.34$	$D = 0.05$
	$r_{G-E} = 0.194$	$BO_{G-E} = 0.58$	$a_{B\text{-}G\text{-}C} = 99.07$	$E = 0.11$
	$r_{G-F} = 0.200$	$BO_{G-F} = 0.46$	$a_{B\text{-}G\text{-}E} = 87.83$	$F = 0.00$
			$a_{B\text{-}G\text{-}F} = 83.90$	$G = 0.03$
$G_0 = 0.019$			$a_{C\text{-}G\text{-}D} = 82.30$	
HCM = 0.0250			$a_{C\text{-}G\text{-}E} = 90.36$	
			$a_{C\text{-}G\text{-}F} = 93.32$	
			$a_{D\text{-}G\text{-}E} = 95.57$	
			$a_{D\text{-}G\text{-}F} = 92.64$	

Table 4.9. Bond lengths, bond orders, angles between coordination positions and atomic spin population on atomic sites for the octahedron around atom Co(III) number 11. The Osipov's chirality index G_0 and the Hausdorff chirality measure (HCM) are below the atomic structure of the octahedron.
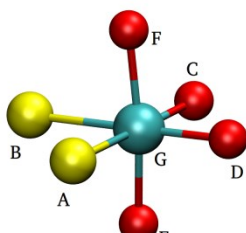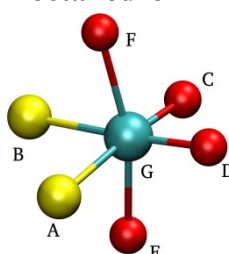
Octahedron Structure and Chirality Index	Bond Length (nm)	Bond Order	Angle (°)	Spin Population
	$r_{G-A} = 0.240$	$BO_{G-A} = 0.65$	$a_{A-G-B} = 84.93$	$A = -0.01$
	$r_{G-B} = 0.237$	$BO_{G-B} = 0.68$	$a_{A-G-D} = 98.07$	$B = -0.01$
octahedron IX	$r_{G-C} = 0.189$	$BO_{G-C} = 0.55$	$a_{A-G-E} = 82.66$	$C = 0.07$
	$r_{G-D} = 0.187$	$BO_{G-D} = 0.67$	$a_{A-G-F} = 92.14$	$D = 0.03$
	$r_{G-E} = 0.226$	$BO_{G-E} = 0.54$	$a_{B-G-C} = 93.50$	$E = 0.02$
	$r_{G-F} = 0.237$	$BO_{G-F} = 0.37$	$a_{B-G-E} = 83.79$	$F = 0.01$
			$a_{B-G-F} = 81.80$	$G = 0.06$
$G_0 = 0.021$			$a_{C-G-D} = 83.72$	
HCM = 0.0464			$a_{C-G-E} = 89.60$	
			$a_{C-G-F} = 95.18$	
			$a_{D-G-E} = 98.06$	
			$a_{D-G-F} = 96.52$	

Table 4.10. Bond lengths, bond orders, angles between coordination positions and atomic spin population on atomic sites for the octahedron around atom Co(III) number 10. The Osipov chirality index G_0 and the Hausdorff chirality measure (HCM) are below the atomic structure of the octahedron.
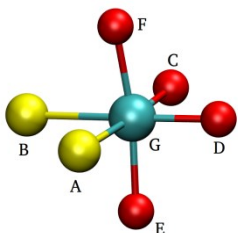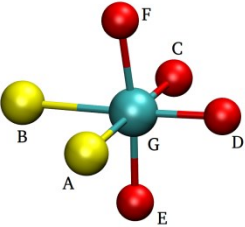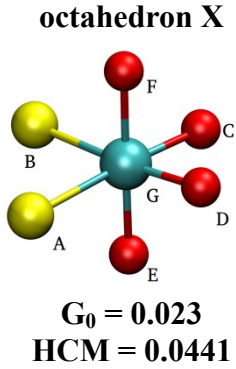
Octahedron Structure and Chirality Index	Bond Length (nm)	Bond Order	Angle (°)	Spin Population
	$r_{G-A} = 0.242$	$BO_{G-A} = 0.56$	$a_{A-G-B} = 83.38$	$A = 0.00$
	$r_{G-B} = 0.235$	$BO_{G-B} = 0.71$	$a_{A-G-D} = 98.83$	$B = -0.01$
octahedron X	$r_{G-C} = 0.190$	$BO_{G-C} = 0.58$	$a_{A-G-E} = 84.75$	$C = 0.04$
	$r_{G-D} = 0.189$	$BO_{G-D} = 0.54$	$a_{A-G-F} = 96.88$	$D = 0.02$
	$r_{G-E} = 0.195$	$BO_{G-E} = 0.53$	$a_{B-G-C} = 96.66$	$E = 0.02$
	$r_{G-F} = 0.191$	$BO_{G-F} = 0.51$	$a_{B-G-E} = 90.97$	$F = 0.00$
			$a_{B-G-F} = 88.24$	$G = -0.06$
$G_0 = 0.023$			$a_{C-G-D} = 81.43$	
HCM = 0.0441			$a_{C-G-E} = 90.98$	
			$a_{C-G-F} = 87.39$	
			$a_{D-G-E} = 93.16$	
			$a_{D-G-F} = 87.57$	

Table 4.11. Bond lengths, bond orders, angles between coordination positions and atomic spin population on atomic sites for the octahedron around atom Co(III) number 6. The Osipov chirality index G_0 and the Hausdorff chirality measure (HCM) are below the atomic structure of the octahedron.
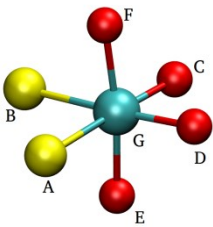
Octahedron Structure and Chirality Index	Bond Length (nm)	Bond Order	Angle (°)	Spin Population
	$r_{G-A} = 0.241$	$BO_{G-A} = 0.58$	$a_{A-G-B} = 82.88$	A = -0.08
	$r_{G-B} = 0.238$	$BO_{G-B} = 0.67$	$a_{A-G-D} = 97.98$	B = -0.10
octahedron XI	$r_{G-C} = 0.188$	$BO_{G-C} = 0.56$	$a_{A-G-E} = 82.28$	C = -0.01
	$r_{G-D} = 0.188$	$BO_{G-D} = 0.65$	$a_{A-G-F} = 89.32$	D = 0.04
	$r_{G-E} = 0.221$	$BO_{G-E} = 0.42$	$a_{B-G-C} = 96.20$	E = 0.11
	$r_{G-F} = 0.238$	$BO_{G-F} = 0.35$	$a_{B-G-E} = 82.89$	F = 0.02
			$a_{B-G-F} = 80.78$	G = 2.16
$G_0 = 0.033$			$a_{C-G-D} = 82.87$	
HCM = 0.0424			$a_{C-G-E} = 94.16$	
			$a_{C-G-F} = 93.97$	
			$a_{D-G-E} = 95.95$	
			$a_{D-G-F} = 100.5$	

Table 4.12. Bond lengths, bond orders, angles between coordination positions and atomic spin population on atomic sites for the octahedron around atom Co(III) number 17. The Osipov chirality index G_0 and the Hausdorff chirality measure (HCM) are below the atomic structure of the octahedron.
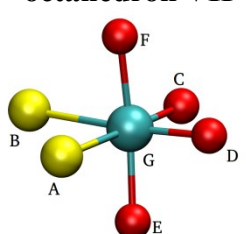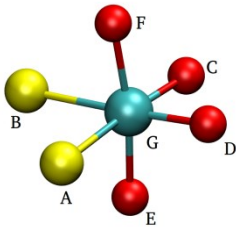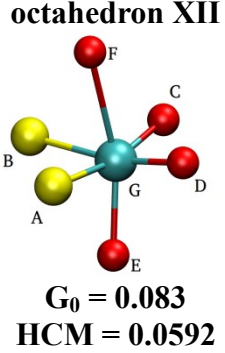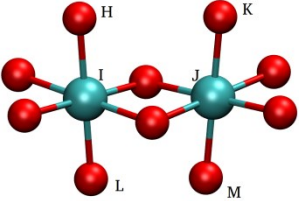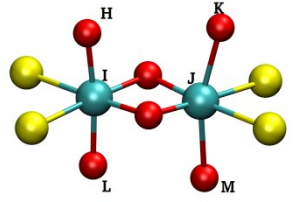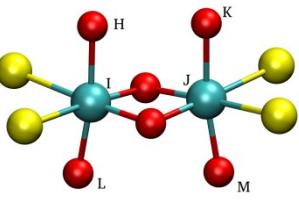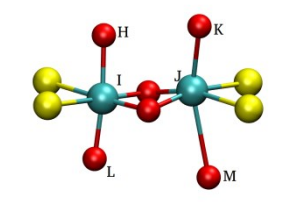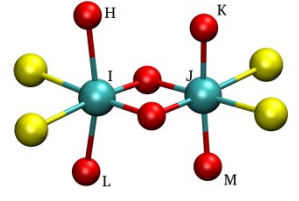
Octahedron Structure and Chirality Index	Bond Length (nm)	Bond Order	Angle (°)	Spin Population
	$r_{G–A} = 0.236$	$BO_{G–A} = 0.69$	$a_{A-G-B} = 83.01$	$A = 0.09$
	$r_{G–B} = 0.237$	$BO_{G–B} = 0.68$	$a_{A-G-D} = 95.92$	$B = 0.12$
octahedron XII	$r_{G–C} = 0.191$	$BO_{G–C} = 0.62$	$a_{A-G-E} = 78.84$	$C = 0.09$
	$r_{G–D} = 0.186$	$BO_{G–D} = 0.71$	$a_{A-G-F} = 96.96$	$D = 0.07$
	$r_{G–E} = 0.284$	$BO_{G–E} = 0.21$	$a_{B-G-C} = 94.52$	$E = 0.17$
	$r_{G–F} = 0.234$	$BO_{G–F} = 0.38$	$a_{B-G-E} = 77.33$	$F = -0.02$
			$a_{B-G-F} = 82.50$	$G = -2.14$
$G_0 = 0.083$			$a_{C-G-D} = 82.86$	
HCM = 0.0592			$a_{C-G-E} = 88.01$	
			$a_{C-G-F} = 95.52$	
			$a_{D-G-E} = 86.63$	
			$a_{D-G-F} = 113.6$	

Table 4.13. Relative orientation between adjoining octahedra sharing an edge with two O atoms (both O atoms belong to the crystal, not the ligands). Dihedral angles between Co-O axial bonds are reported along with the Osipov chirality index (G_0) and the Hausdorff chirality measure (HCM) for the pair of octahedra. G_0 values were neither weighted nor scaled, thus the values for the pair of octahedra are necessarily larger than those reported for single octahedra in Tables 4.2 to 4.12

Octahedra	Dihedral HIJK (°)	Dihedral LIJM (°)	G_0	HCM
Reference structure	0.00	0.00	0.000	0.0000
Octahedra VI and XI	-3.98	6.22	0.587	0.0275
Octahedra VIII and II	2.06	-5.47	0.360	0.0207
Octahedra V and XII	15.87	0.69	0.740	0.0575
Octahedra IX and III	3.60	-12.35	0.136	0.0372
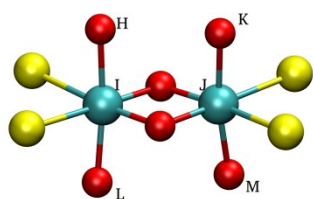
Octahedra VII and IV	8.00	12.56	0.940	0.0529
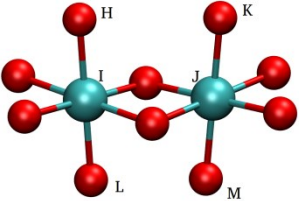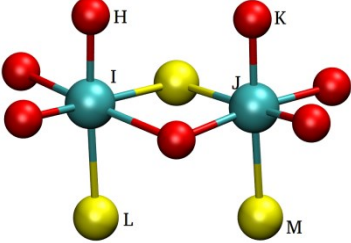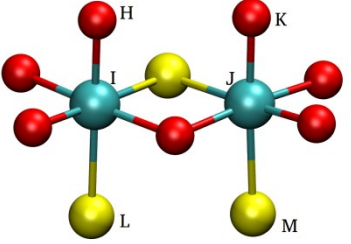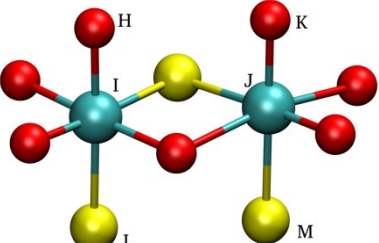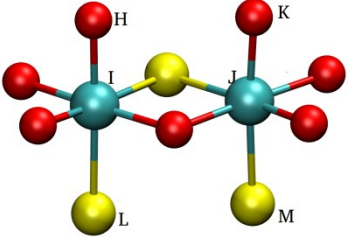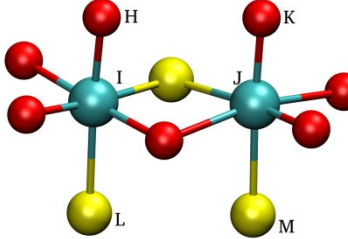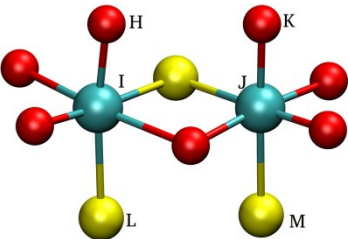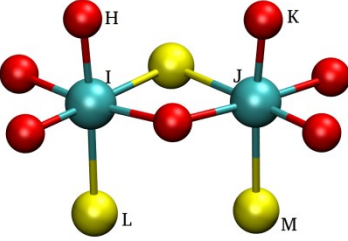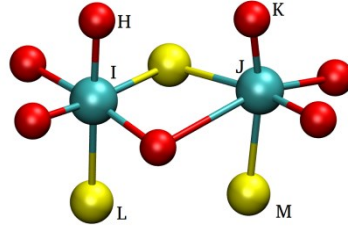
Table 4.14. Relative orientation between adjoining octahedra sharing an edge with one O atom and one S atom (O atoms belong to the crystal, not the ligands). Dihedral angles between Co-O axial bonds are reported along with the Osipov chirality index (G_0) and the Hausdorff chirality measure (HCM) for the pair of octahedra. G_0 values were neither weighted nor scaled, thus the values for the pair of octahedra are necessarily larger than those reported for single octahedra in Tables 4.2 to 4.12.

Octahedra	Dihedral HIJK (°)	Dihedral LIJM (°)	G_0	HCM
Reference structure	0.00	0.00	0.000	0.0000
Octahedra XI and VIII	1.61	3.30	-0.111	0.0518
Octahedra VIII and V	-3.38	-0.73	0.029	0.0233
Octahedra V and XI	-0.57	-1.26	0.599	0.0501

Octahedra II and X	1.47	1.95	-0.181	0.0296
Octahedra X and IX	-4.16	-2.39	0.384	0.0619
Octahedra IX and II	1.62	2.98	-0.003	0.0552
Octahedra III and VII	1.94	2.12	0.135	0.0149
Octahedra VII and XII	6.49	-5.18	1.053	0.0642
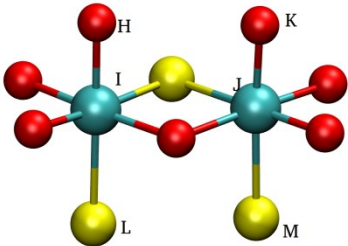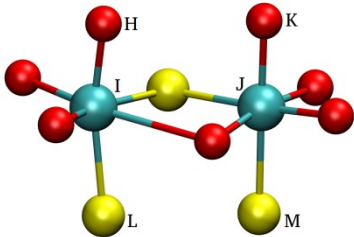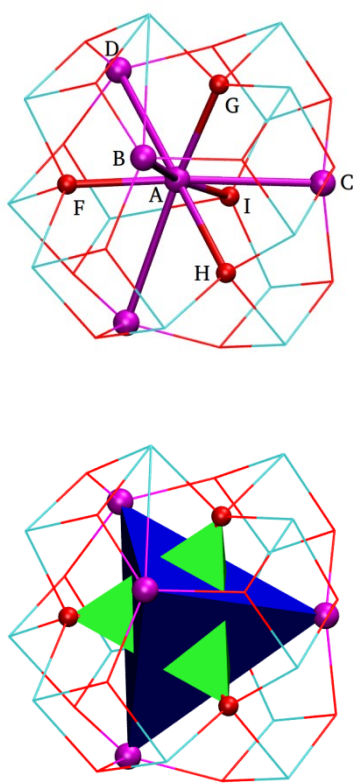
Octahedra VI and IV	4.14	1.69	0.121	0.0203
Octahedra XII and III	-3.31	3.93	0.002	0.0601

Table 4.15. Structure around the central Co(II) atom (*D*-Cys molecules have been omitted for clarity). The atoms directly bonded to the central Co(II) atom are depicted as magenta spheres for Co(II) atoms and red spheres for O atoms (the remaining atoms of the NP core are depicted as lines to provide a reference framework to localize the tetrahedra). The image on the top presents the labels used to analyze the atoms and bonds, whereas the image on the bottom provides graphical representation of the smaller O tetrahedron (in green) and the larger Co(II) tetrahedron (in blue) around the central Co(II) atom.

NP core	Bond length (nm)	Bond order	Spin population
	$r_{A-I} = 0.298$	$BO_{A-I}=0.41$	$I = 2.66$
	$r_{B-I} = 0.280$	$BO_{B-I}=0.25$	$A = 2.71$
	$r_{C-I} = 0.298$	$BO_{C-I}=0.45$	$B = 2.72$
	$r_{D-I} = 0.307$	$BO_{D-I}=0.52$	$C = 2.70$
	$r_{E-I} = 0.208$	$BO_{E-I}=0.15$	$D = 0.98$
	$r_{F-I} = 0.230$	$BO_{F-I}=0.16$	$E = 0.11$
	$r_{G-I} = 0.206$	$BO_{G-I}=0.21$	$F = 0.03$
	$r_{H-I} = 0.208$	$BO_{H-I}=0.15$	$G = 0.17$
			$H = 0.02$

CHAPTER V

Conclusion and Future Directions

5.1 Conclusion

The field of chiral inorganic nanostructures has a relatively short history; however, the field is currently experiencing explosive growth due to its effective optical properties, physical and chemical robustness. Inorganic material is very attractive for use in synthesizing chiral nanostructures because of its strong optical activity in the visible range. Most naturally occurring molecules exhibit CD signals primarily in the UV range, but these signals can be transferred to the visible range by incorporating inorganic materials. NPs provide new opportunities for the design of chiral materials and studies at the nexus of electromagnetism and chirality. The compatible scale of NPs with wavelengths generates strong interactions with light; and their strong transition magnetic dipole moments contribute to an effective optical activity.

In chapters II and III, I have proposed that circularly polarized light can be "imprinted" on nanoscale structures, by altering the chirality of the NPs participating in the self-assembly process. Because light-sensitivity is common for inorganic NPs, this study offers new methods for synthesizing chiral nanostructures using light as the primary parameter determining the

degree of asymmetry in the enantiomeric mixture of products. Furthermore, geological records suggest that inorganic NPs were a part of primordial Earth's conditions,[62] and therefore, selective photonic activation of seemingly achiral NPs might represent the missing link between cosmic CPL and inorganic/organic materials with preferential chirality.

In chapter IV, I switched gears slightly to the magnetic aspect of optical activity. Since the intensity of CD signals depend on both electro- and magnetic transition dipole moments, I used the transition metal cobalt as a material to increase the contribution of the magnetic component. Due to its strong magnetic transition dipole moment, I could observe at least 10 times higher optical activity from the cobalt oxide NPs than conventional plasmonic or semiconducting NPs. It is important to note that this comparison is between the value in the visible range from our NPs and that of Ag NPs in the UV region.[15] To my knowledge, it is *the first approach* of using a transition metal oxide to achieve strong optical activity in the visible range.

In summary, this dissertation is devoted to developing new design strategies for creating chiral inorganic nanostructures and understanding their interactions with electromagnetic and magnetic fields. The study ranges from angstrom to micro scale chirality using various inorganic materials including plasmonic, semiconductor, and magnetic materials. First, I showed the ability of NPs to retain the polarization information of incident photons, which should open pathways for the synthesis of chiral photonic materials and enhance our understanding of the origins of the homochirality of nature. Then, I suggested a new strategy to amplify the intrinsic optical activity of NPs by incorporating magnetic materials into the chiral system.

5.2 Future Directions

Even though chirality is hard-wired into every living biological system, it is not understood well enough to be exploited in biotechnology. For example, individual cells possess intrinsic chirality, which helps explain how tissues and organs are organized with a certain handedness.[153] However, conventional studies have been limited to designing cell culture scaffolds using peptide gels, and examining cell behaviors on 2D platforms. Incorporating chiral inorganic NPs into biomaterials will provide an opportunity to better understand asymmetric biological interactions. This effort should lead to a better understanding of chiral interactions between immune cells, antibodies, enzymes, and proteins.

In that manner, it is expected that these chiral inorganic NPs also can be used in the field of pharmaceuticals, optics, catalysis, and sensors. Considering that chiral, enantiomerically pure molecular drugs made up two-third of all drug sales worldwide in 2008,[154] chiral selective synthesis and separation of enantiomers are critical processes for disease diagnosis and therapy in the pharmaceutical industry. Because nanoscale chiral materials strongly rotate linear and circularly polarized light passing through them, and possess resistance to chemical- and photo-degradation, they are good candidates for biocatalysis, biosensors, and biolabels. Such optical effects are relatively easy to observe with inorganic materials. Thus, chiral inorganic nanostructures should be actively investigated as a part of the study of chiral biomaterials, photonics and plasmonics.

BIBLIOGRAPHY

1. Yeom, J. *et al.* Chiral templating of self-assembling nanostructures by circularly polarized light. *Nat. Mater.* **14,** 66–72 (2015).

2. Valev, V. K. *et al.* Nonlinear superchiral meta-surfaces: tuning chirality and disentangling non-reciprocity at the nanoscale. *Adv. Mater.* **26,** 4074–81 (2014).

3. Naaman, R. & Waldeck, D. H. Spintronics and Chirality: Spin Selectivity in Electron Transport Through Chiral Molecules. *Annu. Rev. Phys. Chem.* **66,** 263–281 (2015).

4. Pfleiderer, C., Rosch, a, Neubauer, a & Georgii, R. Skyrmion Lattice in a Chiral Magnet. *Science* 915–920 (2009).

5. Rikken, G. L. J. A. & Raupach, E. Enantioselective magnetochiral photochemistry. *Nature* **405,** 932–935 (2000).

6. Faraday, M. Experimental Researches in Electricity. Nineteens Series. Action of Magnets on Light. *Phil. Trans. R. Soc. Lond. 1846 136, 1-20,* **136,** 1–20 (1846).

7. Bordacs, S. Chirality of matter shows up via spin excitations. *Nat. Phys.* **8,** 734–738 (2012).

8. Barron, L. D. Magnetic molecules: Chirality and magnetism shake hands. *Nat. Mater.* **7,** 691–692 (2008).

9. Sessoli, R. *et al.* Strong magneto-chiral dichroism in a paramagnetic molecular helix observed by hard X-rays. *Nat. Phys.* **11,** 69–74 (2015).

10. Train, C. *et al.* Strong magneto-chiral dichroism in enantiopure chiral ferromagnets. *Nat. Mater.* **7,** 729–734 (2008).

11. Rikken, G. L. J. A. & Raupach, E. Observation of magneto-chiral dichroism. *Nature* **390,** 493–494 (1997).

12. Pop, F., Auban-Senzier, P., Canadell, E., Rikken, G. L. J. a & Avarvari, N. Electrical magnetochiral anisotropy in a bulk chiral molecular conductor. *Nat. Commun.* **5,** 3757 (2014).

13. Train, C., Gruselle, M. & Verdaguer, M. The fruitful introduction of chirality and control of absolute configurations in molecular magnets. *Chem. Soc. Rev.* **40,** 3297–3312 (2011).

14. Kitagawa, Y., Segawa, H. & Ishii, K. Magneto-chiral dichroism of organic compounds. *Angew. Chem. Int. Ed. Engl.* **50,** 9133–9136 (2011).

15. Nishida, N., Yao, H., Ueda, T., Sasaki, A. & Kimura, K. Synthesis and Chiroptical Study of D / L -Penicillamine-Capped Silver Nanoclusters. *Chem. Mater.* **19,** 2831–2841 (2007).

16. Moloney, M. P., Govan, J., Loudon, A., Mukhina, M. & Gun'ko, Y. K. Preparation of chiral quantum dots. *Nat. Protoc.* **10,** 558–573 (2015).

17. Ben-Moshe, A. *et al.* Enantioselective control of lattice and shape chirality in inorganic nanostructures using chiral biomolecules. *Nat. Commun.* **5,** 4302 (2014).

18. Zhou, Y. *et al.* Optical Coupling Between Chiral Biomolecules and Semiconductor Nanoparticles : Size-Dependent Circular Dichroism Absorption. *Angew. Chem. Int. Ed. Engl.* 11456–11459 (2011).

19. Mason, S. The origin of chirality in nature. *Trends Pharmacol. Sci* 20–23 (1986).

20. Lucas, P. W. *et al.* UV circular polarisation in star formation regions: The origin of homochirality? *Orig. Life Evol. Biosph.* **35,** 29–60 (2005).

21. Cronin, J. R. & Pizzarello, S. Enantiomeric Excesses in Meteoritic Amino Acids. *Science* **275,** 951 LP-955 (1997).

22. Govorov, A. O., Fan, Z., Hernandez, P., Slocik, J. M. & Naik, R. R. Theory of circular dichroism of nanomaterials comprising chiral molecules and nanocrystals: plasmon enhancement, dipole interactions, and dielectric effects. *Nano Lett.* **10,** 1374–82 (2010).

23. Fasman, G. D. *Circular Dichroism and the Conformational Analysis of Biomolecules.* (Springer US, 1996).

24. Nakanishi, K. & N. Berova, R. W. W. *Circular Dichroism: Principles and Applications.* (Wiley-VCH, 2000).

25. Bruhn, T. *et al.* Axially Chiral BODIPY DYEmers: An Apparent Exception to the Exciton Chirality Rule. *Angew. Chem. Int. Ed. Engl.* **53,** 14592–5 (2014).

26. Moffitt, W. & Moscowitz, A. Optical Activity in Absorbing Media. *J. Chem. Phys.* **30,** 648 (1959).

27. Alonso-Gómez, J. L., Rivera-Fuentes, P., Harada, N., Berova, N. & Diederich, F. An enantiomerically pure alleno-acetylenic macrocycle: Synthesis and rationalization of its outstanding chiroptical response. *Angew. Chem. Int. Ed. Engl.* **48,** 5545–5548 (2009).

28. Kuwahara, S. *et al.* Conclusive determination of the absolute configuration of chiral C60-fullerene cis-3 bisadducts by X-ray crystallography and circular dichroism. *Angew. Chem. Int. Ed. Engl.* **44,** 2262–5 (2005).

29. Schaaff, T. G. & Whetten, R. L. Giant Gold - Glutathione Cluster Compounds : Intense Optical Activity in Metal-Based Transitions. 2630–2641 (2000).

30. Petty, J. T., Zheng, J., Hud, N. V & Dickson, R. M. DNA-Templated Ag Nanocluster Formation. *J. Am. Chem. Soc.* **126,** 5207–5212 (2004).

31. Shemer, G. *et al.* Chirality of silver nanoparticles synthesized on DNA. *J. Am. Chem. Soc.* **128,** 11006–11007 (2006).

32. Gautier, C. & Bürgi, T. Chiral gold nanoparticles. *Chemphyschem* **10,** 483–92 (2009).

33. Nishida, N., Yao, H. & Kimura, K. Chiral Functionalization of Optically Inactive Monolayer-Protected Silver Nanoclusters by Chiral Ligand-Exchange Reactions. *Langmuir* **24,** 2759–2766 (2008).

34. Gautier, C. & Bürgi, T. Chiral Inversion of Gold Nanoparticles. *J. Am. Chem. Soc.* **130,** 7077–7084 (2008).

35. Nakashima, T., Kobayashi, Y. & Kawai, T. Optical activity and chiral memory of thiol-capped CdTe nanocrystals. *J. Am. Chem. Soc.* **131,** 10342–3 (2009).

36. Ren, M., Plum, E., Xu, J. & Zheludev, N. I. Giant nonlinear optical activity in a plasmonic metamaterial. *Nat. Commun.* **3,** 833 (2012).

37. Kuzyk, A. *et al.* DNA-based self-assembly of chiral plasmonic nanostructures with tailored optical response. *Nature* **483,** 311–4 (2012).

38. Guerrero-Martínez, A. *et al.* Intense optical activity from three-dimensional chiral ordering of plasmonic nanoantennas. *Angew. Chem. Int. Ed. Engl.* **50,** 5499–503 (2011).

39. Liu, S. *et al.* Synthesis of chiral TiO2 nanofibre with electron transition-based optical activity. *Nat. Commun.* **3,** 1215 (2012).

40. Chen, W. *et al.* Nanoparticle superstructures made by polymerase chain reaction: Collective interactions of nanoparticles and a new principle for chiral materials. *Nano Lett.* **9,** 2153–2159 (2009).

41. Mark, A. G., Gibbs, J. G., Lee, T.C. & Fischer, P. Hybrid nanocolloids with programmed three-dimensional shape and material composition. *Nat. Mater.* **12,** 802–7 (2013).

42. Ma, W. *et al.* Attomolar DNA detection with chiral nanorod assemblies. *Nat. Commun.* **4,** 2689; 1-8 (2013).

43. Gansel, J. K. *et al.* Gold helix photonic metamaterial as broadband circular polarizer. *Science* **325,** 1513–5 (2009).

44. Toyoda, K., Miyamoto, K., Aoki, N., Morita, R. & Omatsu, T. Using optical vortex to control the chirality of twisted metal nanostructures. *Nano Lett.* **12,** 3645–9 (2012).

45. Brachmann, J. F. S., Bakr, W. S., Gillen, J., Peng, a & Greiner, M. Inducing vortices in a Bose-Einstein condensate using holographically produced light beams. *Opt. Express* **19,** 12984–91 (2011).

46. Tabosa, J. W. R. Optical Pumping of Orbital Angular Momentum of Light in Cold Cesium Atoms. 4967–4970 (1999).

47. Padgett, M. & Bowman, R. Tweezers with a twist. *Nat. Photonics* **5,** 343–348 (2011).

48. Tang, Y. & Cohen, A. E. Enhanced enantioselectivity in excitation of chiral molecules by superchiral light. *Science* **332,** 333–6 (2011).

49. Feringa, B. L. & Van Delden, R. A. Absolute asymmetric synthesis: The origin, control, and amplification of chirality. *Angew. Chem. Int. Ed. Engl.* **38,** 3418–3438 (1999).

50. Green, M. M. & Selinger, J. V. Cosmic Chirality. *Science* **282,** 879 LP-879 (1998).

51. Bailey, J. Circular Polarization in Star- Formation Regions: Implications for Biomolecular Homochirality. *Science* **281,** 672–674 (1998).

52. Prins, L. J., Timmerman, P. & Reinhoudt, D. N. Amplification of Chirality: The 'Sergeants and Soldiers' Principle Applied to Dynamic Hydrogen-Bonded Assemblies. *J. Am. Chem. Soc.* **123,** 10153–10163 (2001).

53. Gautier, C. & Bürgi, T. Chiral N-isobutyryl-cysteine protected gold nanoparticles: Preparation, size selection, and optical activity in the UV-vis and infrared. *J. Am. Chem. Soc.* **128,** 11079–11087 (2006).

54. Chen, C.-C. *et al.* Three-dimensional imaging of dislocations in a nanoparticle at atomic resolution. *Nature* **496,** 74–7 (2013).

55. Ben Moshe, A., Szwarcman, D. & Markovich, G. Size dependence of chiroptical activity in colloidal quantum dots. *ACS Nano* **5,** 9034–9043 (2011).

56. Talapin, D. V *et al.* Quasicrystalline order in self-assembled binary nanoparticle superlattices. *Nature* **461,** 964–7 (2009).

57. Srivastava, S. *et al.* Light-controlled self-assembly of semiconductor nanoparticles into twisted ribbons. *Science* **327,** 1355–9 (2010).

58. Bustamante, C., Maestre, M. F. & Tinoco, I. Circular intensity differential scattering of light by helical structures. I. Theory. *J. Chem. Phys.* **73,** 4273 (1980).

59. Tang, Z., Kotov, N. a & Giersig, M. Spontaneous organization of single CdTe nanoparticles into luminescent nanowires. *Science* **297,** 237–40 (2002).

60. Gaponik, N. *et al.* Thiol-capping of CDTe nanocrystals: An alternative to organometallic synthetic routes. *J. Phys. Chem. B* **106,** 7177–7185 (2002).

61. Dolamic, I., Knoppe, S., Dass, A. & Bürgi, T. First enantioseparation and circular dichroism spectra of Au38 clusters protected by achiral ligands. *Nat. Commun.* **3,** 798 (2012).

62. Environmental, T. & Nanoparticles, N. Article The Environmental Significance of Natural Nanoparticles *Nature Education Knowledge* **4,** 7 (2013)

63. Wang, Y. *et al.* Dendrimer modified magnetic nanoparticles for immobilized BSA: a novel chiral magnetic nano-selector for direct separation of racemates. *J. Mater. Chem. B* **1,** 5028 (2013).

64. Ntosh, J. R. I. M. C. I. Computer Visualization of Three-Dimensional Image Data Using IMOD. **76,** 71–76 (1996).

65. Pettersen, E. F. *et al.* UCSF chimera - A visualization system for exploratory research and analysis. *J. Comput. Chem.* **25,** 1605–1612 (2004).

66. Bustamante, C., Tinoco, I. & Maestre, M. F. Circular Differential Scattering Can Be an Important Part of the Circular-Dichroism of Macromolecules. *Proc. Natl. Acad. Sci.* **80,** 3568–3572 (1983).

67. Ma, W. *et al.* Chiral plasmonics of self-assembled nanorod dimers. *Sci. Rep.* **3,** (2013).

68. Tomlin, E. K. and S. G. The optical constants of thin evaporated films of cadmium and zinc sulphides . *J. Phys. D Appl. Phys.* **8,** 581–594 (1975).

69. Govorov, A. O., Fan, Z. Y., Hernandez, P., Slocik, J. M. & Naik, R. R. Theory of Circular Dichroism of Nanomaterials Comprising Chiral Molecules and Nanocrystals: Plasmon Enhancement, Dipole Interactions, and Dielectric Effects. *Nano Lett.* **10,** 1374–1382 (2010).

70. George, J. & Thomas, K. G. Surface plasmon coupled circular dichroism of Au nanoparticles on peptide nanotubes. *J. Am. Chem. Soc.* **132,** 2502–3 (2010).

71. Mastroianni, A. J., Claridge, S. A. & Paul Alivisatos, A. Pyramidal and chiral groupings of gold nanocrystals assembled using DNA scaffolds. *J. Am. Chem. Soc.* **131,** 8455–8459 (2009).

72. Walters, R. S. *et al.* Configurationally Stable Longitudinally Twisted Polycyclic Aromatic Compounds. *J. Am. Chem. Soc.* **130,** 16435–16441 (2008).

73. Pearlstein, R. M., Davis, R. C. & Ditson, S. L. Giant Circular-Dichroism of High Molecular-Weight Chlorophyllide-Apomyoglobin Complexes. *Proc. Natl. Acad. Sci.* **79,** 400–402 (1982).

74. Chandra, S., Sundari, S. T., Raghavan, G. & Tyagi, A. K. Optical properties of CdTe nanoparticle thin films studied by spectroscopic ellipsometry. *J. Phys. D-Applied Phys.* **36,** 2121–2129 (2003).

75. Vincent, B. The van der Waals attraction between colloid particles having adsorbed layers. II. Calculation of interaction curves. *J. Colloid Interface Sci.* **42,** 270–285 (1973).

76. Ebaadi, S. H. Van der Waals interaction between surfactant-coated and bare colloidal particles. *Colloids and Surfaces* **2,** 155–168 (1981).

77. Morrison, I. D. *Colloidal dispersions : suspensions, emulsions, and foams*. (Wiley-Interscience, 2002).

78. Sinyagin, A. Y., Belov, A., Tang, Z. N. & Kotov, N. A. Monte Carlo computer simulation of chain formation from nanoparticles. *J. Phys. Chem. B* **110,** 7500–7507 (2006).

79. Israelachvili, J. N. *Intermolecular and surface forces*. (Academic Press, 2011).

80. Stubenrauch, C., Rojas, O. J., Schlarmann, J. & Claesson, P. M. Interactions between nonpolar surfaces coated with the nonionic surfactant hexaoxyethylene dodecyl Ether C12E6 and the origin of surface charges at the air/water interface. *Langmuir* **20,** 4977–4988 (2004).

81. Ederth, T. Computation of Lifshitz-van der Waals forces between alkylthiol monolayers on gold films. *Langmuir* **17,** 3329–3340 (2001).

82. Bergstrom, L. Hamaker constants of inorganic materials. *Adv. Colloid Interface Sci.* **70,** 125–169 (1997).

83. Mizuno, T., Namiki, A. & Tsuzuki, S. A Novel Filter Rating Method Using Less Than 30-nm Gold Nanoparticle and Protective Ligand. *Ieee Trans. Semicond. Manuf.* **22,** 452–461 (2009).

84. Kim, T., Lee, K., Gong, M. S. & Joo, S. W. Control of gold nanoparticle aggregates by manipulation of interparticle interaction. *Langmuir* **21,** 9524–9528 (2005).

85. Zhang, H. & Wang, D. Y. Controlling the growth of charged-nanoparticle chains through interparticle electrostatic repulsion. *Angew. Chem. Int. Ed. Engl.* **47,** 3984–3987 (2008).

86. Zhang, H. *et al.* Influence of interparticle electrostatic repulsion in the initial stage of aqueous semiconductor nanocrystal growth. *J. Phys. Chem. C* **112,** 1885–1889 (2008).

87. Gregory, J. Interaction of Unequal Double-Layers at Constant Charge. *J. Colloid Interface Sci.* **51,** 44–51 (1975).

88. Chang, H. C., Yossifon, G. & Demekhin, E. A. Nanoscale Electrokinetics and Microvortices: How Microhydrodynamics Affects Nanofluidic Ion Flux. *Annu. Rev. Fluid Mech. Vol 44* **44,** 401–426 (2012).

89. Kim, D., Posner, J. D. & Santiago, J. G. High flow rate per power electroosmotic pumping using low ion density solvents. *Sensors Actuators A Phys.* **141,** 201–212 (2008).

90. Wang, C. M., Wang, L., Zhu, X. R., Wang, Y. G. & Xue, J. M. Low-voltage electroosmotic pumps fabricated from track-etched polymer membranes. *Lab Chip* **12,** 1710–1716 (2012).

91. Shanbhag, S. & Kotov, N. A. On the origin of a permanent dipole moment in nanocrystals with a cubic crystal lattice: Effects of truncation, stabilizers, and medium for CdS tetrahedral homologues. *J. Phys. Chem. B* **110,** 12211–12217 (2006).

92. Zhang, Z. L., Tang, Z. Y., Kotov, N. A. & Glotzer, S. C. Simulations and analysis of self-assembly of CdTe nanoparticles into wires and sheets. *Nano Lett.* **7,** 1670–1675 (2007).

93. Jin, R. *et al.* Photoinduced conversion of silver nanospheres to nanoprisms. *Science* **294,** 1901–1904 (2001).

94. Murdoch, M. *et al.* The effect of gold loading and particle size on photocatalytic hydrogen production from ethanol over Au/TiO2 nanoparticles. *Nat. Chem.* **3,** 489–492 (2011).

95. Yeom, J. *et al.* Chiral templating of self-assembling nanostructures by circularly polarized light. *Nat. Mater.* 1–7 (2014).

96. Lee, G. P. *et al.* Light-Driven Transformation Processes of Anisotropic Silver Nanoparticles. 5911–5921 (2013).

97. Jin, R. *et al.* Photoinduced conversion of silver nanospheres to nanoprisms. *Science* **294,** 1901–3 (2001).

98. Kurihara, K., Kizling, J., Stenius, P. & Fendler, J. H. Laser and pulse radiolytically induced colloidal gold formation in water and in water-in-oil microemulsions. *J. Am. Chem. Soc.* **105,** 2574–2579 (1983).

99. Unal, A. A., Stalmashonak, A., Seifert, G. & Graener, H. Ultrafast dynamics of silver nanoparticle shape transformation studied by femtosecond pulse-pair irradiation. *Phys. Rev. B - Condens. Matter Mater. Phys.* **79,** 1–7 (2009).

100. Podlipensky, A. V., Grebenev, V., Seifert, G. & Graener, H. Ionization and photomodification of Ag nanoparticles in soda-lime glass by 150 fs laser irradiation: A luminescence study. *J. Lumin.* **109,** 135–142 (2004).

101. Seifert, G., Stalmashonak, a, Hofmeister, H., Haug, J. & Dubiel, M. Laser-Induced, Polarization Dependent Shape Transformation of Au/Ag Nanoparticles in Glass. *Nanoscale Res. Lett.* **4,** 1380–1383 (2009).

102. Johnson, P. B. & Christy, R. W. Optical Constants of the Noble Metals. *Phys. Rev. B* **6,** 4370–4379 (1972).

103. Hochepied, J. ., Sainctavit, P. & Pileni, M. . X-ray absorption spectra and X-ray magnetic circular dichroism studies at Fe and Co L2,3 edges of mixed cobalt–zinc ferrite nanoparticles: cationic repartition, magnetic structure and hysteresis cycles. *J. Magn. Magn. Mater.* **231,** 315–322 (2001).

104. McPeak, K. M. *et al.* Complex chiral colloids and surfaces via high-index off-cut silicon. *Nano Lett.* **14,** 2934–2940 (2014).

105. Jain, P. K., Xiao, Y., Walsworth, R. & Cohen, A. E. Surface plasmon resonance enhanced magneto-optics (SuPREMO): Faraday rotation enhancement in gold-coated iron oxide nanocrystals. *Nano Lett.* **9,** 1644–1650 (2009).

106. Yannopapas, V. & Vanakaras, A. G. Strong Magnetochiral Dichroism in Suspensions of Magnetoplasmonic Nanohelices. *ACS Photonics* **2,** 1030–1038 (2015).

107. Crassous, J. Chiral transfer in coordination complexes: towards molecular materials. *Chem. Soc. Rev.* **38,** 830 (2009).

108. Mukhina, M. V *et al.* Intrinsic Chirality of CdSe/ZnS Quantum Dots and Quantum Rods. *Nano Lett.* **15,** 2844–51 (2015).

109. Román-Velázquez, C. E., Noguez, C. & Garzón, I. L. Circular dichroismsimulated dpectra of chiralgold nanoclusters: A dipole approximation. *J. Phys. Chem. B* **107,** 12035–12038 (2003).

110. Sun, S. *et al.* Monodisperse MFe_2O_4 (M = Fe, Co, Mn) Nanoparticles. *J. Am. Chem. Soc.* **126,** 273–279 (2004).

111. Lee, J.-H. *et al.* Exchange-coupled magnetic nanoparticles for efficient heat induction. *Nat. Nanotechnol.* **6,** 418–422 (2011).

112. Lee, N. & Hyeon, T. Designed synthesis of uniformly sized iron oxide nanoparticles for efficient magnetic resonance imaging contrast agents. *Chem. Soc. Rev.* **41,** 2575–2589 (2012).

113. Kumar, J. *et al.* Circularly polarized luminescence in chiral silver nanoclusters. *Chem. Commun.* **21,** 13488–13500 (2017).

114. Goto, T. *et al.* Induction of Strong and Tunable Circularly Polarized Luminescence of Nonchiral, Nonmetal, Low-Molecular-Weight Fluorophores using Chiral Nanotemplates. *Angew. Chem. Int. Ed.* **56,** 2989–2993 (2017).

115. Barron, L. D. & Vrbancich, J. Magneto-chiral birefringence and dichroism. *Mol. Phys.* **51,** 715–730 (1984).

116. Kuzyk, A. *et al.* DNA-based self-assembly of chiral plasmonic nanostructures with tailored optical response. *Nature* **483,** 311–4 (2012).

117. Wang, G. *et al.* Hydrothermal Synthesis and Optical, Magnetic, and Supercapacitance Properties of Nanoporous Cobalt Oxide Nanorods. *J. Phys. Chem. C* **113,** 4357–4361 (2009).

118. Fujioka, Y., Frantti, J., Puretzky, A. & King, G. Raman Study of the Structural Distortion in the Ni1–xCoxTiO3 Solid Solution. *Inorg. Chem.* **55,** 9436–9444 (2016).

119. Ikedo, Y. *et al.* Spatial inhomogeneity of magnetic moments in the cobalt oxide spinel Co3 O4. *Phys. Rev. B - Condens. Matter Mater. Phys.* **75,** 1–8 (2007).

120. Reid, M. F. Electronic Structure and Transition Intensities in Rare-Earth Materials. (2014).

121. Dodson, C. M. & Zia, R. Magnetic dipole and electric quadrupole transitions in the trivalent lanthanide series: Calculated emission rates and oscillator strengths. *Phys. Rev. B - Condens. Matter Mater. Phys.* **86,** 1–10 (2012).

122. Shiratsu, T. & Yao, H. Magnetic circular dichroism of thiolate-protected plasmonic gold nanoparticles: separating the effects of interband transitions and surface magnetoplasmon resonance. *J. Nanophotonics* **10,** 46004 (2016).

123. Yao, H. & Ishikawa, Y. Finite Size Effect on Magneto-Optical Responses of Chemically Modified Fe3O4 Nanoparticles Studied by MCD Spectroscopy. *J. Phys. Chem. C* **119,** 13224–13230 (2015).

124. Yao, H. & Shiratsu, T. Individual and collective modes of surface magnetoplasmon in thiolate-protected silver nanoparticles studied by MCD spectroscopy. *Nanoscale* **8,** 11264–11274 (2016).

125. Pineider, F. *et al.* Circular magnetoplasmonic modes in gold nanoparticles. *Nano Lett.* **13,** 4785–4789 (2013).

126. Kuzmin, D. A., Bychkov, I. V., Shavrov, V. G. & Temnov, V. V. Giant faraday rotation of high-order plasmonic modes in graphene-covered nanowires. *Nano Lett.* **16,** 4391–4395 (2016).

127. Yu, J. H. *et al.* Giant Zeeman splitting in nucleation-controlled doped CdSe:Mn2+ quantum nanoribbons. *Nat Mater* **9,** 47–53 (2010).

128. Norberg, N. S. & Gamelin, D. R. Giant Zeeman effects in colloidal diluted magnetic semiconductor quantum dots with homogeneous dopant speciation. *J. Appl. Phys.* **99,** 08M104 (2006).

129. Baranova, N. B. & Zel'Dovich, B. Y. Theory of a new linear magnetorefractive effect in liquids. *Mol. Phys.* **38,** 1085–1098 (1979).

130. Li, J. *et al.* The increase of the light transparency induced by a magnetic field for the colloid film based on α-FeOOH nanoparticles. *Opt. Mater. Express* **2,** 1760 (2012).

131. Becke, A. D. Density-functional thermochemistry. III. The role of exact exchange. *J. Chem. Phys.* **98,** 5648 (1993).

132. Hehre, W. J., Ditchfield, R. & Pople, J. A. Self—Consistent Molecular Orbital Methods. XII. Further Extensions of Gaussian—Type Basis Sets for Use in Molecular Orbital Studies of Organic Molecules. *J. Chem. Phys.* **56,** 2257–2261 (1972).

133. Dill, J. D. & Pople, J. a. Self-consistent molecular orbital methods. XV. Extended Gaussian-type basis sets for lithium, beryllium, and boron. *J. Chem. Phys.* **62,** 2921 (1975).

134. Rassolov, V. A., Pople, J. A., Ratner, M. A. & Windus, T. L. 6-31G* basis set for atoms K through Zn. *J. Chem. Phys.* **109,** 1223–1229 (1998).

135. Valiev, M. *et al.* NWChem: A comprehensive and scalable open-source solution for large scale molecular simulations. *Comput. Phys. Commun.* **181,** 1477–1489 (2010).

136. Bernard Raveau, M. S. in *Cobalt Oxides from crystal chemistry to physics* 71–128 (Wiley-VCH Verlag GmbH & Co. KGaA, 2012).

137. Harman, B. L. A. & Sv, I. Metal Complexes of Sulphur-containing Ligands . V . Interactions of Cobalt (I1) Ion with L-cysteine and its Derivatives. *Inorganica Chim. Acta,* **80,** 75–83 (1983).

138. Bronstein, L. *et al.* Influence of iron oleate complex structure on iron oxide nanoparticle formation. *Chem. Mater.* **19,** 3624–3632 (2007).

139. Grzelczak, M., Pérez-Juste, J., Mulvaney, P. & Liz-Marzán, L. M. Shape control in gold nanoparticle synthesis. *Chem. Soc. Rev.* **37,** 1783–91 (2008).

140. Schubert, M. P. Cobalt Complexes of Cysteine. *J. Am. Chem. Soc.* **53,** 3851–3861 (1931).

141. Kothari. Cobalt(III) Complexes of Cysteine and Cysteine Derivatives. *Inorg. Chem.* **8,** 2276–2280 (1969).

142. Kingston, A. E. & Hibbert, A. The calculation of the line strengths for M1 transitions between the 2s2, 2s2p and 2p2 states in Be-like ions. *Phys. Scr.* **64,** 58 (2001).

143. Pachucki, K. & Komasa, J. Magnetic dipole transitions in the hydrogen molecule. *Phys. Rev. A - At. Mol. Opt. Phys.* **83,** 1–4 (2011).

144. Sturm, J. E. Grid of expressions related to the Einstein coefficients. *J. Chem. Educ.* **67,** 32 (1990).

145. Igor N. Serdyuk, Nathan R. Zaccai, J. Z. *Methods in Molecular Biophysics: Structure, Dynamics, Function*. (Cambridge University Press, 2007).

146. John M. Brown, A. C. *Rotational Spectroscopy of Diatomic Molecules*. (Cambridge University Press, 2003).

147. Schellman, J. A. Circular Dichoroism and Optical Rotation. *Chem. Rev.* **75,** 323–331 (1975).

148. Mao, X., Sun, H., Wang, W., Chen, X. & Lu, Y. Ferromagnetic, ferroelectric properties, and magneto-dielectric effect of Bi4.25La0.75Fe0.5Co0.5Ti 3O15 ceramics. *Appl. Phys. Lett.* **102,** 0–5 (2013).

149. Lawes, G. *et al.* Magnetodielectric effects at magnetic ordering transitions. *Prog. Solid State Chem.* **37,** 40–54 (2009).

150. J. Kishigami, N. Mori, E. S. Magnetic field dependence of dielectric constant of magnetite at low temperature. *J. Magn. Magn. Mater.* **34,** 785–786 (1983).

151. Carr, E. F. Influence of Electric and Magnetic Fields on the Dielectric Constant and Loss of the Liquid Crystal Anisaldazine. *J. Chem. Phys.* **38,** 1536–1542 (1963).

152. A.V.Turik, A.V.Pavlenko, L. A. R. Maxwell – Wagner Relaxation and Magnetodielectric Properties. *Phys. Solid State* **58,** 1549–1551 (2016).

153. Green, D. W., Lee, J.-M., Kim, E.-J., Lee, D.-J. & Jung, H.-S. Chiral Biomaterials: From Molecular Design to Regenerative Medicine. *Adv. Mater. Interfaces* **3,** 1500411 (2016).

154. Lin, G.-Q., Zhang, J.-G. & Cheng, J.-F. in *Chiral Drugs* 3–28 (John Wiley & Sons, Inc., 2011).